Control of nonlinear modulated waves in flexible mechanical metamaterials

Antoine Demiquel

THESE DE DOCTORAT

DE
LE MANS UNIVERSITE
SOUS LE SCEAU DE
LA COMUE ANGERS – LE MANS

ECOLE DOCTORALE N° 602
Sciences de l'Ingénierie et des Systèmes
Spécialité : Acoustique

Par
Antoine DEMIQUEL

Control of nonlinear modulated waves in flexible mechanical metamaterials

Thèse présentée et soutenue à Le Mans, le 19 Septembre 2024
Unité de recherche : Laboratoire d'Acoustique de l'Université du Mans, UMR CNRS 6613
Thèse N° : 2024LEMA1015

Rapporteurs avant soutenance :

Dimitrios FRANTZESKAKIS	Professor, National and Kapodistrian University of Athens, Greece
Victor SANCHEZ MORCILLO	Professor, Universidad Politécnica de Valencia, Spain

Composition du Jury :

Examinateurs :	Christophe JOSSERAND	Directeur de recherche CNRS, LadHyx Ecole Polytechnique, France
	Xinxin GUO	Post-doctoral fellow, Swiss Federal Institute of Technology ETH, Switzerland
	Rajesh CHAUNSALI	Assistant professor, Indian Institute of Science Bengaluru, India
Dir. de thèse :	Vincent TOURNAT	Directeur de recherche CNRS, LAUM UMR CNRS 6613, France
Co-dir. de thèse :	Georgios THEOCHARIS	Chargé de recherche CNRS, LAUM UMR CNRS 6613, France
	Vassos ACHILLEOS	Chargé de recherche CNRS, LAUM UMR CNRS 6613, France

Le Mans Université, Le Mans, France
École Doctorale Sciences de l'Ingénierie et des Systèmes

Doctoral Thesis

Speciality: Acoustics

Presented by
Antoine DEMIQUEL
submitted for the Doctoral degree

Control of nonlinear modulated waves in flexible mechanical metamaterials

---

Defense scheduled on September 19th 2024

Members of the committee:

D. Frantzeskakis	Professor, National and Kapodistrian University of Athens	-*Reviewer*
V. Sánchez	Professor, Universidad Politécnica de Valencia	-*Reviewer*
C. Josserand	Directeur de Recherche CNRS, LadHyx Ecole Polytechnique	-*Examiner*
X. Guo	Post-Doc fellow, Swiss Federal Institute of Technology ETH	-*Examiner*
R. Chaunsali	Assistant Professor, Indian Institute of Science Bengaluru	-*Examiner*
V. Tournat	Directeur de Recherche CNRS, LAUM UMR CNRS 6613	-*Supervisor*
G. Theocharis	Chargé de Recherche CNRS, LAUM UMR CNRS 6613	-*Co-supervisor*
V. Achilleos	Chargé de Recherche CNRS, LAUM UMR CNRS 6613	-*Co-supervisor*

Acknowledgements

Completing this doctoral thesis represents much more than a simple water drop in academic research. It is the fruit of several years of hard work, intense research, doubts, challenges, and enriching collaborations. In these few lines, I would like to express my gratitude to all those who have supported and accompanied me all along the way.

First of all, many thanks to my thesis supervisors Vincent Tournat, Georgios Theocharis, and Vassos Achilleos. Your expertise and sound advice were invaluable and indispensable to the success of my first steps in the research universe. You were able to find the right words to motivate me, reassure me in times of doubt, and encourage me to always *"trust in the process"* and push my limits back. I would particularly like to thank you Georgios for your availability, your involvement at all times, and for showing me around Athens (Σουβλάκια για πάντα). These were unforgettable moments!

I would like to acknowledge Dimitrios Frantzeskakis and Victor Sánchez-Morcillo for agreeing to be the reviewers of this thesis. Many thanks to Christophe Josserand, Xinxin Guo, and Rajesh Chaunsali for being members of my PhD committee and giving particularly relevant comments on my work. I do not forget to mention Stéphane Job and Jordan Raney for having taken part in my *"comité de suivi individuel"* and for the interesting discussions around the doctoral thesis in general and the post-thesis period, thank you.

I will never forget to mention my friends: Nicolas, Kevin, Lilian, Thomas, Mark, and Antoine, who stayed back in my native Catalan Pyrenees. You remain in my heart and thoughts, despite the distance. Our Discord sessions have been invaluable in helping me recharge. Although I've been somewhat absent this past year, your support means the world.

Of course, many thanks to all my friends from the LAUM who have made my daily work in the laboratory so much more enjoyable. "Merci les bb": Juliette, Martin, Charlotte, Anis, Lou-Anne, Constance, Jinyue, Mathieu, Orphée, and Melvin. A special mention to my original office mate Alexis, from the granular room to the dark-dusty office (which finally became luminous...). Thank you for the daily discussions and jokes and by the way, "tell us something your mum doesn't know".

A huge thank you to my family, especially my parents, for their unconditional love and support. You are always there when I need you. You have helped me realize my dream by encouraging self-discovery and respecting my career choices. I love you.

Finally, I do not have the words to express the depth of my gratitude for my lover, Lou-Anne. Your support, patience, kindness, and your daily intentions allowed me to finalize my work in due time. It is now your turn to live this adventure and I will be there every step of the way. I love you.

List of Figures

Contents

1 | Introduction

Contents

1.1. Background on metamaterials

Over the past two decades, architecturally structured mechanical structures, also known as metamaterials, have been central to the breakthrough observed in the field of wave physics. In this context of waves, metamaterials are synthetic composite structures that offer unprecedented control over possibly different types of waves (light, heat, sound, mechanical vibrations [9, 10], etc.). The concepts of unusual wave properties that are tailorable are not recent and examples of theoretical results such as in 1968 with an electrodynamic structure broadcasting a negative refractive index described by Vesalago et. al. [11] exist. However, the study of metastructures was democratized during the XXIst century thanks to important advances in the fabrication and computation aspects. The fact that these materials can manipulate waves in ways that traditional materials cannot, leads to innovations across various fields. For example in optics, metamaterials called photonic crystals are used to make devices such as superlenses [12, 13] or invisibility cloaks [14, 15].

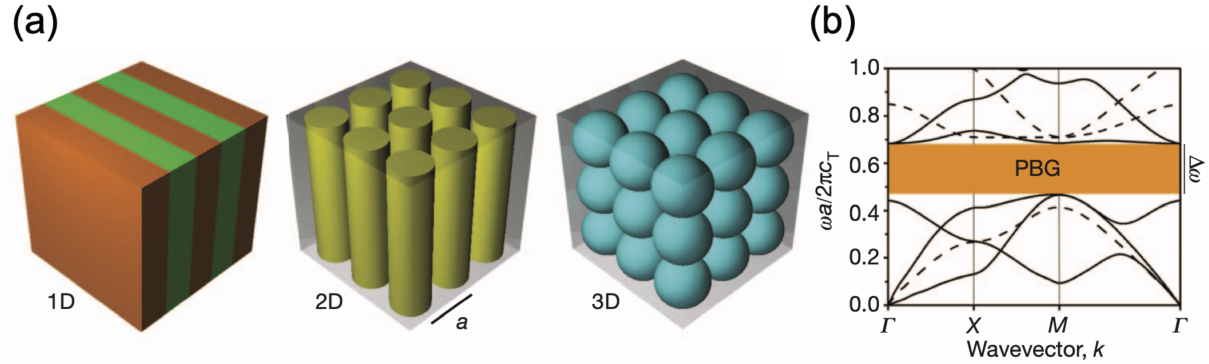

Figure 1.1: (a) Schematics of 1D, 2D, and 3D phononic crystals made of two different elastic materials arranged periodically. The different colors represent materials with different elastic properties. (b) An example of a phononic band diagram $\omega(k)$ for a two-dimensional phononic crystal [1].

In acoustics and vibrations, there exists a very large variety of metamaterials that generally aim to absorb broadband frequencies with different manufacturing and designing tricks. The most famous acoustic metamaterials are phononic crystals. They are characterized by periodically arranged structures made from scatterers and resonators with dimensions and spacings comparable to the wavelength [16, 17]. Such structures can be modeled as 1D, 2D, or 3D materials, as displayed in Fig. 1.1. In the one-dimensional case, a metamaterial can be a periodic layered structure of alternating materials with different properties [18], see Fig. 1.1 (a). Another example of one-dimensional metamaterial is a

waveguide periodically loaded with Helmholtz resonators [19, 9, 20]. In two dimensions, a phononic crystal can be obtained by embedding periodic arrays of cylindrical inclusions in a host medium, like air for instance [21], or a meta-surface made of elastic particles such as spheres ordered to form granular phononic crystal [9, 22, 23, 10]. In three dimensions, spherical inclusions enable negative elastic constants in certain frequency ranges [24]. Periodicity control generally induces the formation of band gaps in metamaterials, frequency ranges where wave propagation is impossible. All these properties make phononic crystals useful for applications in vibration insulation, noise reduction, and wave guiding.
Locally-resonant metamaterials also point to a large category of acoustic metamaterials [25, 26]. These metamaterials exploit local resonances to achieve high-quality-factor absorption, the most known example being Helmholtz resonators [27, 28]. They are particularly useful to target specific frequencies and are still extensively explored to improve existing efficient structures. The coupling between broadband metamaterials and resonating designs is nowadays a particularly active field of research, with the use of membranes and cavities for instance [29, 30].

In this PhD thesis, we focus on a particular class of phononic crystals called flexible mechanical metamaterials, which offer further avenues for the exploration of wave manipulation and structural reconfiguration thanks to their high deformability.

1.2. Overview of flexible mechanical metamaterials

Flexible mechanical metamaterials (FlexMM) or mechanism-based materials [31] are carefully engineered structures that consist of stiff and flexible elements, where the stiff elements connected by the soft ones can move relatively in a continuous way. These structures form usually a periodic network of unit cells. Their properties and behaviors are derived from the geometry of the structure rather than just its intrinsic properties (chemical composition, atomic structure...). Each cell can deform, rotate, buckle, fold, and snap in response to mechanical constraints and is designed so that adjacent cells of the network can interact, resulting in a desired collective behavior. The microstructural architecture impacts the global structure with unique and often advanced unconventional properties such as shape morphing [32, 33, 34, 35], topological protection [36, 37, 38], and nonlinear responses [39, 7].

In this overview, we present some of these structures, their properties, and applications. We particularly look at a structure based on the rotating element mechanism.

1.2.1. Auxetic metamaterials

An auxetic metamaterial is a structure with a negative Poisson's ratio ($\nu < 0$), even though the constituent material has a positive one. Unlike conventional materials that become laterally thinner when stretched ($\nu > 0$), auxetic materials expand laterally due to specific structural designs. For instance, re-entrant cells and rotating elements can rearrange themselves under mechanical stress to expand laterally when stretched, and to contract when compressed, as displayed in Fig. 1.2.

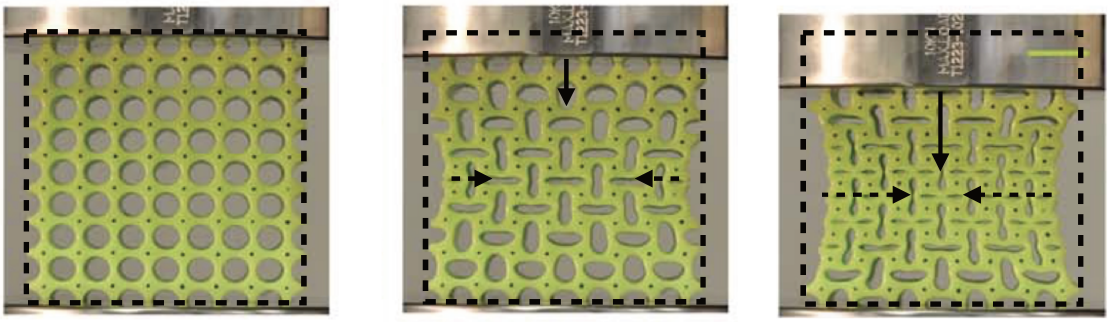

Figure 1.2: Uniaxial compression of a rubber block with an array of circular holes. The periodic pattern created by the holes conveys an auxetic property to the structure. The deformation undergoes a reversible pattern transformation [2].

Other structural designs include the re-entrant honeycomb, which features a hexagonal pattern with inwardly angled sides that widen when stretched, the bow-tie or arrowhead unit cell, the rotating element cell, and the double-V. Chiral structures also present a twisting geometry that causes lateral spreading when stretched. These examples show that appropriately designed architectures can push the properties of metamaterials beyond those of their constituents.

The creation of flexible mechanical metamaterials with auxetic properties is possible thanks to advanced manufacturing techniques such as 3D printing or laser cutting. These methods allow precise fabrication of complex structures such as origami and kirigami structures.

1.2.2. Origami and kirigami-inspired metamaterials

One innovative approach to making flexible mechanical metamaterial involves the Japanese arts of origami (folding) and kirigami (cutting) techniques, transforming flat sheets into complex three-dimensional shapes that offer remarkable flexibility and the ability to undergo large deformations.

Origami-inspired designs can fold and unfold into intricate shapes allowing for the creation of deployable structures. One pioneer application in space engineering is the Miura-ori structure, displayed in Fig. 1.3 (a) which is used for the creation of deployable solar panels based on 2D sheets with predefined crease patterns. The structure can be compactly stored and expanded to full size in space.

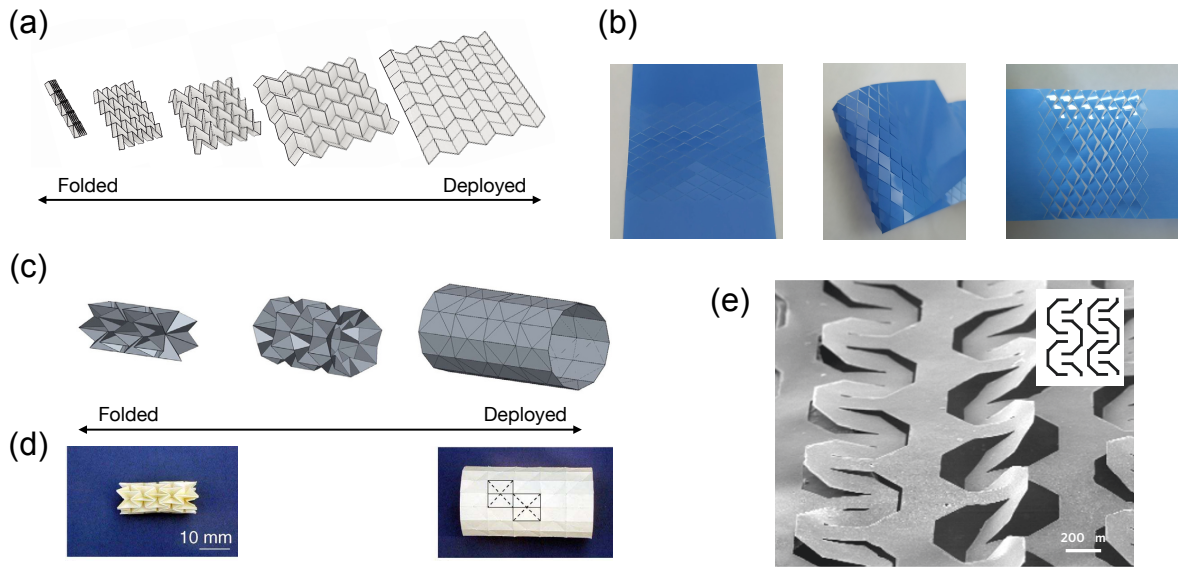

Figure 1.3: (a) Deploying motions of Miura-ori fold [3]. (b) Stretchable kirigami plate manufactured in LAUM. (c) Schematic showing the deployment of an origami stent [4] and (d) Photograph of a stent graft design made from a sheet [5]. (e) Microscale kirigami patterns in GO-PVA nanocomposites using photolithography [6].

Kirigami-based structures are produced by introducing arrays of cuts or engravings into thin sheets of material, see Fig. 1.3 (b), and currently participate in the field of wearable electronics. For instance, kirigami-type graphene sheets, displayed in Fig. 1.3 (e), are used to add elasticity in stiff nanocomposites without compromising their electrical conductance [6], and to make stretchable lithium-ion batteries [40].

In biomedical engineering, origami and kirigami-inspired stents [4, 5], see Fig. 1.3 (c-d), as well as surgical devices [41] can be minimally invasive during insertion and then expand to their functional form within the body. Additionally, these structures are utilized in designing energy-absorbing systems for impact protection [42, 43] such as vehicle crash box [44] or assistive shoe grips [45], as they efficiently dissipate energy. The combination of both kirigami and origami-inspired structures makes them suitable for adaptive architectures and soft robotics [46, 47] sometimes bio-inspired.

1.2.3. Rotating elements-based mechanism

Rotating elements-based structures form a class of flexible mechanical metamaterials composed of an assembly of rigid elements that can have different shapes (squares, crosses, rectangles, etc.) connected by thin, highly deformable ligaments. One example of a rotating element structure is displayed in Fig. 1.4 (a). It is made of Lego® pieces and plastic films to form a 1D chain of particles, see Fig. 1.4 (b), that can rotate and translate. Theoretically speaking, FlexMMs are most often modeled using a lumped element approach to simplify them into a lattice structure that can lead to the deduction of the equations of motion and analytical solutions. Though linear wave metamaterials constitute the

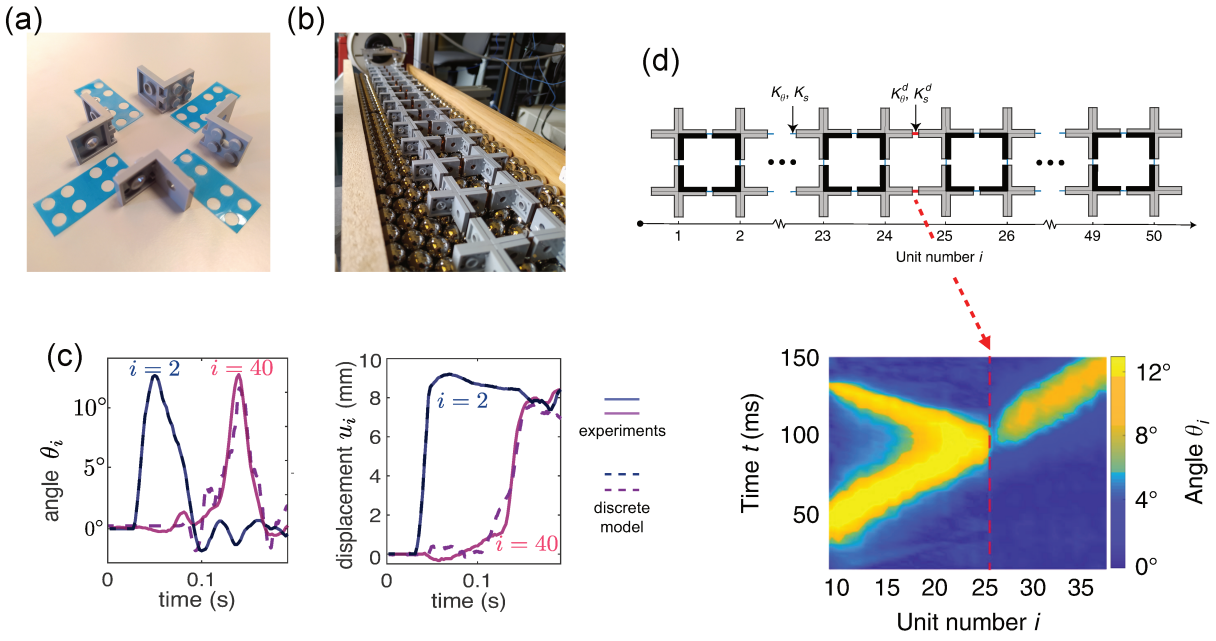

Figure 1.4: (a) Metamaterial element: cross built with legos, linked together by plastic films. (b) Experimental set-up: chain linked to a shaker laid on low friction support granular bed (LAUM). (c) Experimental data of a propagating elastic vector soliton along the chain initiated by a pulse, compared with the theoretical model. (d) Experimental rotational measurement during the propagation of a pulse for soliton splitters [7].

vast majority of studied designs, several nonlinear wave effects have been studied and revealed in flexible mechanical metamaterials [48], including pulse vector solitons [39, 7] (Fig. 1.4 (c)), soliton splitters (Fig. 1.4 (d)), and diodes [7] or bistable effect [49]. In the case of soliton splitters, a local change in the mechanical stiffness of the hinges of the chain (see Fig. 1.4 (d)) plays the role of interface. An incoming pulse elastic vector soliton is splitted into a transmitted and a reflected one. All these studies show that flexible mechanical metamaterials offer a rich platform for generating and controlling the

behavior of nonlinear wave propagation. In addition to pulse-like waves such as solitary waves, periodic waves [50, 48] or modulated waves have also been investigated recently in these systems.

1.3. History of solitary waves, called solitons

Solitary waves, commonly called solitons, have been the subject of numerous theoretical and experimental studies through many physical domains including hydrodynamics [51] [52], nonlinear optics [53], plasma physics [54], or mechanics [55].

The first documented observation of a solitary wave was made by the Scottish civil engineer and naval architect, John Scott Russell in 1834. The solitary wave was generated by

"a boat which was rapidly drawn along a narrow channel by a pair of horses, when the boat suddenly stopped-not so the mass of water in the channel which it had put in motion; it accumulated round the prow of the vessel in a state of violent agitation, then suddenly leaving it behind rolled forward with great velocity, assuming the form of a large solitary elevation, a rounded, smooth and well-defined heap of water, which continued its course along the channel apparently without change of form or diminution of speed".

John Scott Russell, Report on Waves 1844 [56]

Based on this observation, wave-tank experiments established several remarkable conclusions on the physical properties of solitary water waves, including a relation between the velocity of the wave, its amplitude, and the water depth. This work has faced skepticism due to the lack of mathematical proof and its contradiction with Airy's nonlinear shallow water wave theory, which suggested that waves of finite amplitude cannot maintain their shape while traveling. In 1895, the concept of solitary wave was rehabilitated thanks to the work of Diederik J. Korteweg and Gustav de Vries [57]. They developed the Korteweg-de Vries (KdV) equation, which accurately describes the phenomena observed by Russell, including the interaction effect between dispersion and nonlinearity of the system. Through this equation, they identified periodic wave solutions in the shallow water domain known as cnoïdal waves, which converge to solitary waves in the limit of large wavelengths, see Fig. 1.5. Research on solitary waves continues in the 1950s with the Fermi-Pasta-Ulam-Tsingou (FPUT) problem [58]. This problem consists of a numerical study of the energy equipartition in an anharmonic one-dimensional monoatomic chain of masses. Contrary to their expectations, the system did not exhibit the expected equipartition of energy, but instead, the energy was localized recurrently in a certain number of modes, showing

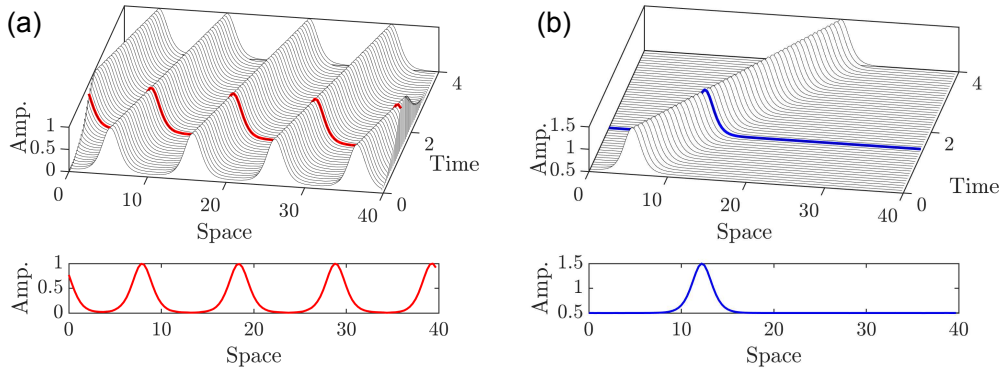

Figure 1.5: Representation of a cnoïdal wave (a), and a solitary wave (b) of the KdV equation.

the emergence of a soliton-like behavior. This paradox and what results from it widely spread interest in the nonlinear dynamics of lattice systems. From the FPUT problem, Norman Zabusky and Martin Kruskal's work in 1965 [59] marked a breakthrough, linking the theory of solitons previously developed for shallow water waves (continuous media), to the discrete lattice setting. Through their research, they discovered a new property for solitary waves, namely that two solitons collide elastically. Their shape and speed are not disturbed by their collision with other solitary waves. Due to this particle-like property and as a tribute, they decided to call this kind of solitary wave "soliton".

Examples of this collision are shown in Fig. 1.7 which represents the propagation of kink-solitons from the sine-Gordon equation which can be used as a simple model for elementary particles [60, 61]. Kink-soliton solutions of the sine-Gordon equation can be experimentally observed in the continuous limit of the mechanical lattice systems made up of pendulums elastically connected by springs [55]. The device displayed in Fig. 1.6 was the resulting demonstrator of a research project at LAUM for the "biennale du son, Le Mans Sonore 2022" [62]. A kink (anti-kink) topological soliton propagates by twisting in the clockwise (counterclockwise) direction. These solitons are called topological solitons because the structure of the propagation medium is modified after the soliton passes. As seen in Fig. 1.7, when two kink-solitons approach each other, they repel one another. This interaction causes them to decelerate as they move towards each other, and accelerate as they move away from each other. After the collision, the two kinks keep their amplitude and velocity and undergo a phase shift. Oppositely, a kink and an antikink attract each other. Depending on the initial velocities and energies, these interactions can lead to different outcomes such as elastic scattering, breather formation, or annihilation [55]. Elastic scattering means that the kink and antikink re-emerge after colliding with phase shifts as shown in Fig. 1.7.

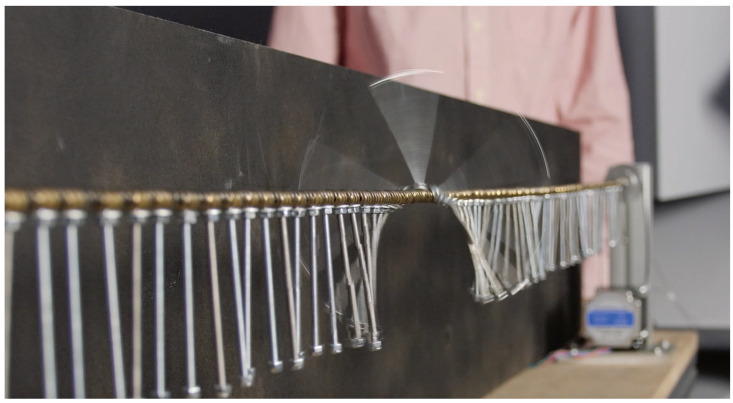

Figure 1.6: Propagation of kink-solitons along a chain of pendulums. This device can be used to observe linear waves or nonlinear waves like kink/anti-kink solitons and collisions, breather solitons, etc.

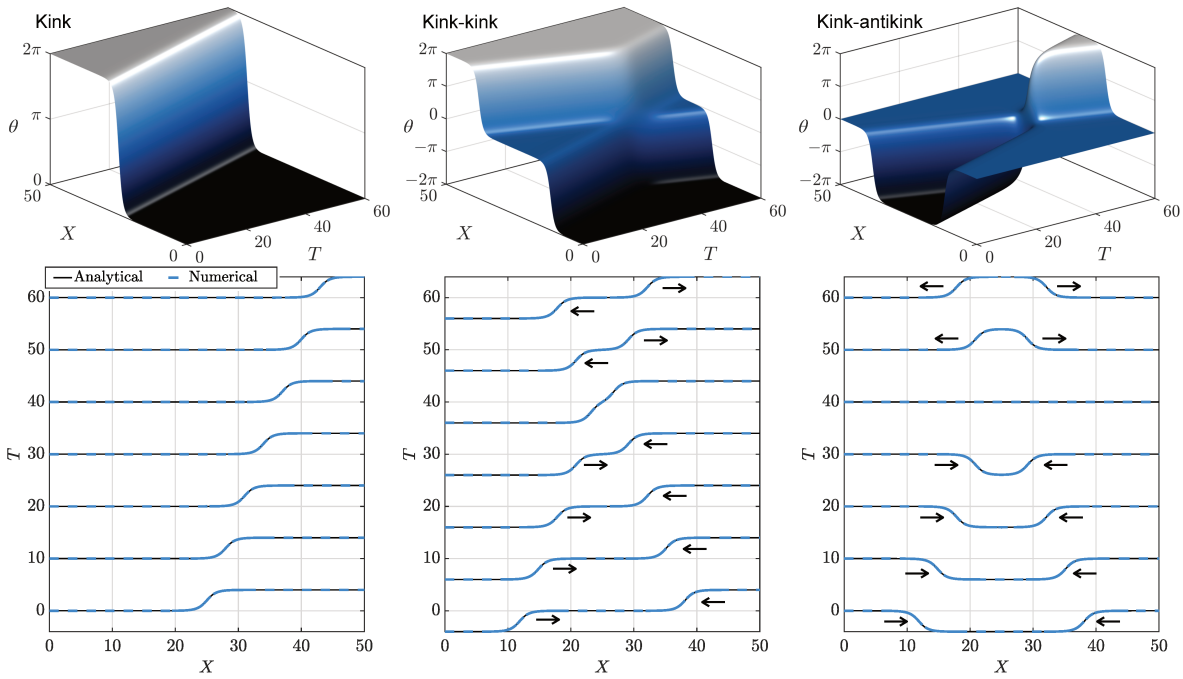

Figure 1.7: Numerical integration of the sine-Gordon equation using kink, kink-kink, and kink-antikink initial conditions.

In the low amplitude regime, the sine-Gordon equation is approximated by the nonlinear Klein-Gordon equation. In this equation, slowly varying envelope modulating waves can be observed and modeled by the nonlinear Schrödinger (NLS) equation, integrated in 1968 by V.E. Zakharov and A. B. Shabat [63]. They found exact solutions in the form of envelope solitons. The NLS equation found its applications in deep-water wave dynamics [64, 65, 51], electromagnetic waves in media with third-order nonlinearity [55], plasma

physics [66, 67], and acoustics [68].

1.4. Objectives and chapter sequences

In this PhD, we are interested in the propagation of nonlinear modulated waves in rotating element-based flexible mechanical metamaterials, see Sec. 1.2.3. Pulse vector solitons have already been studied and observed in such structures and present a close link with the nonlinear Klein-Gordon equation: the rotational displacement field is modeled by this equation in the continuous limit [7, 69]. These studies on pulse vector solitons are the foundation of our investigation, as they demonstrate a connection between the nonlinear KG equation and the equations of motion of our FlexMM. Additionally, since it is established that the NLS equation can describe the envelope of a wave propagating in the nonlinear KG equation [70, 71], we can anticipate observing phenomena specific to the NLS equation in the FlexMM such as modulation instabilities, bright/dark/breather solitons, etc., in the weakly nonlinear and dispersive regimes.

This dissertation is motivated by improving the knowledge of the nonlinear mechanical dynamic properties of FlexMMs, which would increase their potential applications, especially in discrete devices subject to continuous vibrations. Furthermore, FlexMMs offer a promising platform for studying new phenomena and investigating extreme events using continuous, modulated nonlinear waves. This could lead to significant advances in large-scale reconfiguration for example.

Chap. 2 presents the analytical and numerical methods used in subsequent chapters to study modulated wave propagation in FlexMMs. We introduce a simplified version of our FlexMM chain inspired by several works [39, 7, 8, 69], where the equation of motion reduces to a continuous nonlinear Klein-Gordon (KG) equation in the continuous limit. Finally, we demonstrate how this equation leads to a nonlinear Schrödinger equation, which describes the envelope of the wave train. The NLS bright soliton solution is particularly studied as an example.

In Chap. 3, the main objective is to study the phenomenon of modulational instability (MI) in nonlinear FlexMM. The study of MI aims to investigate the nonlinear evolution of modulated plane waves which is essential for comprehending the behavior of continuous waves in these flexible metamaterials. This foundational knowledge is crucial for advancing practical applications such as vibration damping and energy harvesting, where periodic signals are commonly encountered. Starting from a discrete, nonlinear, lump model that accurately describes the dynamics of FlexMMs, we derive an NLS equation for the slowly varying envelope of waves in the rotational degree of freedom. We then

analyze the conditions under which modulation instability of plane waves arises due to random perturbations. Finally, theoretical predictions are compared to numerical simulations of the full nonlinear lump model demonstrating how the coupling between the degrees of freedom of the particles and which mechanical parameters of the metamaterial (see section 3.2) can induce modulation instabilities.

Chap. 4 is dedicated to soliton solutions of the NLS equation: the bright and dark solitons. In the context of FlexMM, they are lattice envelope vector solitons. In Sec. 4.2, we present the nonlinear discrete lump model which was found to be relevant for describing the dynamical equations of FlexMMs. In section 4.3, we derive an effective NLS equation in the semi-discrete approximation for the slowly varying envelope of waves of the rotational degree of freedom (DOF). Using the semi-discrete approximation provides a valid model for any wavelength of the carrier waves, contrary to the development of Chap. 3. Sections 4.4 and 4.5 study the existence and dynamics of both bright and dark envelope vector solitons.

In chapter 5, we investigate the generation of extreme wave events in FlexMMs. We use the regularization of the gradient catastrophe process developed by A. Tovbis and M. Bertola for the nonlinear Schrödinger equation. According to this theory, Peregrine solitons can locally emerge in the semi-classical limit of the NLS equation. Using the effective NLS (eNLS) equation obtained in chapter 4, we compare the evolution of the dynamics of the FlexMMs with that of the NLS equation as a function of the initial conditions used.

Finally, in Chap. 6, the general conclusions and the main perspectives of the presented work are drawn.

2 | Waves in nonlinear lattices

Contents

Wave propagation through nonlinear lattice structures is a very active research topic that seeks to understand the complex interactions between the nonlinearity and periodicity of the medium. Rooted in fundamental questions concerning energy localization, solitons, and lattice vibrations, this field has evolved significantly since its inception, marked by seminal contributions and a deeper understanding of nonlinear phenomena.

As mentioned in chapter 1 Section I, FlexMMs are most often modeled using the lumped element approach, simplifying them to a lattice structure. This chapter aims to provide a clear and informative introduction to the analytical and numerical methods employed in subsequent chapters for studying modulated wave propagation in FlexMMs. To help comprehension, we will begin with a simplified problem where the equation of motion is reduced to a nonlinear Klein-Gordon (KG) equation. This simplified version of the system is not only a pedagogical model; it has recently been shown that this system can be used to create active metamaterials for generating and propagating unidirectional dissipative solitons [72].

First, we introduce a simplified version of the FlexMM we use in the upcoming chapters. Then, from the equation of motion, we demonstrate the derivation of a nonlinear KG equation using a continuous approximation model. Finally, we show how this equation leads to a nonlinear Schrödinger equation which describes the envelope modulated waves. The propagation of a nonlinear Schrödinger (NLS) bright soliton is chosen as an example to show the relevance of the derived NLS equation.

2.1. Flexible mechanical metamaterial: pinned rotating structure

This section introduces the mathematical model employed to depict the motion of our FlexMM and specifies the approximations used.

2.1.1. Lumped element approach

The structure under study in the following chapter is made of rigid particles (which can have different shapes), connected to their neighboring particles with soft elastic connections which are physically modeled by three linear springs: a longitudinal one with stiffness k_l, a shear one with shear stiffness k_s, and a bending one with bending stiffness k_θ. The soft and rigid parts can be modeled using the lumped element approach (see Fig. 2.1). We consider a line of N particles of size $2l$ periodically arranged, aligned (the static angle of particles is equal to 0), and pinned. In this case, only rotational motion can occur

while the longitudinal and transversal translations are blocked respectively on the x and y directions. Consequently, only one equation is needed to describe the rotational motion of the n-th particle θ_n.

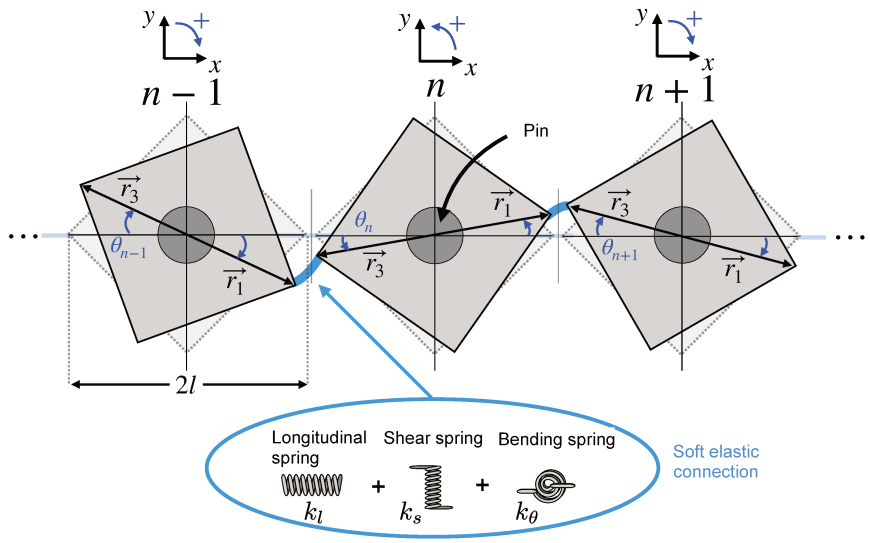

Figure 2.1: Geometry of the pinned structure. It comprises a total of N aligned rigid pinned particles, the n-th of which is connected to its direct neighbors $n-1$ and $n+1$ by soft elastic connections. Pins allow rotation but prevent translation.

To determine the forces acting on the n-th particle, it is necessary to estimate the vectors $\mathbf{r_1}(\theta_n)$ and $\mathbf{r_3}(\theta_n)$. They are of norm l and represent the distance and direction from the center of inertia of the particle, to its extremity, connected to the soft elastic joint. Consequently, these vectors are expressed as a function of the dynamical angle $\theta_n(t)$. Considering a single particle, the positions of its extremities are as follows,

$$\mathbf{r_1}(\theta_n) = \begin{pmatrix} l\cos\theta_n \\ (-1)^n l\sin\theta_n \end{pmatrix}, \qquad \mathbf{r_3}(\theta_n) = \begin{pmatrix} -l\cos\theta_n \\ -(-1)^n l\sin\theta_n \end{pmatrix}. \tag{2.1}$$

The $(-1)^n$ coefficient in front of the sine function comes from the orientation choice for the positive direction of the dynamical angle $\theta_n(t)$. Here, and in chapter 3, we define the positive direction of rotation alternatively for neighboring squares. If for the n-th particle the trigonometric rotation is considered as positive, the anti-trigonometric direction of rotation is considered as positive for the $n \pm 1$ ones, see Fig. 2.1. Due to the position of the vertices, the springs strain in both the longitudinal and transverse directions x and y is given by,

$$\begin{aligned}\mathbf{\Delta l_n} &= [\{\mathbf{r_3}(\theta_{n+1}) - \mathbf{r_3}(0)\} - \{\mathbf{r_1}(\theta_n) - \mathbf{r_1}(0)\}] \\ &= \begin{bmatrix} -l\cos\theta_{n+1} - l\cos\theta_n + 2l \\ -(-1)^{n+1} l\sin\theta_{n+1} - (-1)^n l\sin\theta_n \end{bmatrix},\end{aligned} \tag{2.2}$$

where $\mathbf{r_1}(0) = \mathbf{r_3}(0)$ are the static positions of the vectors equal to l in the x direction. At equilibrium, Eq. (2.2) shows that $\mathbf{\Delta l_n} = 0$. This is an approximation as in reality, the elastic links have a length d. For Eq. (2.2) to be valid, the particle extremities must be close to their neighbors, as presented in these FlexMMs [32]. In Eq. 4.2, the trigonometric terms model the shear rotation. For the bending rotation, we consider linear elasticity. As a result, rotational bending strain can be expressed as,

$$\Delta\theta_n = \theta_{n+1} + \theta_n\,, \tag{2.3a}$$

$$\Delta\theta_{n-1} = \theta_n + \theta_{n-1}\,. \tag{2.3b}$$

Combining the expressions of each elastic link elongation derived in Eqs. (2.2-2.3), the expression for the Hamiltonian of the system can be written,

$$H = \sum_{n=1}^{N} \frac{1}{2} J\dot{\theta}_n^2 + \sum_{n=1}^{N-1} \frac{1}{2} \|\mathbf{k}.\mathbf{\Delta l_n}\|^2 + \sum_{n=1}^{N-1} \frac{1}{2} k_\theta {\Delta\theta_n}^2\,, \tag{2.4}$$

with $\mathbf{k} = (\sqrt{k_l}\ \sqrt{k_s})$.

In this model (cf. Eq. (2.4)), it is considered that the soft elastic connections between vertices behave physically as follows. The bending moment linearly depends on the relative angles between two adjacent units, the longitudinal restoring force is proportional to the elastic elongation along the connector axis, and the shearing force is proportional to the elastic elongation projected orthogonally on the connector axis. A more general model could be implemented to include global rotation effects and the geometrical nonlinearity associated with large rotations. However, this might result in the equations of motion that are not easily treated analytically as we wish to do so below.

The first sum corresponds to the kinetic energy contribution, where J is the moment of inertia of the rigid particles. The second one corresponds to the traction/compression and shear deformations of the soft elastic connections $\mathbf{\Delta l_n}$. Finally, the third one is the contribution of the bending deformations of the soft elastic connections.

From the Hamiltonian Eq. (2.4) of the system, it is possible to find the equation governing

θ_n,

$$J\frac{\partial^2\theta_n}{\partial t^2} = -\frac{\partial H}{\partial \theta_n}\,. \tag{2.5}$$

Only direct neighbors of the n_{th} particle, i.e. $n \pm 1$, influence its dynamics. As a result, Eq. (2.5) is reduced to,

$$J\frac{\partial^2\theta_n}{\partial t^2} = -\frac{1}{2}\frac{\partial\|\mathbf{k}.\mathbf{\Delta l_n}\|^2}{\partial\theta_n} - \frac{1}{2}\frac{\partial\|\mathbf{k}.\mathbf{\Delta l_{n-1}}\|^2}{\partial\theta_n} - \frac{1}{2}k_\theta{\Delta\theta_n}^2 - \frac{1}{2}k_\theta{\Delta\theta_{n-1}}^2\,. \tag{2.6}$$

The equation of motion governing the rotation of the pinned chain is finally given by,

$$\begin{aligned} J\frac{\partial^2\theta_n}{\partial t^2} =& k_l l^2 \sin\theta_n\left(\cos\theta_{n-1} + 2\cos\theta_n + \cos\theta_{n+1} + 4\right) - k_s l^2\cos\theta_n\left(\sin\theta_{n-1}\right. \\ & \left. -2\sin\theta_n + \sin\theta_{n+1}\right) - k_\theta\left(\theta_{n-1} + \theta_n + \theta_{n+1}\right)\,. \end{aligned} \tag{2.7}$$

From the previous equation of motion, it can be deduced that the system contains a geometric nonlinearity, activated by the rotation of the rigid particles on the longitudinal and transversal axes. With the following normalized variables and parameters: the normalized time $T = t\sqrt{k_l}$, an inertial parameter $\alpha = l/\sqrt{J}$, and the stiffness parameters: $K_\theta = k_\theta/(k_l l^2)$ and $K_s = k_s/k_l$, the equation of motion Eq. (2.7) is written as,

$$\begin{aligned} \frac{1}{\alpha^2}\frac{d^2\theta_n}{dT^2} =& -K_\theta\left(\theta_{n-1} + 2\theta_n + \theta_{n+1}\right) + K_s\cos\theta_n\left[\sin\theta_{n-1} - 2\sin\theta_n + \sin\theta_{n+1}\right] \\ & -\sin\theta_n\left[4 - \cos\theta_{n-1} - 2\cos\theta_n - \cos\theta_{n+1}\right]\,. \end{aligned} \tag{2.8}$$

The continuum limit is employed in the next subsection to find analytical solutions to the equation of motion of the lattice Eq. (2.8).

2.1.2. Continuum limit

Considering lattice waves (cf. Eq. (2.8)) with sufficiently large wavelength compared to the unit cell distance, i.e. $\lambda \gg a$, one can apply the continuum limit. In this case, we can treat the discrete variable of the position x_n as a continuous variable X and derive,

$$\theta(X_n, T) = \theta_n(T)\,,\quad X_n = \frac{x_n}{a}\,. \tag{2.9}$$

The rotation of the masse pairs $n+1$ and $n-1$ is expressed using the following Taylor expansions,

$$\begin{aligned}
\theta_{n\pm1}(T) = \theta(X_{n\pm1},T) &\approx \theta|_{X_n,T} \pm \left.\frac{\partial\theta}{\partial X}\right|_{X_n,T} + \frac{1}{2}\left.\frac{\partial^2\theta}{\partial X^2}\right|_{X_n,T},\\
\cos\theta_{n\pm1}(T) = \cos\theta(X_{n\pm1},T) &\approx \cos\theta|_{X_n,T} \pm \left.\frac{\partial\cos\theta}{\partial X}\right|_{X_n,T} + \frac{1}{2}\left.\frac{\partial^2\cos\theta}{\partial X^2}\right|_{X_n,T},\\
\sin\theta_{n\pm1}(T) = \sin\theta(X_{n\pm1},T) &\approx \sin\theta|_{X_n,T} \pm \left.\frac{\partial\sin\theta}{\partial X}\right|_{X_n,T} + \frac{1}{2}\left.\frac{\partial^2\sin\theta}{\partial X^2}\right|_{X_n,T}.
\end{aligned} \tag{2.10}$$

Substituting equation (2.10) in (2.8), and keeping terms up to the third order, we find that the rotational degree of freedom is described by the following nonlinear KG equation,

$$\frac{\partial^2\theta}{\partial T^2} = C_1\frac{\partial^2\theta}{\partial X^2} - C_2\theta - C_3\theta^3\,. \tag{2.11}$$

The coefficients $C_1 = \alpha^2(K_s - K_\theta)$, $C_2 = 6K_\theta\alpha^2$ and $C_3 = 2\alpha^2$ depend on the physical parameters, α the inertial parameter and stiffness parameters K_s and K_θ.

2.2. Nonlinear Klein-Gordon equation

2.2.1. Low-amplitude limit, linear KG equation

The low-amplitude regime allows us to determine how waves propagate in lattices under the dispersion effect from the discreteness (periodicity). The dispersion relation, cf. Eq (2.14), which depends on the physical properties of the medium C_1 and C_2, establishes the relation between the angular and spatial ω, k frequencies. To find the dispersion relation, for example in the pinned structure defined in the previous section, it is necessary to linearize the effective continuous nonlinear KG equation that describes the system. First, we assume $\theta \ll 1$. The resulting linear KG equation writes,

$$\frac{\partial^2\theta}{\partial T^2} = C_1\frac{\partial^2\theta}{\partial X^2} - C_2\theta\,. \tag{2.12}$$

2.2.2. Dispersion relation and phase velocity

Within sight of the results of the next chapters, it is instructive to explain the difference between the KG equation and the simple wave equation regarding the propagation of pulses. Considering harmonic wave solutions,

$$\theta(x,t) = A\cos(kx-\omega t) = A\mathrm{Re}\left[e^{i(kx-\omega t)}\right]\,. \tag{2.13}$$

one gets the following linear dispersion relation,

$$\omega = \pm\sqrt{C_1 k^2 + C_2}\,, \tag{2.14}$$

which is depicted in Fig. 2.2. Due to the C_2 term, the KG exhibits a strong dispersion around $k = 0$. If $C_2 = 0$, the system becomes nondispersive and is reduced to a wave equation,

$$\frac{\partial^2\theta}{\partial X^2} - \frac{1}{c_0^2}\frac{\partial^2\theta}{\partial T^2} = 0\,, \tag{2.15}$$

characterized by a linear dispersion relation with a constant propagation velocity.

In this case, the phase velocity

$$v_\phi = \frac{\omega}{k}\,, \tag{2.16}$$

is equal to the propagation velocity $c_0 = \sqrt{C_1}$.

From Eq. (2.14), we note that the wavenumber k is imaginary for $\omega < \sqrt{C_2}$, that is $\omega_c = \sqrt{C_2}$ is a cutoff frequency. Below this cutoff frequency, the structure presents a gap: waves with a frequency in this region cannot propagate, they are evanescent.

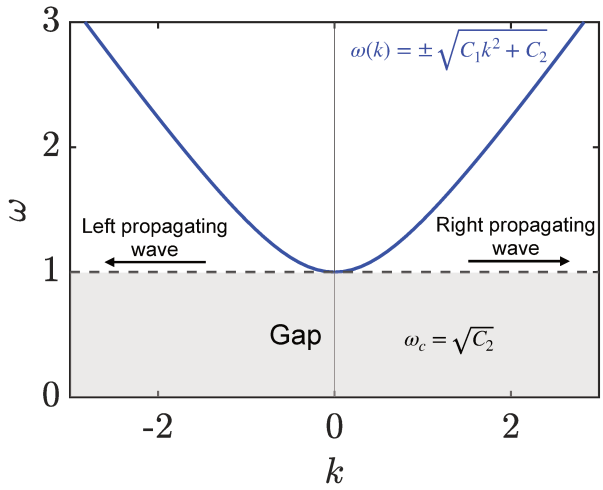

Figure 2.2: Dispersion relation of the Klein-Gordon equation for $C_1 = C_2 = 1$.

For dispersive waves, the phase velocity depends on the wavenumber k. A pulse propagating in a dispersive medium is a superposition of sinusoidal wave trains with different wavenumbers, each traveling with its own phase speed $v_\phi(k)$ given by Eq. (2.16). A pulse of amplitude A_0 initially defined with a given narrow width deforms its shape or disperses as it propagates, cf. Fig. (2.3)(a).

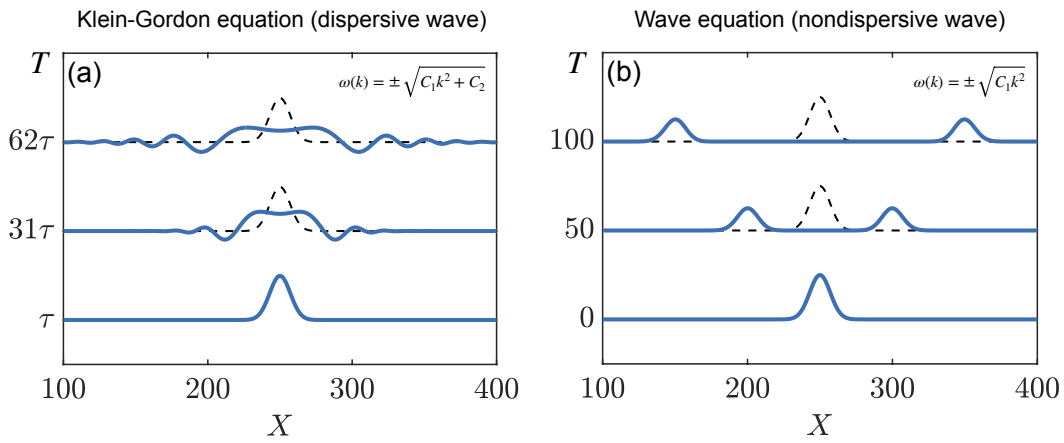

Figure 2.3: Pulse propagating at wavenumber $k = 0$ for $C_1 = 1$. In panel (a), $C_2 = 1$ so the system is dispersive, and the resulting wave oscillates in time with the period $\tau \approx 6.3$. For panel (b), $C_2 = 0$ so the system is nondispersive, and the resulting pulse is split into two pulses of amplitude $A = A_0/2$ translated with a constant velocity $\sqrt{C1} = 1$ on the left and right directions.

In the wave equation, a pulse or a wave pattern initially created with no initial velocity is split into two parts, each moving at a constant velocity to the right and left directions without deforming their shape over time, see Fig. 2.3(b). When $k = 0$ and for a nondispersive media ($\omega = 0$), there is no temporal oscillation. However, in the dispersive case described by the Klein-Gordon equation, temporal oscillations are present.

Numerical scheme to solve the KG equation

After deriving and studying the theoretical properties of the KG equation, we can dive into its numerical integration. Indeed, numerical integrations will have to be performed in the upcoming sections of this chapter.

The method employed to solve the KG equation consists of using a fourth-order Runge-Kutta algorithm to integrate the equation over time, while the second spatial derivative is computed with a centered second-order finite-difference scheme,

$$\frac{\partial^2\theta}{\partial X^2} = \frac{(\theta_{n+1} - 2\theta_n + \theta_{n-1})}{\Delta x^2} \,. \tag{2.17}$$

The Courant-Friedrichs-Lewy (CFL) (1928) condition must be used to ensure convergence of the numerical integration scheme [73]. The CFL condition places a limit between the theoretical velocity c_0 of the waves and the discretization along x and t and writes $c_0 < \frac{\Delta_x}{\Delta_t}$. It affirms that the propagation of the information in the numerical scheme should always

be faster than the velocity of waves inside the theoretical model. The space domain is of size $L = 500$, discretized with a $\Delta x = 0.1$ step for a total number of $N_x = 5000$ lattice points, and with free boundary conditions at both ends of the domain. The total time of integration is $T_f = 300$, with a time step $\Delta t = 0.05$. Here, for the chosen Δx and Δt, the CFL is equals 2.

Similar numerical simulations will be performed in the upcoming sections of this chapter, in particular on envelope soliton solutions of the nonlinear KG equation.

2.3. Envelope soliton solution of the nonlinear KG equation

This section aims to study modulated plane waves propagating in the nonlinear KG equation. First, the theoretical framework of modulated waves will be set. Then, it will be demonstrated with the help of the multiple-scales method, that the envelope of a modulated plane wave propagating in the KG equation can be described with an NLS equation, in the weakly nonlinear regime. Finally, the interaction of two phase-shifted propagating solitary waves will be studied in the previous NLS equation framework, completing the set of analytical tools and methods available for the next chapters of this manuscript.

2.3.1. Modulated waves and group velocity

First, let us define a plane wave modulated by an amplitude $A(x,t)$,

$$\theta(x,t) = A(x,t)e^{i(k_0 x - \omega_0 t)}\,, \tag{2.18}$$

where $\omega_0 = \omega(k_0)$ follows the dispersion relation of the medium.

Then, we can express the wave packet in the Fourier k-space. This new representation shows the superposition of a large number of plane waves with different amplitudes $\tilde{A}(k)$, which compose the wave packet,

$$\theta(x,t) = \frac{1}{2\pi}\int_{-\infty}^{+\infty} \tilde{A}(k)e^{i(kx-\omega(k)t)}dk\,. \tag{2.19}$$

Considering that the spectra $\tilde{A}(k)$ is narrow, the function $\omega(k)$ can be approximated as a Taylor series expansion around the central frequency ω_0 and higher order terms can be

neglected,

$$\omega(k) = \omega_0 + (k - k_0) \left.\frac{\partial \omega}{\partial k}\right|_{k=k_0} + \dots . \tag{2.20}$$

Eq. (2.20) is substituted into (2.19), obtaining the following result,

$$\theta(x,t) = e^{i(k_0 x - \omega_0 t)} \frac{1}{2\pi} \int_{-\infty}^{+\infty} \tilde{A}(k) e^{i(k-k_0)\left(x - \frac{\partial \omega}{\partial k} t\right)} dk \,, \tag{2.21}$$

which can be written as,

$$\theta(x,t) = A\left(x - \frac{\partial \omega(k_0)}{dk} t\right) e^{i(k_0 x - \omega_0 t)} \,. \tag{2.22}$$

Eq. (2.22) shows that the envelope function propagates with the following group velocity,

$$v_g = \frac{\partial \omega}{\partial k} \,, \tag{2.23}$$

at the corresponding wavenumber k_0, while the carrier moves at the phase velocity defined in Eq. (2.16).

In the case of a wave modulated by an envelope whose spectrum is continuous, e.g. a Gaussian function, see Fig. 2.4(a), the frequency content of the modulated plane wave corresponds to the continuous spectrum of the Gaussian envelope centered on the carrier wavenumber k_0, as displayed in Fig. 2.4(b)

For the linear KG equation Eq. (2.12), the group velocity is,

$$v_g = \frac{C_1 k}{\omega} \,. \tag{2.24}$$

2.3.2. Large amplitude plane wave

As seen in the low-amplitude limit, a linear equation has plane-wave solutions of the form,

$$\theta(x,t) = A e^{i(k_0 x - \omega_0 t)} + A^* e^{-i(k_0 x - \omega_0 t)} \,. \tag{2.25}$$

For a relatively large amplitude of the plane wave, as displayed in Fig. 2.5(a), the cubic nonlinearity of the nonlinear KG equation (C_3 coefficient) becomes significant (see Fig. 2.5(d)) and influences the evolution of the plane wave by modulating it, as presented in panel Fig. 2.5(b). The modulation resulting from the emergence of harmonics, visible in Fig. 2.5 (e-f), can persist until the original plane wave (see Fig. 2.5 (a)) is split into

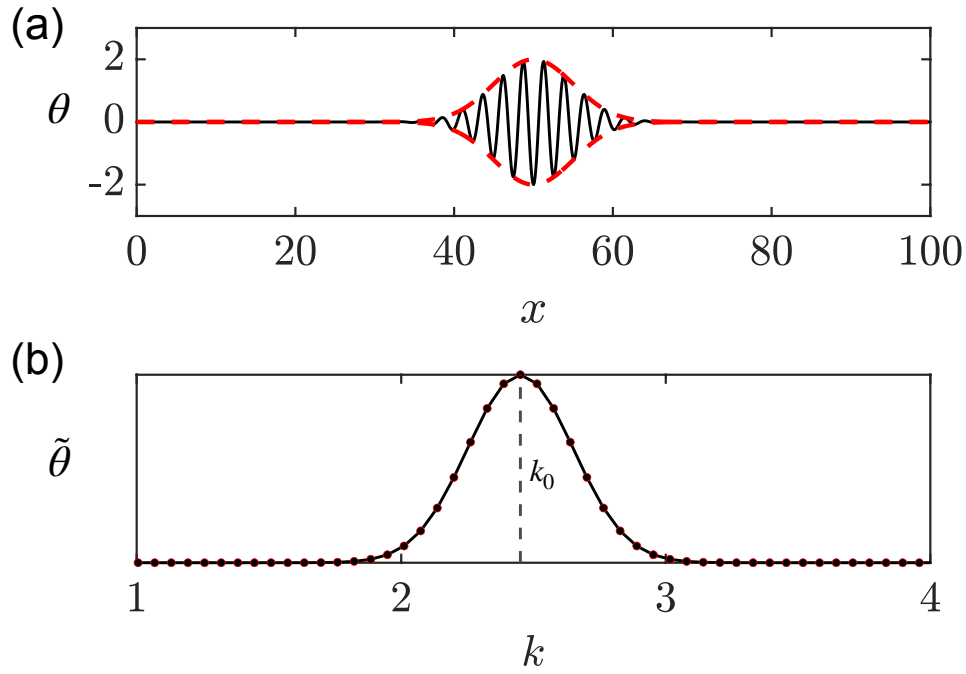

Figure 2.4: (a) Plane wave with a k_0 wavenumber, modulated by a Gaussian function. The black line is the carrier wave and the red dashed line is the envelope. (b) Spatial spectrum of the modulated wave.

wave packets with properties similar to solitons Fig. 2.5 (c). These coherent structures are thus composed of a carrier wave modulated by an envelope signal. They are termed envelope solitons.

In the next section, the multiple scales method [71, 70] will be employed to describe the evolution of weakly nonlinear envelope waves of the KG equation and predict the phenomenon observed in Fig. 2.5.

2.3.3. From the KG equation to the NLS equation

As we exhibited in section 2.1, weakly nonlinear long wavelength waves can be effectively described by the following nonlinear KG equation,

$$\frac{\partial^2\theta}{\partial T^2} - C_1\frac{\partial^2\theta}{\partial X^2} + C_2\theta - C_3\theta^3 = 0\ . \tag{2.26}$$

This equation can be rewritten using two linear operators $\hat{\mathcal{L}}$ and $\hat{\mathcal{N}}$ giving,

$$\hat{\mathcal{L}}[\theta] - \hat{\mathcal{N}}[\theta^3] = 0\ , \tag{2.27}$$

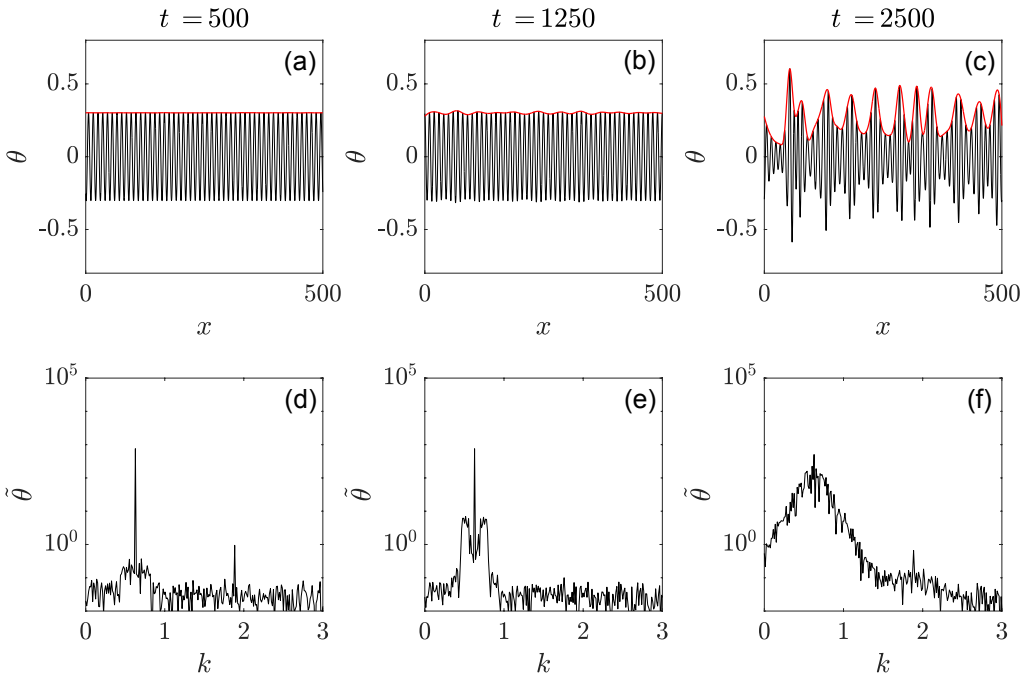

Figure 2.5: Representation of the modulation process of a plane wave, with wavenumber $k_0 = 0.63$, and corresponding spatial spectra at different times. (a) At $t = 500$, the plane wave is not modulated yet. Two pics are visible on the spectrum (d), the first one at $k = k_0 = 0.63$ (the original plane wave frequency), and the other at $k = 3k_0 = 1.89$, caused by the cubic nonlinearity of the nonlinear KG equation. (b) At $t = 1250$, the plane wave starts to be modulated from the generation of harmonics in the spectrum (e). (c) At $t = 2500$, more frequencies are generated around the original carrier frequency k_0 (f). The original plane wave is split into wave packets. The red line corresponds to the envelope $A(x, t)$ of the wave.

where $\hat{\mathcal{L}} = \frac{\partial^2}{\partial T^2} - C_1 \frac{\partial^2}{\partial X^2} + C_2$ and $\hat{\mathcal{N}} = C_3$.

We know that a modulated wave can be split into a carrier wave and an envelope. The carrier wave varies rapidly in space and time, while the envelope has a slower variation. Hereafter, we treat the fast and slow scales separately to derive an NLS equation that describes the dynamics of the modulated wave envelope.

Multiple-scales method

The multiple-scales method is an analytical tool used to construct uniformly valid approximations of the solutions of perturbation problems in which the solutions depend simultaneously on widely different scales. The original fast-scale X_0, T_0 is introduced for the carrier, and the slow-scale X_1, T_1, X_2, T_2 is introduced for the envelope description.

Each time and space scale is an independent variable proportional to a small scale coefficient $\epsilon^n \ll 1$, where n is the order number. We are looking for weakly nonlinear solutions, implying that we are only interested in the first order of cubic nonlinearity. It is thus sufficient to keep variables up to order ϵ^2,

$$X = X_0 + \epsilon X_1 + \epsilon^2 X_2 \,, \tag{2.28a}$$

$$T = T_0 + \epsilon T_1 + \epsilon^2 T_2 \,. \tag{2.28b}$$

The new independent variables imply the refinement of the differentials of X and T for the different scales X_i and T_i. Defining the notation $D_i = \frac{\partial}{\partial T_i}$ and similarly $D_{iX} = \frac{\partial}{\partial X_i}$, one can write,

$$\begin{aligned}
\frac{\partial^2}{\partial T^2} &= (D_0 + \epsilon D_1 + \epsilon^2 D_2 + ...)^2 = D_0^2 + 2\epsilon D_0 D_1 + \epsilon^2 (D_1^2 + 2 D_0 D_2) + ... \\
\frac{\partial^2}{\partial X^2} &= (D_{0X} + \epsilon D_{1X} + \epsilon^2 D_{2X} + ...)^2 = D_{0X}^2 + 2\epsilon D_{0X} D_{1X} + \epsilon^2 (D_{1X}^2 + 2 D_{0X} D_{2X}) + ... \,.
\end{aligned} \tag{2.29}$$

The differentials of X and T are defined in Eq. (2.29) so that the linear operator (cf. Eq. (2.27)) can be developed up to the second order with the new scales,

$$\begin{aligned}
\hat{\mathcal{L}} &= D_0^2 + 2\epsilon D_0 D_1 + \epsilon^2 \left(D_1^2 + 2 D_0 D_2 \right) \\
&\quad - C_1 \left[D_{0X}^2 + 2\epsilon D_{0X} D_{1X} + \epsilon^2 \left(D_{1X}^2 + 2 D_{X0} D_{X2} \right) \right] + C_2 \,, \\
&= \hat{\mathcal{L}}_0 + \epsilon \hat{\mathcal{L}}_1 + \epsilon^2 \hat{\mathcal{L}}_2 \,.
\end{aligned} \tag{2.30}$$

It can then be separated in orders of ϵ as follows,

$$\begin{aligned}
&\mathcal{O}(1) : \hat{\mathcal{L}}_0 = D_0^2 - C_1 D_{0X}^2 + C_2 \quad , \\
&\mathcal{O}(\epsilon) : \hat{\mathcal{L}}_1 = 2(D_0 D_1 - C_1 D_{0X} D_{1X}) \quad , \\
&\mathcal{O}(\epsilon^2) : \hat{\mathcal{L}}_2 = D_1^2 - C_1 D_{1X}^2 + 2(D_0 D_2 - C_1 D_{0X} D_{2X}) \quad .
\end{aligned} \tag{2.31}$$

The operator in front of the nonlinear term simply gives $\hat{\mathcal{N}} = C_3$.

We are looking for a solution θ under the form of a perturbative expansion,

$$\theta(X,T) = \sum_{n=1}^{N} \epsilon^n \theta_n(X_0, ..., X_N, T_0, ..., T_N) \ , \tag{2.32}$$

where the functions θ_n with $n = 1, ..., N$ are functions of the different scales X_n and T_n, see Eq. (2.28).

The previous developments can be brought together to write the different orders of the nonlinear Klein-Gordon equation up to the first order of nonlinearity (order ϵ^3) as follows,

$$\mathcal{O}(\epsilon) : \hat{\mathcal{L}}_0\theta_1 = 0 \ , \tag{2.33a}$$

$$\mathcal{O}(\epsilon^2) : \hat{\mathcal{L}}_0\theta_2 + \hat{\mathcal{L}}_1\theta_1 = 0 \ , \tag{2.33b}$$

$$\mathcal{O}(\epsilon^3) : \hat{\mathcal{L}}_0\theta_3 + \hat{\mathcal{L}}_1\theta_2 + \hat{\mathcal{L}}_2\theta_1 - \hat{\mathcal{N}}\theta_1^3 = 0 \ . \tag{2.33c}$$

The equations will now be solved at each order.

Order ϵ, linear KG equation

Eq. (2.33a) at order ϵ is the linear KG equation. Hence, we are looking for a solution in the form of a modulated plane wave, described by the fast coordinates (X_0, T_0), and an envelope that evolves according to slow coordinates (X_1, T_1, X_2, T_2). Following the expression of the linear operator,

$$\theta_1 = A(X_1, T_1, X_2, T_2)e^{i\sigma(X_0,T_0)} + A^*(X_1, T_1, X_2, T_2)e^{-i\sigma(X_0,T_0)} \ , \tag{2.34}$$

with $\sigma = kX_0 - \omega T_0$, and where $*$ denotes conjugation.

At first order, cf. Eq. (2.33a),

$$-\omega^2\theta_1 + C_1k^2\theta_1 + C_2\theta_1 = 0 \ , \tag{2.35}$$

we recover the dispersion relation of the linear KG equation (see Eq. 2.14).

Order ϵ^2, solvability condition

Then, the second order of the equation (Eq. (2.33b)) leads to the following,

$$\hat{\mathcal{L}}_0\theta_2 = 2i\omega\frac{\partial A}{\partial T_1}e^{i\sigma} + 2iC_1k\frac{\partial A}{\partial X_1}e^{i\sigma} + \text{c.c} \, . \tag{2.36}$$

Eq. (2.36) is a linear equation with source terms proportional to $e^{\pm i\sigma}$. These source terms will generate secular terms which put the linear operator $\hat{\mathcal{L}}_0$ in resonance and blow up after a long time. The perturbation scheme fails and a solvability condition on A must be defined to prevent secular terms from occurring. This condition is met when the source terms of Eq. (2.36) cancel each other out,

$$\frac{\partial A}{\partial T_1} + v_g \frac{\partial A}{\partial X_1} = 0\,, \tag{2.37}$$

and reciprocally for A^*. Due to the removal of the secular term (see Eq. (2.37)), the second order equation Eq. (2.36) becomes,

$$\hat{\mathcal{L}}_0 \theta_2 = 0\,. \tag{2.38}$$

To solve this equation, we choose the trivial solution $\theta_2 = 0$ because the nontrivial solution would be equivalent to θ_1 due to the joint operator $\hat{\mathcal{L}}_0$, see Eq. (2.33a). It will generate a new unknown amplitude function that can be included in the A field of the plane wave at ϵ order.

Order ϵ^3, nonlinear Schrödinger equation

Finally, considering $\theta_2 = 0$, the third-order equation becomes,

$$\hat{\mathcal{L}}_0 \theta_3 = -\hat{\mathcal{L}}_2 \theta_1 + C_3 \theta_1^3\,. \tag{2.39}$$

We observe that the resulting Eq. (2.39) is now nonlinear. As for the previous equation at order ϵ^2, on the right-hand side of Eq. (2.39), secular terms arise, proportional to $e^{i\sigma}$. First of all $\hat{\mathcal{L}}_2 \theta_1$ is secular because θ_1 is resonating with the homogeneous solution but other resonant terms are present in the nonlinear term $C_3\theta_1^3$. θ_1 is a complex function which can be written as $\theta_1 = \tilde{\theta_1} + \tilde{\theta_1}^*$. We note that every equation is symmetric with regards to the complex conjugate $\tilde{\theta_1}^*$. Deriving the set of equations for $\tilde{\theta_1}$ leads to the following,

$$\begin{aligned} \theta_1^3 &= \tilde{\theta_1}^3 + 3|\tilde{\theta_1}|^2 \tilde{\theta_1}\,, \\ &= A^3 e^{3i\sigma} + 3|A|^2 A e^{i\sigma}\,. \end{aligned} \tag{2.40}$$

Eq. (2.40) exposes that the cubic term of Eq. (2.39) generates a secular term and a non-secular driving term $e^{i3\sigma}$ [1]. Substituting θ_1 from Eq. (2.34) and θ_1^3 from Eq. (2.40),

[1] The solution at order ϵ^3 is therefore of the type: $\theta = \epsilon(Ae^{i\sigma} + \text{c.c}) + \epsilon^3(Be^{3i\sigma} + \text{c.c}) + \mathcal{O}(\epsilon^4)$.

Eq. (2.39) becomes,

$$\hat{\mathcal{L}}_0 u_3 = \left(-D_1^2 A + C_1 D_{1X}^2 A + 2i\omega D_2 A + 2ikC_1 D_{2X} A + 3C_3|A^2|A\right) e^{i\sigma} + C_3 A^3 e^{3i\sigma} \,. \tag{2.41}$$

Resonating terms are obtained and a solvability condition can be derived,

$$-D_1^2 A + C_1 D_{1X}^2 A + 2i\omega D_2 A + 2ikC_1 D_{2X} A + 3C_3|A^2|A = 0\,. \tag{2.42}$$

It is possible to simplify the expression of Eq. (2.42) using the variables $\xi_n = X_n - v_g T_n$, $\tau_n = T_n$, i.e., a reference frame moving at the group velocity v_g. The differentiation of the co-moving coordinates ξ_n and τ_n can be computed for each scale n. This leads to,

$$\begin{aligned} \frac{\partial}{\partial X_n} &= \frac{\partial}{\partial \xi_n}\,, & \frac{\partial}{\partial T_n} &= -v_g \frac{\partial}{\partial \xi_n} + \frac{\partial}{\partial \tau_n}\,, \\ \frac{\partial^2}{\partial {X_n}^2} &= \frac{\partial^2}{\partial \xi_n^2}\,, & \frac{\partial^2}{\partial {T_n}^2} &= \frac{\partial}{\partial {\tau_n}^2} - 2v_g \frac{\partial^2}{\partial \xi_n \tau_n} + v_g^2 \frac{\partial^2}{\partial {\xi_n}^2}\,. \end{aligned} \tag{2.43}$$

In the new system of coordinates, the solvability condition cf. Eq.(3.13) becomes,

$$\frac{\partial A}{\partial \tau_1} = 0\,, \tag{2.44}$$

and the nonlinear Schrödinger equation finally appears from Eq. (2.42),

$$i\frac{\partial A}{\partial \tau_2} + \frac{(C_1 - v_g^2)}{2\omega}\frac{\partial^2 A}{\partial \xi_1^2} + \frac{3C_3}{2\omega}|A^2|A = 0\,. \tag{2.45}$$

This equation is useful to describe approximate low amplitude envelope solutions of the KG equation.

2.3.4. Bright soliton and collisions

As an example of the usefulness of the above method and the derived NLS equation, this subsection studies the collision of two bright solitons, which are exact solutions of the NLS equation and approximate solutions of the nonlinear Klein-Gordon equation with cubic nonlinearity. Collisions between solitons propagating in the NLS equation are known to be nearly perfectly elastic, meaning they occur without any change in shape and velocity. However, as a result of the collision, a shift in position and time occurs [53]. Depending on the phase shift between the two colliding solitons, they can overlap, resulting in a simple linear superposition, or repel each other.

The first part of this work presents the procedure to go from the KG to the NLS equation, assuming plane wave solutions under the small amplitude approximation. By returning to the (X, T) scale, the solutions of the NLS equation can be used as envelope solutions for the nonlinear KG equation.

Single bright soliton

From the previous part, we have found that the envelope of modulated waves propagating in the KG equation in the weakly nonlinear regime can be described by the NLS equation,

$$i\frac{\partial A}{\partial \tau_2} + P\frac{\partial^2 A}{\partial \xi_1^2} + Q|A|^2 A = 0 \,, \tag{2.46}$$

where

$$P = \frac{(C_1 - v_g^2)}{2\omega} \qquad \text{and} \qquad Q = \frac{C_3}{2\omega} \,, \tag{2.47}$$

are two coefficients which depends on C_1, C_2 and C_3, of the KG equation. As we are interested in the bright soliton solution, the NLS equation is studied in its focusing case $PQ > 0$. Next, starting from the known form of the NLS bright soliton [53] we have,

$$A(\xi_1, \tau_2) = A_0 \text{sech}\left[A_0\sqrt{\frac{Q}{2P}}\xi_1\right] e^{i\frac{QA_0^2}{2}\tau_2} \,, \tag{2.48}$$

where A is the amplitude and ξ_1, τ_2 are coordinates defined in the derivation of NLS. A can also be expressed in the slow coordinates system,

$$A(X_1, T_1) = A_0 \text{sech}\left[A_0\sqrt{\frac{Q}{2P}}\,(X_1 - v_g T_1)\right] e^{i\frac{QA_0^2}{2}T_2} \,, \tag{2.49}$$

leading to the latter approximate solution of the Klein-Gordon equation. At order ϵ we have,

$$\theta(X,T) = 2\epsilon A_0 \text{sech}\left[\epsilon A_0 \sqrt{\frac{Q}{2P}}\,(X - v_g T)\right] \cos\left[kX - \left(\omega - \epsilon^2 \frac{Q A_0^2}{2}\right) T\right] \ . \tag{2.50}$$

The nonlinear KG equation is a second-order partial differential equation. Consequently, two initial conditions are necessary to initialize the numerical integration scheme: the position $\theta(X, T = 0)$ and its corresponding velocity $\dot{\theta}(X, T = 0)$. Assuming $C_1 = C_2 = 1$ and $C_3 = \frac{1}{2}$ and $A_0 = 1$. The initial conditions are expressed,

$$\theta(X,0) = 2\epsilon \text{sech}\left[\frac{\epsilon}{2\sqrt{1-v_g^2}}(X - X_0)\right] \cos(kX) \ , \tag{2.51}$$

and,

$$\begin{aligned}\dot{\theta}(x,0) = &\frac{\epsilon^2 v_g}{\sqrt{(1-v_g^2)}} \tanh\left[\frac{\epsilon}{2\sqrt{1-v_g^2}}(X - X_0)\right] \text{sech}\left[\frac{\epsilon}{2\sqrt{1-v_g^2}}(X - X_0)\right] \cos(kX) \\ &+ 2\epsilon\left(\omega - \frac{\epsilon^2}{8\omega}\right) \text{sech}\left(\frac{\epsilon}{2\sqrt{1-v_g^2}}(X - X_0)\right) \sin(kX) \ .\end{aligned} \tag{2.52}$$

Numerical simulations are carried out based on the numerical scheme introduced in Sec. 2.2.2. The wavenumber chosen for the simulations is $k = 1$ which implies that $v_g \approx 0.71 <$ CFL (cf. Eq. (2.24)) and a focusing NLS equation ($PQ > 0$). The resulting bright soliton propagation initially excited using Eqs (2.51-2.52) is displayed in Fig. 2.6. In panel (a), the solitary wave propagates, keeping its form and velocity. The envelope is an exact solution of NLS and the propagating wavepacket is an approximate solution of the KG equation. As displayed in panel (b), theory and numerics are consistent. Nevertheless, the limits of our approximation can be tested, choosing $\epsilon = 0.5$ for instance, yielding the results revealed in Fig. 2.7. Although a localized wavepacket is still found to propagate in the KG lattice, the theoretical prediction deviates from the numerical results.

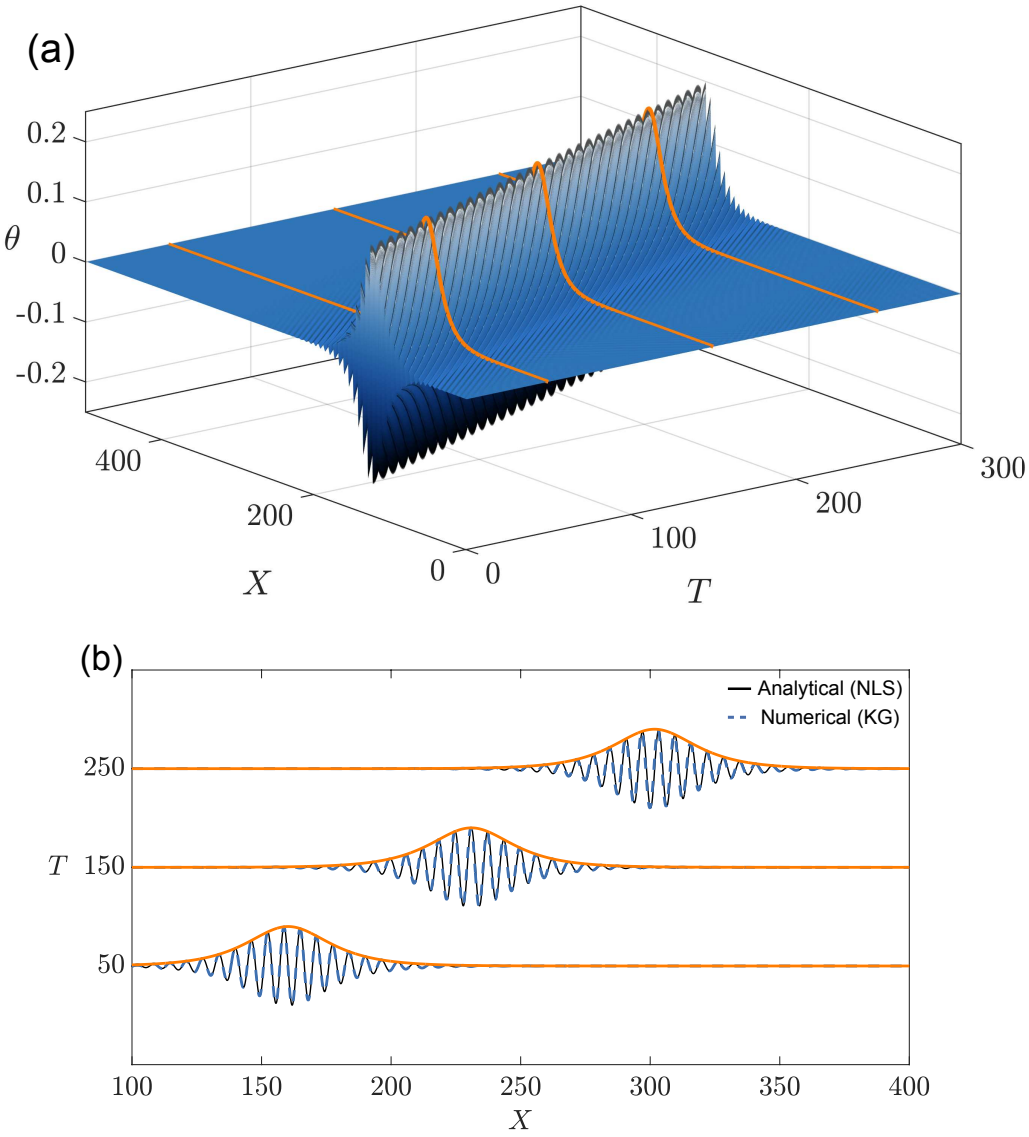

Figure 2.6: Bright soliton propagation regarding time and space initially at the position $X_0 = L/4$. In panel (a) the full evolution of the soliton is represented while in panel (b) only at a few particular times $T = 50, 150, 250$, which allows us to compare the numerical result of the KG nonlinear equation with the NLS analytical solution. The numerical parameters employed are $\epsilon = 0.1$, $\Delta x = 0.1$, $\Delta t = 0.05$.

Collision of two bright solitons

As introduced at the beginning of this section, solitons of the NLS equation collide nearly elastically except for the phase [53]. During the collision, the two colliding solitons merge with each other before separating out. However, depending on the phase shift, merging is not the same.

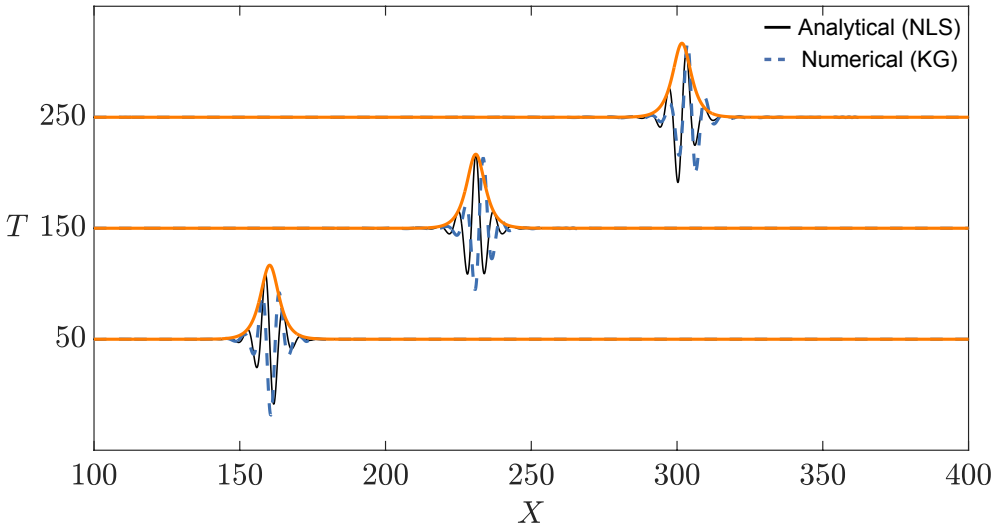

Figure 2.7: Bright soliton propagation in time and space initially at position $X_0 = L/4$. In panel (a), the full evolution of the soliton is represented while in panel (b), only a few particular times $T = 50, 150, 250$ are represented. This allows us to compare the numerical result of the nonlinear KG equation with the NLS analytical solution. The numerical parameters employed are $\epsilon = 0.5$, $\Delta x = 0.1$, $\Delta t = 0.05$.

Here, using the multiple scales method, we show that similar interactions can be observed for the KG equation. Let us assume the sum of two bright solitons propagating in opposite directions by choosing $k_{1/2} = \pm k$, with $X_{01} = \frac{L}{4}$, $X_{02} = \frac{3L}{4}$ and $\epsilon = 0.1$ with the same phase $\Delta\phi = 0$. This leads to the following representations in time and space, see Fig. 2.8. This solution corresponds to two independent solitons at $T = 0$, that collide around $T \approx 125$. After a strong nonlinear interaction, they recover their initial shapes and resurge intact from the collision.

However, depending on the phase shift between the two solitons, their interaction is different. Fig. 2.9 represents two colliding bright solitons for four chosen values of phase-shifts $\Delta\phi$. In-phase ($\Delta\phi = 0$) collision is translated into a strong peak of amplitude at the middle of the collision. When out-of-phase ($\Delta\phi = \pi$), they appear to repel each other while they still actually pass through one another. For intermediate phase shifts $\Delta\phi = \pi/2$ and $3\pi/2$, the evolution is similar to an in-phase collision, with a peak of amplitude this time shifted towards the left (right) for $\pi/2$ ($3\pi/2$) for the collision center.

The two wavepackets propagate and collide elastically. Nevertheless, regardless of the phase shift, their trajectories highlight the particle-like property of solitons which experience a position shift after their collision. The theoretical and numerical results are in

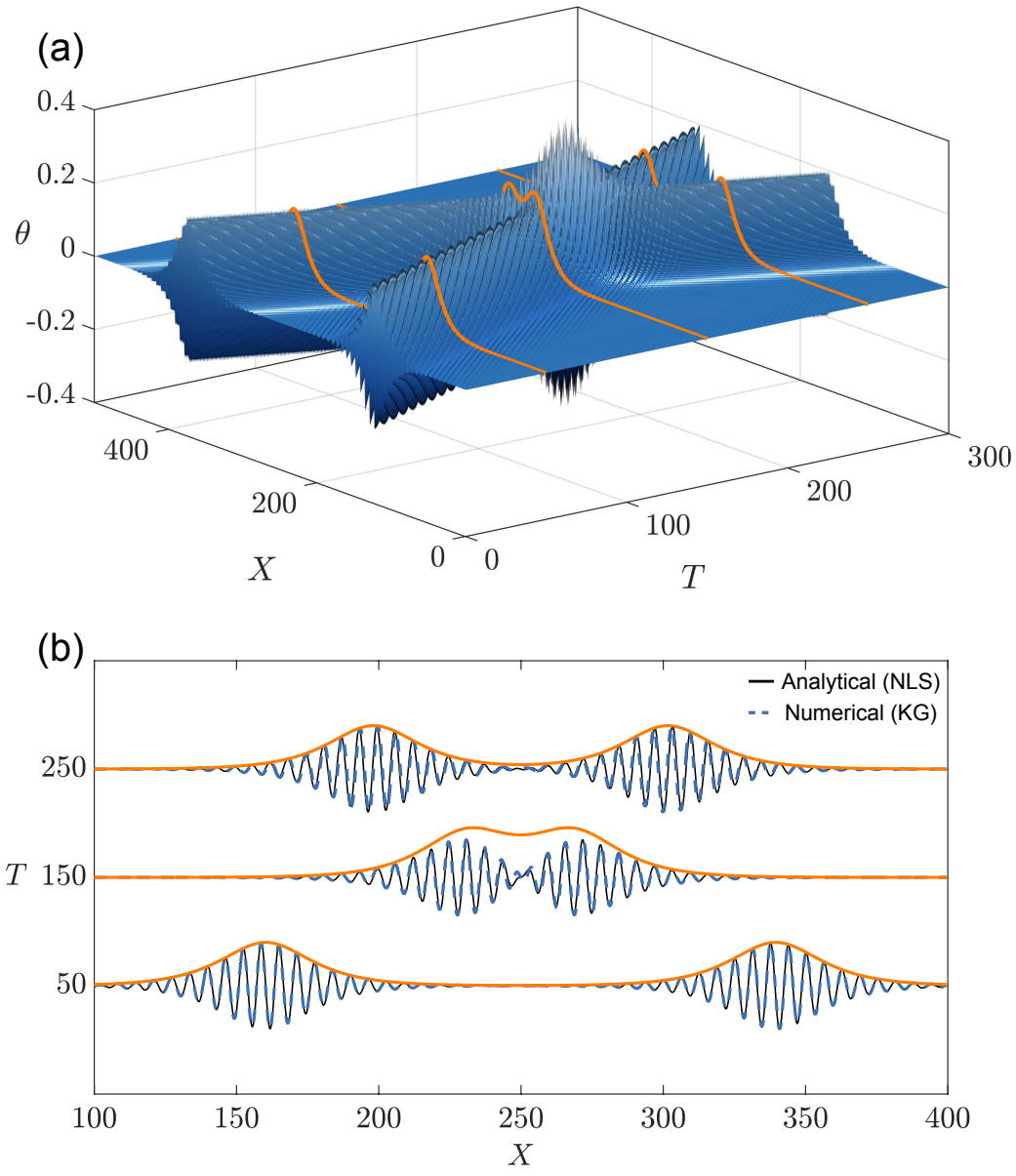

Figure 2.8: Two colliding bright solitons of the same amplitude, phase, and velocity v_g, propagating in opposite directions, $k_{01} = 1$ and $k_{02} = -1$ regarding time and space. They are initially at position $X_{01} = L/4$ and $X_{02} = 3L/4$. In panel (a), the full evolution of the solitons is represented while in panel (b), it is only represented at a few particular times $T = 50, 150, 250$. This allows us to compare the numerical result of the KG nonlinear equation with the NLS analytical solution. The numerical parameters employed are $\epsilon = 0.1$, $\Delta x = 0.1$, $\Delta t = 0.05$.

perfect agreement in this low amplitude (weakly nonlinear) regime.

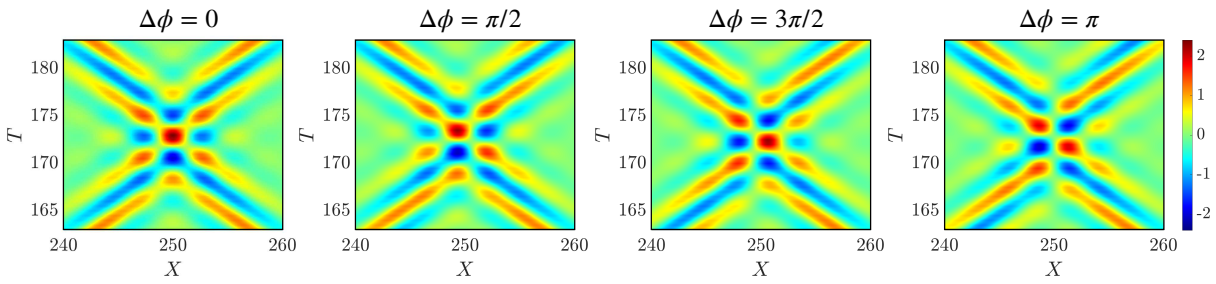

Figure 2.9: Zoom on the spatio-temporal dynamics of the collision of two identical solitons of amplitude $A_0 = 6$, the rest of the parameters are identical to Fig. 2.8. This figure shows the impact of the phase shift on the collision.

2.4. Conclusions

In this pedagogical chapter, we have introduced multiple analytical and numerical tools useful for the upcoming studies of this thesis. We have applied these methods to a simple system, the pinned rotating square structure, where each particle can only rotate. We have shown that for sufficiently large wavelengths, the wave dynamics in this lattice can be described by the nonlinear KG equation. As this equation has been extensively studied [74], it is of pedagogical interest to understand the dynamics of this system. It is also well known that low amplitude modulated wave propagation can be described by a nonlinear Schrödinger equation. To this end, we have outlined the steps involved in obtaining this equation, describing the spatial and temporal evolution of the modulated wave envelope. With the concepts now presented, a more complex structure can be studied by "unpinning" the rigid particles.

3 | Modulation instability in nonlinear flexible mechanical metamaterials

By: Antoine Demiquel, Vassos Achilleos, Georgios Theocharis, Vincent Tournat. Published in Physical Review E, on May 16 2023. DOI: 10.1103/PhysRevE.107.054212.

Contents

In this chapter, we study modulation instabilities (MI) in a one-dimensional chain configuration of a flexible mechanical metamaterial (FlexMM). Using the lumped element approach, FlexMMs can be modeled by a coupled system of discrete equations for the longitudinal displacements and rotations of the rigid mass units. In the long wavelength regime, and applying the multiple-scales method we derive an effective nonlinear Schrödinger equation for slowly varying envelope rotational waves. We are then able to establish a map of the occurrence of MI to the parameters of the metamaterials and the wavenumbers. We also highlight the key role of the rotation-displacement coupling between the two degrees of freedom in the manifestation of MI. All analytical findings are confirmed by numerical simulations of the full discrete and nonlinear lump problem. These results provide interesting design guidelines for nonlinear metamaterials offering either stability to high amplitude waves, or conversely being good candidates to observe instabilities.

3.1. Introduction

In the context of nonlinear waves, flexible mechanical metamaterials have recently emerged as a rich and versatile platform, opening the way for fundamental studies and potential applications [48]. Such flexible mechanical metamaterials (FlexMMs) can be defined as artificial compliant structures able to support large deformations and mechanical instabilities leading to new modes of functionality [31]. As a result, a plethora of original quasi-static behaviors and functions have already been reported, with applications to soft robotics [46], structure reconfigurability [75] or mechanical logic devices [32, 33, 76], as examples. In addition and more recently, the study of their dynamic properties has revealed that the nonlinearity is most often geometric in nature, resulting from large local deformations, which makes the nonlinear dynamic response governed by the architecture and therefore controllable [48]. This latter possibility opens the way to targeting specific dynamical properties, which have been known to be described by existing fundamental equations (such as nonlinear Klein-Gordon equations found in [39]) or which could illustrate and reveal new relevant dynamic equations. FlexMMs have also the potential of offering realizable configurations for testing exciting concepts or processes such as those encountered in time crystals [77, 78], in active metamaterials [79, 80] or for micropolar elasticity of mechanical metamaterials [81].

Up to now, the specific behaviors of the reported FlexMM designs could be accurately modeled as rigid units able to translate and rotate, connected with highly compliant springs of longitudinal, shear, and bending nature. On the one hand, the derived non-

linear and discrete equations of motion for multiple degrees of freedom can be efficiently solved by numerical integration [48]. On the other hand, several steps towards analytical solutions can be taken, including the consideration of periodicity, long wavelength compared to the lattice period, and expansions to first-order nonlinear and dispersive terms, for instance. A review of the main nonlinear wave processes and corresponding equations in FlexMM reported to date can be found in [48]. These include among others the observation of mechanical vector solitons, their interactions and tuning [39, 7, 48], the observation of cnoidal waves [50] and of transition waves [75, 32, 33, 76]. However, nonlinear modulated waves in FlexMM is an unexplored field. Many interesting wave phenomena are expected to be revealed, including the manifestation of modulation instability (MI) and the resulting formation of localized waves such as envelope solitons or breathers [82, 83, 84]. Beyond these fundamental interests, understanding the continuous wave dynamics of non-linear flexible metamaterials is a key step before analyzing driven-damped problems and implementing these for practical applications such as, e.g., vibration damping or energy harvesting, where periodic signals are often encountered.

The phenomenon of MI has attracted significant research interest in a range of different wave systems, both continuum (water surface [64, 65, 51], plasmas [67], optical fibers [85, 86], Bose-Einstein condensates [87]) and discrete (electrical transmission lines [66], granular chains [88]) described by the universal nonlinear Schrödinger equation (NLSE) [73, 71, 89]. MI analysis conventionally describes the early (linear) stage of the exponential growth of perturbations of an unstable plane wave background [85, 86, 90, 91, 92, 93]. Recently, a renewed interest in MI has appeared, motivated by the search for extreme waves, and has led to the analysis of various initial conditions not limited to plane waves as well as to the study of the subsequent nonlinear stages of instability beyond the initial linear stage. [94, 95, 96]. Along these lines, numerous theoretical and experimental works in water wave tanks and optical fibers appeared in the literature [65, 51, 97, 98, 99, 100, 101, 102, 88, 103, 84].

It is the main objective of this chapter to study the phenomenon of MI in nonlinear FlexMM. To do so, starting from a discrete, nonlinear lump model, which was found to describe well the dynamics of FlexMM, we derive an NLS equation for the slowly varying envelope of waves of the rotational degree of freedom. Then, we analyze under which conditions, the modulation instability of plane waves emerges by random perturbations. We finally compare the theoretical results with numerical simulations of the full nonlinear lump model. We show that, via an initial condition problem, the coupling between the degrees of freedom of the particles as well as the mechanical parameters of the metamaterial (see section 3.2), can allow modulation instability to occur and under which conditions.

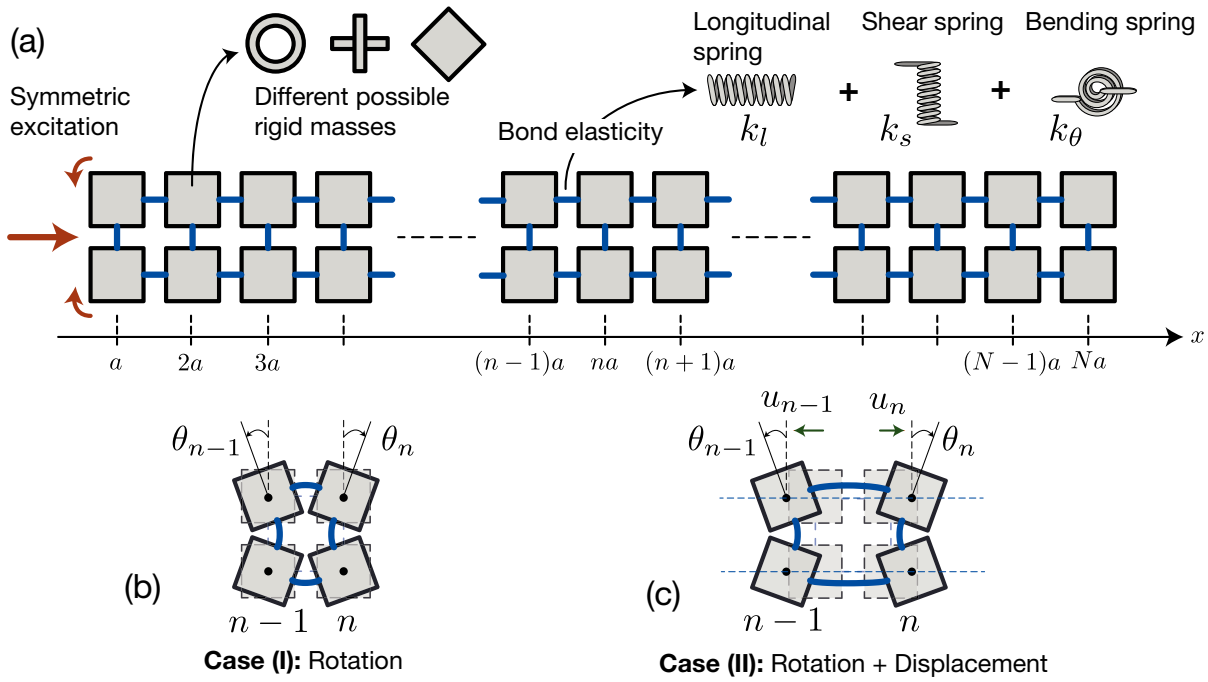

Figure 3.1: (a) Sketch of the chain configuration periodic FlexMM under consideration. It is composed of two rows of rigid mass units (gray squares) linked by elastic connectors (thick, blue lines) extending along the x-direction with a lattice constant α. The rigid units can be of various shapes (for example crosses, spheres, cubes) and are characterized by a mass m and a moment of inertia J. The elastic bonds (for example highly flexible plastic films) are characterized by three effective stiffness. We consider symmetric movements relative to the horizontal symmetry axis of the system. The displacements of the n and $n-1$ particles from the equilibrium position are shown in panels (b) and (c) for the two different considered cases. In panel (b) the mass units can only rotate, case (I) while in panel (c), the mass units can both rotate and longitudinally translate, case (II).

Note that in this theoretical and numerical study, damping is not considered. The latter is expected to affect substantially the dynamic behavior of FlexMM subjected to continuous excitation in experiments, and requires solving driven-damped problem types. Such problems are beyond the scope of this chapter but could constitute the next steps in order to fully describe experimental results and lead to applications.

3.2. Properties and modeling of the considered Flexible Mechanical Metamaterial

3.2.1. Problem position and modeling of the structure

The considered structure is inspired by the flexible Lego® chain implemented in ref. [7] and it consists of rigid units (an assembly of Lego® bricks), that are linked to the next neighbors by highly flexible plastic films. A periodic chain can then be constructed by connecting pairs of units along one direction as shown in Fig. 3.1(a). The plastic films connecting the rigid bodies are physically modeled by massless springs. Three springs are needed to represent the plastic film connections, a longitudinal spring with stiffness k_l, a shear spring with a shear stiffness k_s, and a bending spring with a bending stiffness k_θ. Two rows of masses were originally used in ref. [7] because this chain configuration possesses a symmetry axis ensuring symmetry of the motion and no experimental buckling of the chain out of this axis. The motion takes place in the plane of the chain and in the general case, each mass should have 3 degrees of freedom, one rotation, and two displacements. In the context of soliton propagation [7, 39], it has been shown numerically and experimentally that ignoring the transversal displacement is a reasonable assumption. Indeed, the numerically and experimentally observed transversal displacement amplitude is an order of magnitude smaller than the longitudinal one. A 2-degree-of-freedom model was therefore used for this system and could be used as a starting point for obtaining relevant analytical solutions.

In the present study, we also ignore the transversal displacements and we consider two cases. Case (I), Fig. 3.1(b), where each rigid unit is free only to rotate (thus is described by one DOF θ), and case (II), Fig. 3.1(c), where each rigid unit both rotates and is longitudinally displaced (thus is described by two DOFs θ and u). Based on the mirror symmetry of the two lines configuration along the y-axis, we look for symmetric excitations for which the two rigid units of each column move along x with the same amount and rotate at an opposite angle.

As done in [7], a positive direction of rotation is from now on defined alternately for neighboring units since the natural rotation is alternated, upon static compression or long-wavelength propagation. The corresponding normalized equations of motion for the n-th column are then written [7],

$$\begin{aligned}\frac{\partial^2 U_n}{\partial T^2} &= U_{n+1} - 2U_n + U_{n-1} - \frac{\cos\theta_{n+1} - \cos\theta_{n-1}}{2},\\ \frac{1}{\alpha^2}\frac{\partial^2 \theta_n}{\partial T^2} &= -K_\theta\left(\theta_{n+1} + 4\theta_n + \theta_{n-1}\right) + K_s \cos\theta_n \left[\sin\theta_{n+1} + \sin\theta_{n-1} - 2\sin\theta_n\right]\\ &\quad - \sin\theta_n \left[2\left(U_{n+1} - U_{n-1}\right) + 4 - 2\cos\theta_n - \cos\theta_{n+1} - \cos\theta_{n-1}\right],\end{aligned} \tag{3.1}$$

where we have introduced the following normalized variables and parameters: the longitudinal displacement of unit n, $U_n = u_n/a$, the normalized time $T = t\sqrt{k_l/m}$, an inertial parameter $\alpha = a\sqrt{m/(4J)}$, and stiffness parameters $K_\theta = 4k_\theta/(k_l a^2)$ and $K_s = k_s/k_l$. Above, m and J are the mass and the moment of inertia of the rigid units, while a is the unit cell length (distance between the centers of the masses).

3.2.2. Discrete dispersion relations

A particularity of this system, compared to other mechanical chains with two DOFs, [104, 105, 36, 10, 37], is that in the linear limit, the two motions (displacements and rotations) are decoupled, i.e. each degree of freedom follows its dynamics, independent of the other (see appendix A).

The corresponding dispersion relations are given by

$$\omega^{(1)} = 2\sin\left(\frac{qa}{2}\right), \tag{3.2}$$

$$\omega^{(2)} = \pm\sqrt{4\alpha^2(K_s - K_\theta)\sin^2\left(\frac{qa}{2}\right) + 6\alpha^2 K_\theta}\,. \tag{3.3}$$

The first branch, Eq. (3.2), describes propagating longitudinal waves with the typical monoatomic dispersion relation. The second branch, Eq. (3.3), describes propagating rotational waves with a Klein-Gordon type dispersion relation and a lower cutoff frequency at $\omega = \alpha\sqrt{6K_\theta}$. From Eq. (3.3), it is clear that the dispersion relation of the structure can be highly tuned through the inertial parameter α (changing the mass and the shape of the rigid particles) as well as the stiffness parameters K_s, K_θ (changing the elastic parameters of the plastic films). Four examples of the dispersion relation for different values of the bending stiffness K_θ are shown in Fig. 3.2 with solid lines. The rest of the parameters are chosen to be consistent with the literature [39, 7, 8, 50]. Note also that the concavity of the dispersion relation for the rotation DOF is defined by the sign of $\delta = K_s - K_\theta$, see Fig. 3.2(a-c) vs (b-d). As we explain below, the sign of δ plays a key role in the stability of the plane waves in the system.

3.2.3. Continuum limit

Considering waves with wavelengths that are sufficiently larger than the unit cell distance, i.e. $\lambda \gg a$, one can employ the continuum limit approximation. Therefore, we define two continuous functions $U(X,T)$ and $\theta(X,T)$, interpolating the displacement and rotation of the n-th pair of rigid units located at the position $x_n = na$, where n is an integer, such that

$$U(X_n,T) = U_n(T)\,, \quad \theta(X_n,T) = \theta_n(T)\,, \quad X_n = \frac{x_n}{a}\,. \tag{3.4}$$

If we further assume weak nonlinearity, namely $\theta \ll 1$, keeping terms up to θ^3, see also [7, 39], Eqs. (3.1) yield,

$$\frac{\partial^2 U}{\partial T^2} = \frac{\partial^2 U}{\partial X^2} + \theta\frac{\partial \theta}{\partial X}\,, \tag{3.5}$$

$$\frac{\partial^2 \theta}{\partial T^2} = C_1\frac{\partial^2 \theta}{\partial X^2} - C_2\theta - C_3\theta^3 - C_4\theta\frac{\partial U}{\partial X}\,, \tag{3.6}$$

where $C_1 = \alpha^2[K_s - K_\theta]$, $C_2 = 6K_\theta\alpha^2$, $C_3 = 2\alpha^2$ and $C_4 = 4\alpha^2$. The system of equations (3.5-3.6) is a simple dispersion-less wave equation for the displacement field U, Eq. (3.5), coupled through a nonlinear term, with a nonlinear Klein-Gordon equation for the rotation field θ, Eq. (3.6). Pulse soliton solutions of (3.5-3.6) were theoretically obtained and experimentally observed in [7], revealing the validity of the continuum-coupled equations.

The linear dispersion relations of Eqs. (3.5-3.6) are given by,

$$\omega^{(1)} = k\,, \tag{3.7}$$

$$\omega^{(2)} = \sqrt{C_1 k^2 + C_2}\,, \tag{3.8}$$

and they are shown in Fig. 3.2 with dashed lines. For the cases we plot, one can see that as long as the wavenumber $qa \leq 1$, the continuum equations capture well the dispersive characteristics of the discrete model.

3.3. Modulated waves in FlexMM

Although there are several recent studies on pulse nonlinear waves, the existence, stability, and propagation of nonlinear modulated waves, in the form of plane waves or wavepackets in FlexMM remain unexplored. Only recently, the existence and stability of discrete breathers in FlexMM were explored [106]. Here, we derive the theoretical framework for

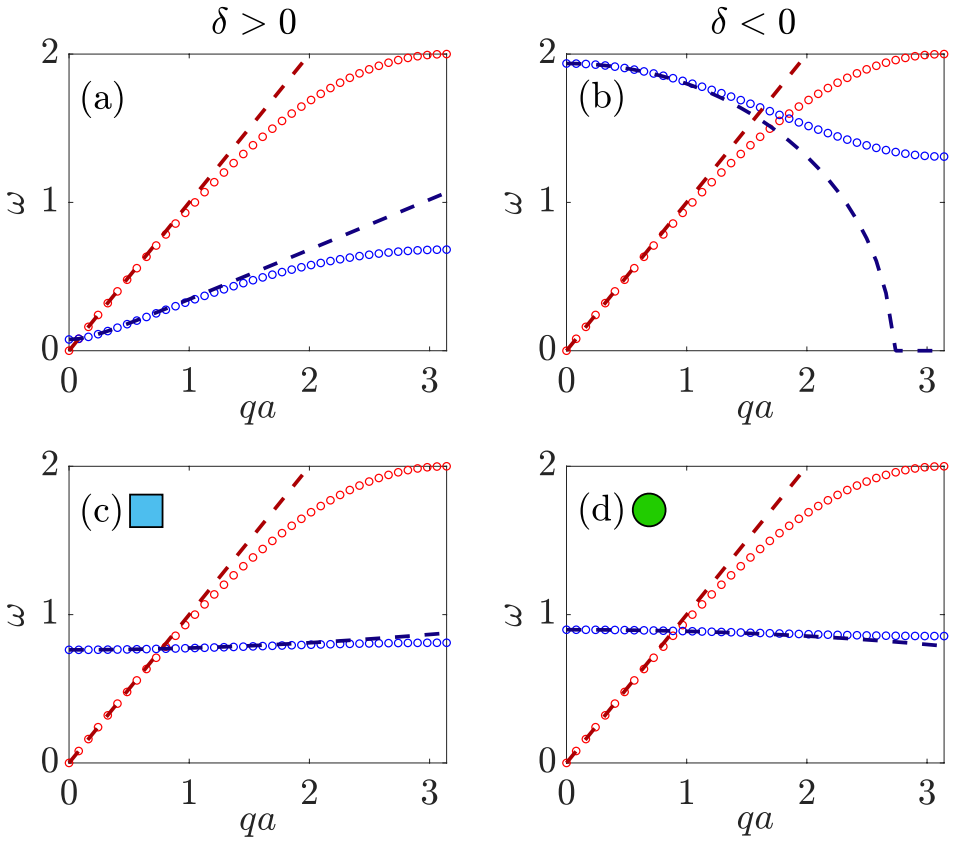

Figure 3.2: Dispersion relations of Eqs. (3.2-3.3) (solid lines) and of the continuum approximation (dashed lines) following Eqs. (3.7-3.8). In all the examples, we fix the coefficients $\alpha = 2.5$, $K_s = 0.01851$ and we vary K_θ. (a) $K_\theta = 1.534.10^{-4}$, (b) $K_\theta = 0.1$, (c) $K_\theta = 0.01551$, and (d) $K_\theta = 0.02151$. Left (right) panels correspond to $\delta > 0$ ($\delta < 0$).

the description of long-wave, nonlinear modulated waves. For this purpose, we apply below the multiple-scales method [71, 70] to Eqs. (3.5-3.6).

3.3.1. Multiple-Scales

We are looking for U and θ, in the form of a perturbative expansion,

$$\begin{aligned} U &= \sum_{i=1}^{N} \epsilon^i u_i(X_0, \dots X_N, T_0, \dots T_N)\,, \\ \theta &= \sum_{i=1}^{N} \epsilon^i \theta_i(X_0, \dots X_N, T_0, \dots T_N)\,, \end{aligned} \tag{3.9}$$

where $T_i = \epsilon^i T$ and $X_i = \epsilon^i X$, with $i = 0, 1, \dots N$ and ϵ represents a small parameter. X_0 and T_0 correspond to the original "fast" spatial and temporal scales of the carrier wave,

while X_i and T_i with $i \neq 0$ define progressively the "slow" spatial and temporal scales of the envelope.

By inserting the expansions of Eq. (3.9) into the system of Eqs. (3.5-3.6), and taking into account the derivative operators of the new spatial and temporal variables (see appendix B Eq. (B.1)), we end up with the following hierarchy of equations at successive orders of ϵ,

$$
\begin{aligned}
&\mathcal{O}(\epsilon) \\
&\begin{cases}
\hat{\mathcal{L}}_0^{(1)} u_1 = 0\,, \\
\hat{\mathcal{L}}_0^{(2)} \theta_1 = 0\,,
\end{cases} \\
&\mathcal{O}(\epsilon^2) \\
&\begin{cases}
\hat{\mathcal{L}}_0^{(1)} u_2 = -\hat{\mathcal{L}}_1^{(1)} u_1 + \hat{\mathcal{M}}_0^{(1)} \theta_1^2\,, \\
\hat{\mathcal{L}}_0^{(2)} \theta_2 = -\hat{\mathcal{L}}_1^{(2)} \theta_1 + \theta_1 \hat{\mathcal{M}}_0^{(2)} u_1\,,
\end{cases} \\
&\mathcal{O}(\epsilon^3) \\
&\begin{cases}
\hat{\mathcal{L}}_0^{(1)} u_3 = -\hat{\mathcal{L}}_1^{(1)} u_2 - \hat{\mathcal{L}}_2^{(1)} u_1 + \hat{\mathcal{M}}_1^{(1)} \theta_1^2 + 2\hat{\mathcal{M}}_0^{(1)} \theta_1 \theta_2\,, \\
\hat{\mathcal{L}}_0^{(2)} \theta_3 = -\hat{\mathcal{L}}_1^{(2)} \theta_2 - \hat{\mathcal{L}}_2^{(2)} \theta_1 + \hat{\mathcal{M}}^{(3)} \theta_1^3 + \theta_1 \hat{\mathcal{M}}_0^{(2)} u_2 + \theta_1 \hat{\mathcal{M}}_1^{(2)} u_1 + \theta_2 \hat{\mathcal{M}}_0^{(2)} u_1\,,
\end{cases}
\end{aligned}
\tag{3.10}
$$

where the linear operators, $\hat{\mathcal{L}}_j^{(i)}$ and $\hat{\mathcal{M}}_j^{(i)}$, applied to the linear and nonlinear terms of the equations (3.5-3.6) respectively are defined in appendix B Eqs. (B.2).

The first set of equations (3.10) of order $\mathcal{O}(\epsilon)$, corresponds to the linearized system of Eqs.(3.5-3.6). Using the fact that in the linear regime, the two fields are decoupled, we will focus on the particular case in which, at the leading order, there is only rotational motion, i.e.,

$$
\begin{aligned}
u_1 &= 0\,, \\
\theta_1 &= B(X_1, T_1, X_2, T_2, ...) e^{i(kX_0 - \omega T_0)} + \text{c.c}\,,
\end{aligned}
\tag{3.11}
$$

with ω and k satisfying the dispersion relation Eq. (3.8) and c.c stands for the complex conjugate.

Let us proceed to the next order of the perturbation scheme, $\mathcal{O}(\epsilon^2)$, and substitute the solutions (3.11) into the second set of equations (3.10) to obtain,

$$
\begin{aligned}
\hat{\mathcal{L}}_0^{(1)} u_2 &= \hat{\mathcal{M}}_0^{(1)} \theta_1^2\,, \\
\hat{\mathcal{L}}_0^{(2)} \theta_2 &= -\hat{\mathcal{L}}_1^{(2)} \theta_1\,.
\end{aligned}
\tag{3.12}
$$

The right-hand-side of the last equation is a secular term, as it acts as a source term proportional to $e^{i\sigma}$ ($\sigma = kX_0 - \omega T_0$) with which the linear operator $\hat{\mathcal{L}}_0^{(2)}$ on the left is in resonance. This implies that the solution θ_2 would blow up as $t \to \infty$ and thus the perturbation scheme will fail. The only way for the expansion to be bounded is to set the secular term to zero, which translates to the following relation for the envelope function B,

$$D_1 B + v_g D_{1X} B = 0\,. \tag{3.13}$$

Here we have introduced the group velocity given by

$$v_g = \frac{C_1 k}{\sqrt{C_1 k^2 + C_2}} = \frac{C_1 k}{\omega}\,. \tag{3.14}$$

Once the secular term is removed, the system of equations of the second order in ϵ in Eq. (3.10) is now reduced to,

$$\begin{cases} \hat{\mathcal{L}}_0^{(1)} u_2 = ikB^2 e^{2i\sigma} + \text{c.c}\,, \\ \hat{\mathcal{L}}_0^{(2)} \theta_2 = 0\,. \end{cases} \tag{3.15}$$

The first equation has the following solution,

$$u_2 = \frac{ikB^2}{4(k^2 - \omega^2)} e^{2i\sigma} + \text{c.c}\,, \tag{3.16}$$

where the homogeneous part of the solutions is omitted due to our choice of initial conditions $U(0, X) = \dot{U}(0, X) = 0$. For θ_2 we choose the trivial solution, i.e. $\theta_2 = 0$, since any other solution can be incorporated in B.

3.3.2. Nonlinear Schrödinger equation (NLSE)

We now proceed with the $\mathcal{O}(\epsilon^3)$ order of the perturbation scheme. By using $u_1 = 0$ and $\theta_2 = 0$, as discussed above, the last equation of Eq. (3.10) is reduced to

$$\hat{\mathcal{L}}_0^{(2)} \theta_3 = -\hat{\mathcal{L}}_2^{(2)} \theta_1 + \hat{\mathcal{M}}^{(3)} \theta_1^3 + \theta_1 \hat{\mathcal{M}}_0^{(2)} u_2\,. \tag{3.17}$$

Similar to the previous order, there are secular terms on the right-hand side of Eq. (3.17) proportional to $e^{i\sigma}$: the $\hat{\mathcal{L}}_2^{(2)} \theta_1$, and parts of the $\hat{\mathcal{M}}^{(3)} \theta_1^3$ and $\theta_1 \hat{\mathcal{M}}_0^{(2)} u_2$ terms. To find their secular contributions, we develop the operators as well as the functions on which they are

applied. For the first of them,

$$\hat{\mathcal{M}}^{(3)}\theta_1^3 = -C_3B^3e^{3i\sigma} - 3C_3|B|^2Be^{i\sigma} + \text{c.c}\,, \tag{3.18}$$

the secular contribution is $-3C_3|B|^2Be^{i\sigma}$. For the next one,

$$\theta_1\hat{\mathcal{M}}_0^{(2)}u_2 = \frac{C_4k^2B^3}{2(k^2-\omega^2)}e^{3i\sigma} + \frac{C_4k^2|B|^2B}{2(k^2-\omega^2)}e^{i\sigma} + \text{c.c}\,, \tag{3.19}$$

the secular contribution is $\frac{C_4k^2|B|^2B}{2(k^2-\omega^2)}e^{i\sigma}$. To avoid resonant driving we set all the secular terms equal to zero (3.17-3.18-3.19),

$$\hat{\mathcal{L}}_2^{(2)}\theta_1 + \left(3C_3 - \frac{C_4k^2}{2\left(k^2-\omega^2\right)}\right)|B|^2Be^{i\sigma} = 0\,. \tag{3.20}$$

It is possible to simplify this expression Eq. (3.20) by using the variables $\xi_i = X_i - v_gT_i$, $\tau_i = T_i$, i.e. a reference frame moving with the group velocity. Within this frame Eq. (3.13), becomes $\partial B/\partial\tau_1 = 0$ and Eq. (3.20) leads to the following nonlinear Schrödinger equation,

$$i\frac{\partial B}{\partial\tau_2} + \frac{g_1}{2}\frac{\partial^2B}{\partial\xi_1^2} + g_2|B|^2B = 0\,. \tag{3.21}$$

Eq. (3.21) describes the evolution of envelope B of the modulated rotational waves, in the co-moving space variable and the second-order slow time.

The coefficients g_1 and g_2 are given by the following expressions,

$$\begin{aligned} g_1 &= \frac{C_1 - v_g^2}{\sqrt{C_1k^2 + C_2}}\,, \\ g_2 &= -\frac{1}{2\sqrt{C_1k^2 + C_2}}\left(3C_3 + \frac{C_4k^2}{2k^2(C_1-1) + 2C_2}\right)\,. \end{aligned} \tag{3.22}$$

Furthermore, Eq. (3.21) can be rewritten as a function of a single nonlinear parameter $g = g_2/g_1$ by applying the following change of variable $\tilde{\tau}_2 = g_1\tau_2$,

$$i\frac{\partial B}{\partial\tilde{\tau}_2} + \frac{1}{2}\frac{\partial^2B}{\partial\xi_1^2} + g|B|^2B = 0\,. \tag{3.23}$$

In its current form, the NLS equation has two distinct behaviors depending on the sign of the nonlinearity coefficient: it is known as focusing when $g > 0$ and defocusing for $g < 0$. Among other different properties between these two cases, an important one is the stability of plane wave solutions. More precisely, for the focusing case, it is known that plane waves

are subject to modulational instabilities [84, 107, 108, 109, 110, 91, 92], which is the main interest of the present work. Therefore, below we establish the conditions under which MI appears in the proposed FlexMM.

3.3.3. Modulation instability (MI)

We seek solutions of Eq. (3.23) in the form of a perturbed plane wave [82],

$$B(\xi_1, \tilde{\tau}_2) = (A_0 + b(\xi_1, \tilde{\tau}_2))e^{i(k_0\xi_1 - \omega_0\tilde{\tau}_2 + \tilde{\theta}(\xi_1,\tilde{\tau}_2))}\,, \tag{3.24}$$

with b the amplitude and $\tilde{\theta}$ the phase of small perturbations. The unperturbed plane wave satisfies the dispersion relation,

$$\omega_0 = \frac{k_0^2}{2} - gA_0^2. \tag{3.25}$$

Inserting Eq. (3.24) into Eq. (3.23), we find at first order a set of linear equations for the perturbations b and $\tilde{\theta}$. We thus assume harmonic solutions of the form,

$$b = f_1 e^{i(K\xi_1 - \Omega\tilde{\tau}_2)}\,, \quad \tilde{\theta} = f_2 e^{i(K\xi_1 - \Omega\tilde{\tau}_2)}\,, \tag{3.26}$$

where the perturbation frequency Ω and wavenumber K follow the dispersion relation,

$$\Omega = Kk_0 \pm |K|\sqrt{\frac{K^2}{4} - gA_0^2}\,. \tag{3.27}$$

We can now identify two different regions of stability of the plane waves. On the one hand, where $g < 0$ the perturbations are oscillating functions and remain bounded. Thus we call this region *modulational stable*. On the other hand, for $g > 0$ there exists a band of unstable wavenumbers satisfying $K < K_c$ where,

$$|K_c| = 2A_0\sqrt{g}\,, \tag{3.28}$$

resulting in a complex frequency $\Omega = \Omega_R \pm i\Omega_I$ with

$$\Omega_R = Kk_0, \quad \Omega_I = |K|A_0\sqrt{g - \frac{K^2}{4A_0^2}}\,. \tag{3.29}$$

We call this region modulational *unstable*. The small unstable wavenumbers lead to an exponential growth of the perturbations, with a growth rate Ω_I. Thus any perturbation

with wavenumbers within the instability band should lead to MI. Another important parameter for studying MI is the wavenumber with the maximum growth rate,

$$|K_m| = A_0\sqrt{2g}\,. \tag{3.30}$$

We notice that both the critical wavenumber K_c and the wavenumber corresponding to the fastest growth rate of the perturbations K_m, depend on the parameter g and the initial amplitude A_0.

Parametric study of the coefficient g

It is now clear that the stability of modulated waves in the FlexMM depends on the sign g. As already discussed in section 3.2, we study two distinct cases: (I) allowing only rotations and (II) with 2 DOFs per unit, i.e. including both rotation and longitudinal displacement [Fig. 3.1(b-c)]. The corresponding nonlinear coefficient $g(\delta, \alpha, K_\theta, k)$ for the two cases is given by,

$$g = \frac{-3\alpha^2}{\delta\alpha^2 - v_g^2}\,, \tag{3.31}$$

for case (I), and

$$g = \frac{-3\alpha^2}{\delta\alpha^2 - v_g^2}\left(1 + \frac{k^2}{3k^2\left(\alpha^2\delta - 1\right) + 18K_\theta\alpha^2}\right)\,, \tag{3.32}$$

for case (II).

In practice, the sign of g is determined by the choice of the carrier wavenumber k and the geometrical characteristics of the FlexMM. This shows the great flexibility that the proposed system offers to manipulate weakly nonlinear waves. In Fig. 3.3 we plot a map of the sign of g as a function of the wavenumber k and δ. In all cases, white (resp. black) regions correspond to $g > 0$ (resp. $g < 0$). From the left panel, it is clear that for case (I) with only rotations, the sign of g solely depends on the sign of delta. However for case (II), things are different and the coupling between the rotation and the longitudinal motion creates intermediate regions of focusing and defocusing behavior depending also on the wavenumber k. The different panels of Fig. 3.3 also show how these regions "move" towards larger k by changing the value of the inertia parameter α.

Another interpretation of the results plotted in Fig. 3.3 is that the coupling between the rotations and longitudinal displacements creates stripes of stability (black shaded regions) in the otherwise unstable single DOF lattice with only rotations [panel (a)]. At the same time, this coupling forms regions of instability (white) where solely rotational motion would have been stable. Once again, this result shows the great tunability and richness

of the system regarding nonlinear wave propagation.

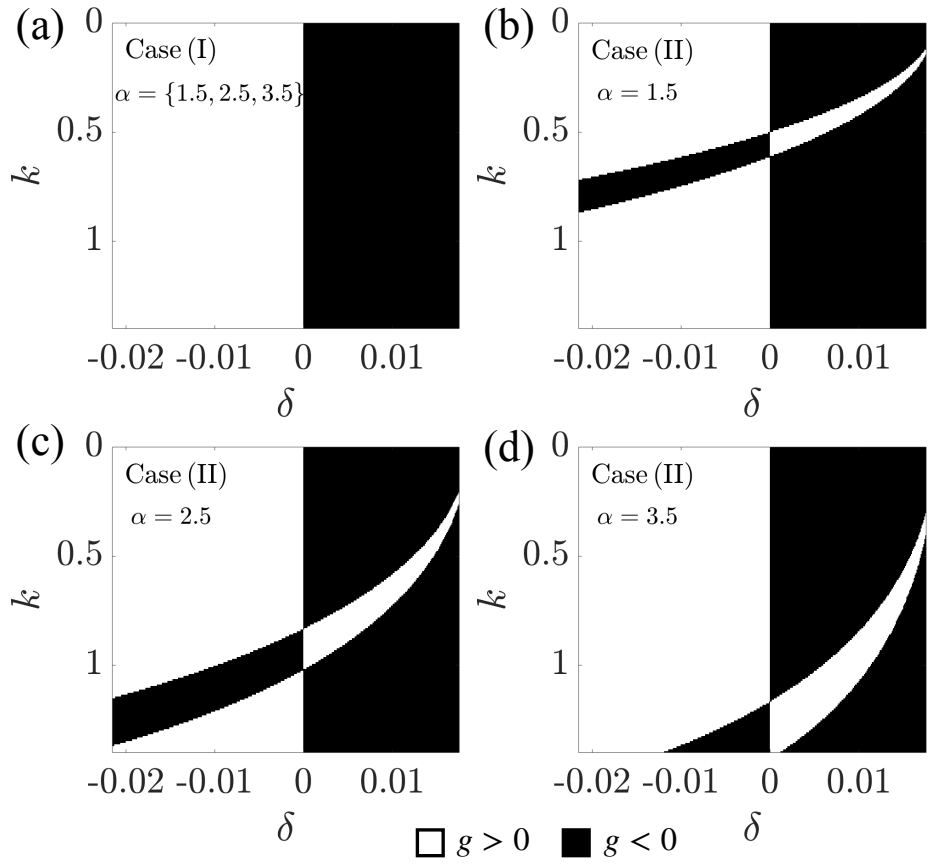

Figure 3.3: Sign of the nonlinear coefficient g as a function of k and δ, for $\alpha = 1.5, 2.5, 3.5$. Panel (a) corresponds to case (I) while panels (b,c,d) to case (II).

3.4. Numerical simulations of the FlexMM

In this section, we use direct numerical simulations of the system's discrete equations (3.1), in order to verify our analytical predictions. In particular, we first want to check the stability of plane waves as this is predicted by the sign of g (defocusing vs focusing) of the effective NLS. In addition, in the case of modulational instability, we want to compare the unstable generated wavenumber, according to the ones that the MI analysis predicts. Furthermore, we use the numerical simulations to uncover as well the dynamics of the system long after the emergence of the MI. We thus solve the Eqs. (3.1) using a $4th$ order Runge-Kutta iterative integration scheme for a total of $N = 500$ sites, using periodic boundary conditions. We focus on the case with $\alpha = 2.5$ (Fig. 3.3 panels (a) and (c)) although any other choice of α could have been done in principle.

As initial conditions, we apply *plane waves* on the rotations only, with wave-number k, whose amplitude is perturbed by a random noise

$$\begin{aligned} \theta(n,0) &= 2\epsilon(1+b_0)\cos(kn)\,, \\ \dot{\theta}(n,0) &= 2\epsilon\omega(k)(1+b_0)\sin(kn)\,, \end{aligned} \tag{3.33}$$

with $\epsilon = 0.01$ and $b_0 \in [-10^{-3}, 10^{-3}]$ is a random number taken from a uniform distribution. As mentioned above, in all the cases we use $U(n,0) = \dot{U}(n,0) = 0$ for the longitudinal displacements. Here random noise was chosen as a perturbation, not only because it is relevant to realistic experimental conditions but also because it is an efficient way to excite all the wavenumbers including the unstable ones. Moreover, we can confirm in this way our analytical results by identifying the two characteristic wavenumbers K_c and K_m using Eqs.(3.28) and (3.30) during the lattice dynamics simulation.

Here we note the following technical point. Due to the periodic boundary conditions, the spectrum is wrapped between $[0;\pi]$. During the manifestation of the MI, we expect to identify at least the following wavenumbers: the carrier k, and the most unstable wavenumber K_m. However, we know that we always excite at least the third harmonics $3k$. In order for all these frequencies to be well identified, we thus choose parameters such that the $k + \epsilon K_m$ is smaller than $3k$. To do so, we use an alternative representation of Fig. 3.3, using as colormap the values of K_m. The two points denoted by squares and circles in the left and right panels respectively, are the two examples that we will study in detail below.

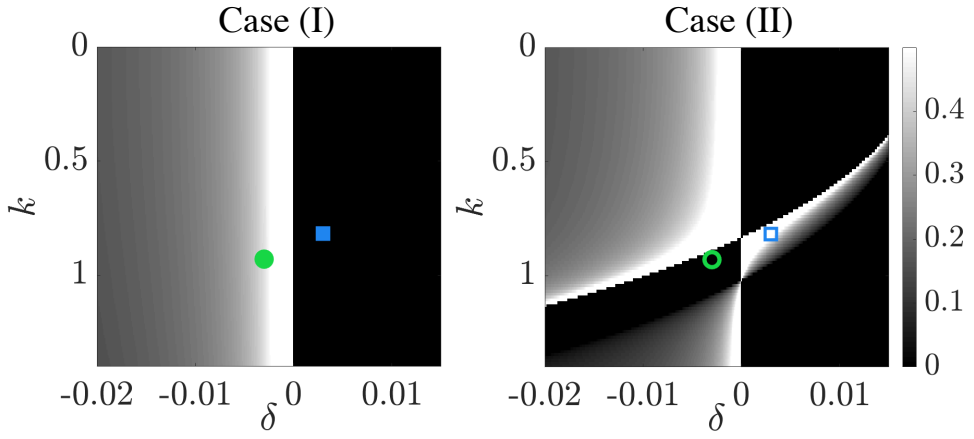

Figure 3.4: Most unstable wavenumber K_m (colormap) as a function of δ and k for $\alpha = 2.5$. In both panels, two particular points are indicated: a blue square point for $k = 0.81681$ and $\delta = 0.003$ and a green circle point at the position $k = 0.92991$ and $\delta = -0.003$.

3.4.1. Inducing MI by coupling the rotations with displacements

We first focus on a point, in the parameter space spanned by δ and k, indicated by the square in Fig. 3.4. This corresponds to the plane wave wavenumber $k = 0.81681$ and $\delta = 0.003$. We fix from now the value of $\alpha = 2.5$. As a reminder, the values of δ fix the difference between shear and bending stiffness ($\delta = K_s - K_\theta$), while the value of α is the ratio of mass to the moment of inertia of the particles.

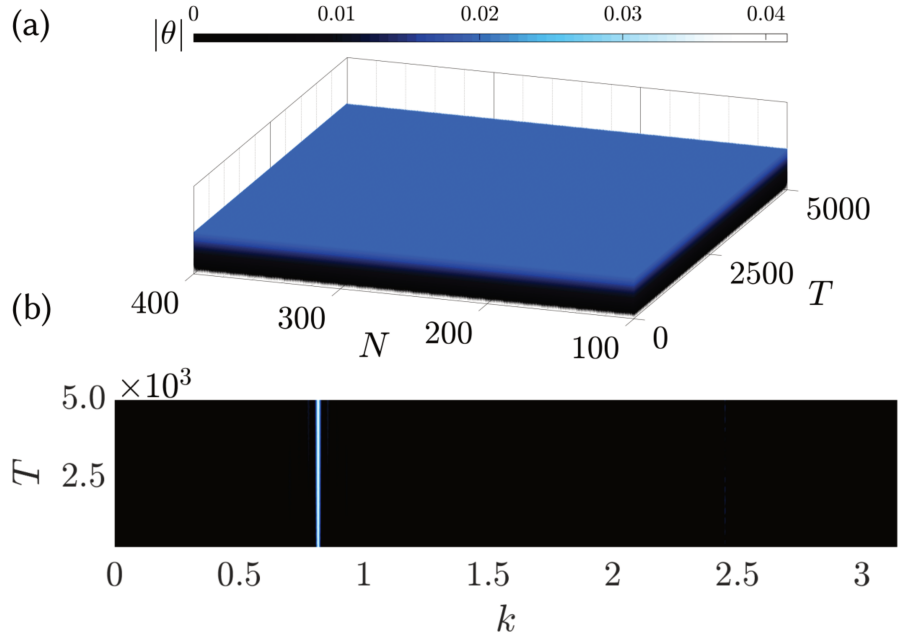

Figure 3.5: Panel (a) represents the evolution in time (T) of the absolute value of the rotation amplitude along the chain (N). Panel (b) represents the evolution in time of its k-spectrum. The results correspond to the case (I), blue square point ($k = 0.81681$, $\delta = 0.003$).

According to the theory, this point is described by a defocusing NLSE ($g < 0$) for the case (I). Thus, the plane wave is supposed to be stable. In contrast, when both the DOF are considered, i.e., case (II), and for the same parameters, the plane wave becomes modulationally unstable, since the system is described by a focusing NLSE ($g > 0$). To confirm our theoretical prediction, we solve the discrete system of Eqs. (3.1) using the initial conditions (3.33). In Fig. 3.5, we show the results for the case (I). Here both the evolution of the rotation (panel (a)) and its space Fourier transform (panel (b)) indeed show that a random perturbation on an initial plane wave remains bounded, thus the plane wave is stable.

The rotations θ_n show small amplitude oscillations in time with a frequency ω, following

the dispersion relation Eq. (3.8) at the given k. Even after more than 500 oscillations, only the wavenumber of the carrier wave is present in the spectrum, indicating stability.

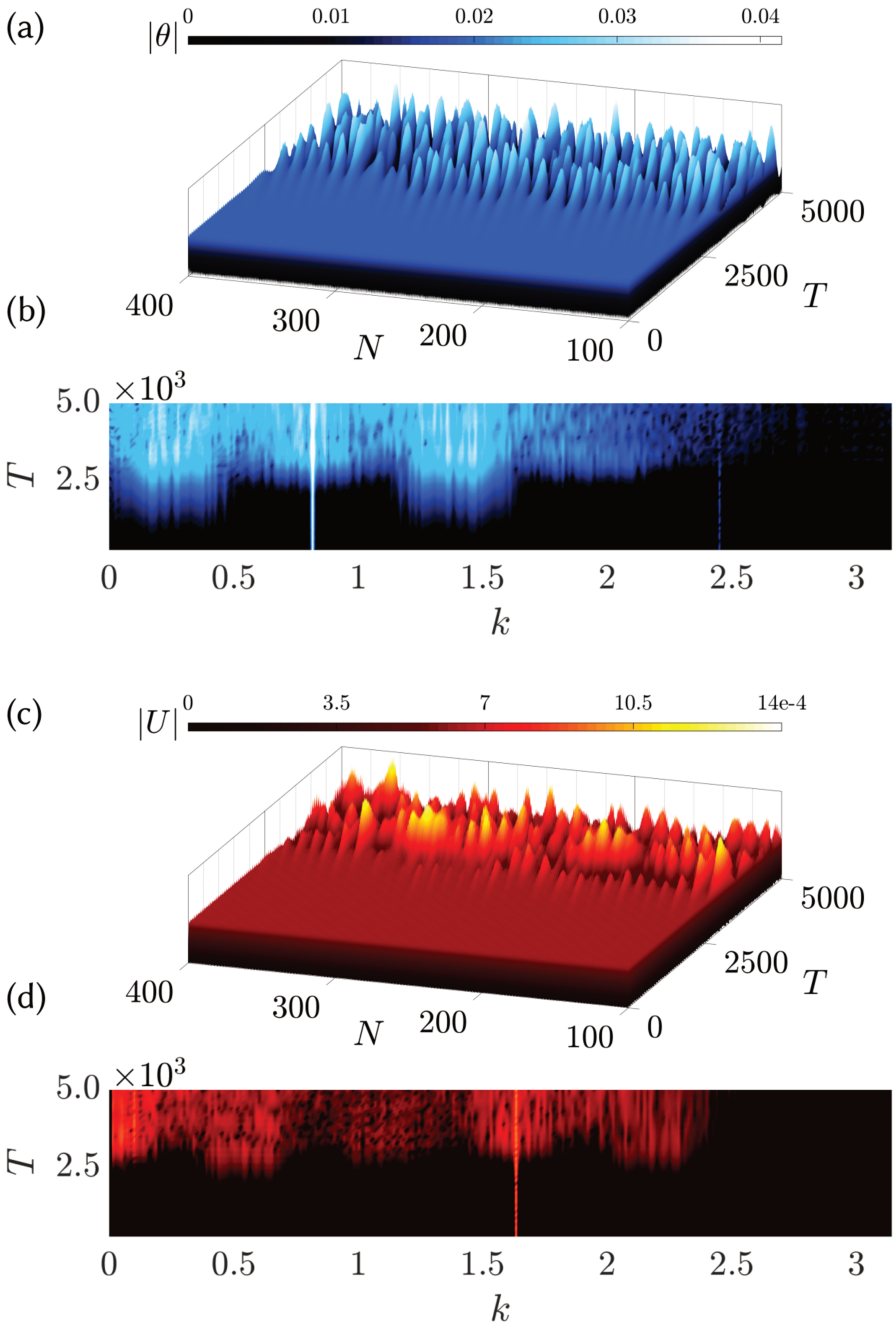

Figure 3.6: Panels (a-c) represent the evolution in time (T) of the absolute value of the rotation respectively displacement amplitudes along the chain (N). Panels (b-d) represent the evolution in time of the k-spectrum for the rotation and longitudinal displacement. The results correspond to case (II) - blue square point ($k = 0.81681$, $\delta = 0.003$).

For the exact same FlexMM and the same initial condition, if we allow the coupling between the two DOFs, namely if we consider the case (II), the dynamics are radically different. This scenario is shown in Fig. 3.6. As predicted by the theory, the wavenumbers of the perturbation that belong to the instability band, start growing. This is clear by the two sidebands that are developed symmetrically around the excited wavenumber $k = 0.81681$ in panel (b) of Fig. 3.6. More precisely, the center of these sidebands corresponds to the point $k \pm \epsilon K_m$ since the most unstable wavenumber rises first. The generation of these wavenumbers is directly revealed on the rotations as large amplitude localized structures appear (see Fig. 3.6 (a)). For later times, after the instability kicks in, and when the amplitude of the rotations becomes large enough, we observe a spectrum with many excited wavenumbers.

In this case, since rotations are coupled to the longitudinal displacements U_n, we expect to see some dynamics in the displacements too. Indeed, as expected from our analysis in Eq. (3.16), U starts oscillating with a wavenumber $2k$ as shown in Fig. 3.6(d), and at later times following the evolution of θ, larger amplitude modulated waves are also emerging in the displacements U_n.

3.4.2. Stabilizing plane waves using the coupling of DOFs

The second configuration which we focus on is the "complementary" one. It corresponds to the green circles in Fig. 3.4, where the uncoupled system (case I) is described by a focusing NLSE, thus we expect the plane waves to be modulationally unstable, while by allowing the coupling between the two DOFs (case II), the effective NLSE is focusing and thus, the plane waves are stable. To confirm these theoretical predictions, we use the same initial conditions as in Eq. (3.33) but with $k = 0.92991$ and $\delta = -0.003$ and we solve again numerically the system of Eqs. (3.1). The result of the case (I) is shown in Fig. 3.7. Following our analysis, the numerical simulations confirm that an initially perturbed plane wave develops initially the expected side branches at $k \pm \epsilon K_m$. At the final steps of the simulation, all the wavenumbers are excited. On the other hand, when both DOFs are present (case (II)) and for exactly the same parameter values, the corresponding numerical result, shown in Fig. 3.8(a-b), verifies the stability of the plane wave solution. We see that for the same total time of propagation as in the decoupled case, θ shows stable oscillations with a wavenumber k while U oscillates at $2k$, as per the theory.

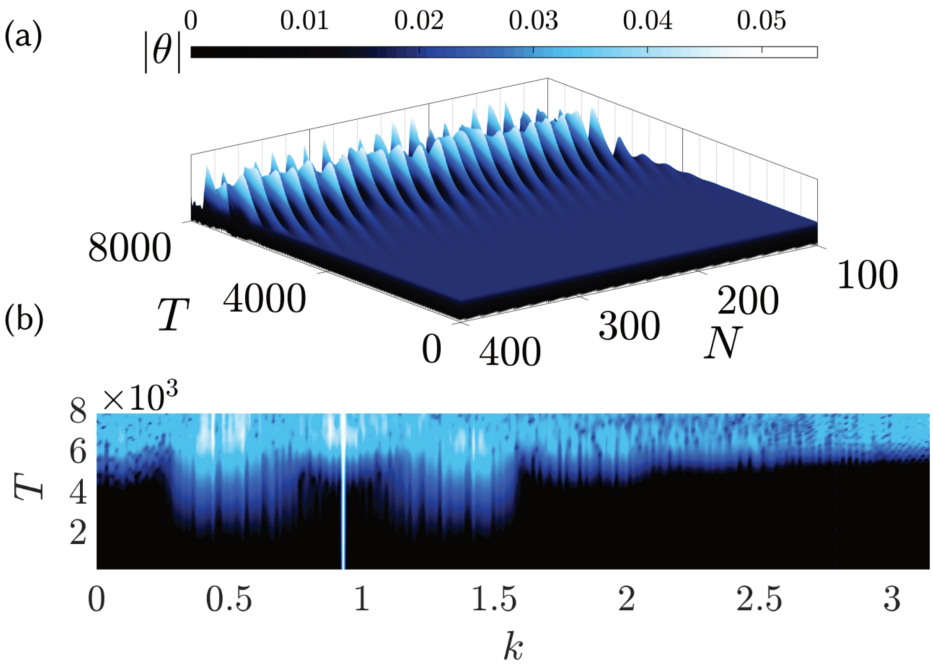

Figure 3.7: Panel (a) represents the evolution in time (T) of the absolute value of the rotation amplitude along the chain (N). Panel (b) represents the evolution in time of its k-spectrum. The result corresponds to case (I), green circle point ($k = 0.92991$, $\delta = -0.003$).

3.4.3. MI growth rate: theory vs numerics

To further support our theoretical findings we perform numerical simulations, for both cases, by varying the amplitude of the initial excitation A_0, and we compare the predictions of the MI linear stability analysis (see Eqs. (3.28-3.30)), with the early stage of the MI manifestation in simulations.

In particular, in Fig. 3.9(a-b), we plot the MI growth rate for both cases and for two different amplitudes A_0. The dotted lines correspond to the analytical values of $k + \epsilon K_m$, while the dashed ones to $k + \epsilon K_c$. In Fig. 3.9(c-d), we plot the Fourier spectrum of the rotation field θ at times that correspond to the early stage of MI. In both cases, a stronger initial excitation results in a larger unstable band showing a maximum value shifted to larger k values. Note also how well the theoretically predicted bandwidth, Fig. 3.9(a-b), matches the numerically obtained bandwidth. This observation constitutes another more quantitative validation of the derived effective NLSE description.

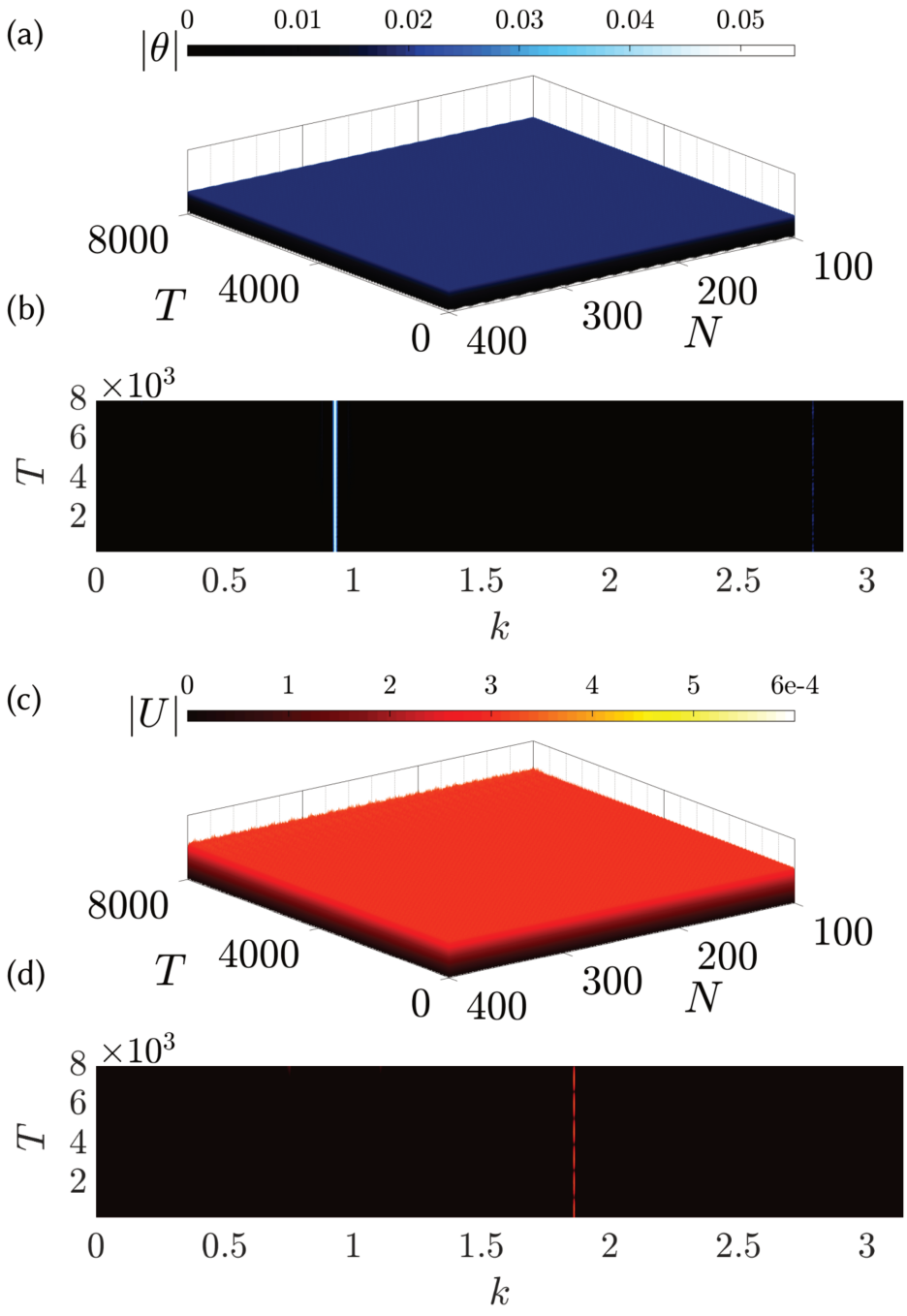

Figure 3.8: Panels (a-c) show the evolution in time (T) of the absolute value of the rotation and displacement amplitudes along the chain (N). Panels (b-d) show the evolution in time of the k-spectrum for the rotation and longitudinal displacement. The results correspond to case (II), green circle point ($k = 0.92991$, $\delta = -0.003$).

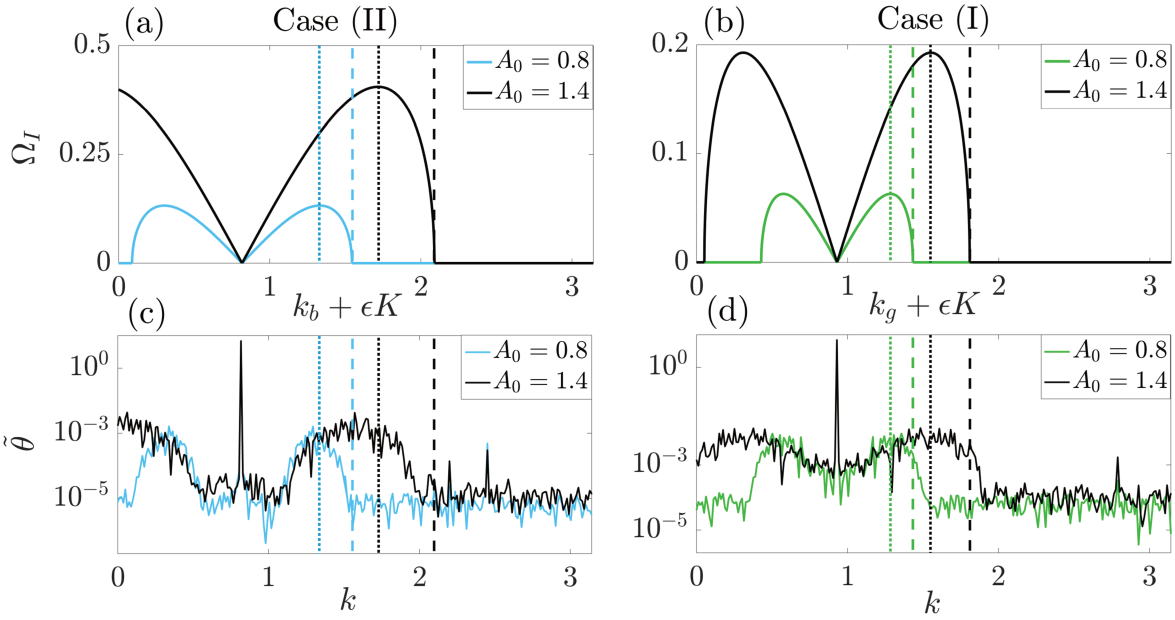

Figure 3.9: Panels (a) and (b) show the theoretical modulational instability band for the blue point in case (II), the green point in case (I) and for two different amplitudes A_0. In panels (c) and (d), we plot the Fourier transform of the θ, corresponding to the parameters of the blue square (respectively green circle) at two different instances. For case (II), we choose $t = 2500$ for $A_0 = 0.8$ and $t = 1100$ for $A_0 = 1.4$. For case (II), $t = 5000$ for $A_0 = 0.8$ and $t = 1700$ for $A_0 = 1.4$. The dotted lines correspond to the analytical values of $k_{b/g} + \epsilon K_m$, while the dashed ones to $k_{b/g} + \epsilon K_c$. $k_{b/g}$ are the wavenumbers of the initial plane waves and K the wavenumber of the perturbation.

3.5. Conclusions

In this chapter, we focused on the archetypal nonlinear phenomenon of MI. To that end, starting from a discrete, nonlinear lump model, that has been proved to accurately describe their dynamics, we first derived a NLS equation for slowly varying rotational envelope waves. We then studied the stability of the rotational plane waves to small perturbations via the MI analysis for the derived NLSE. Analytical and numerical results revealed that, under proper values of the physical parameters of the FlexMM, namely under some particular values of the inertia and stiffness parameters, it is possible to observe MI in these FlexMMs. More importantly, we have analyzed the role of the coexistence of two DOFs. In particular, the interplay between the two DOFs can lead to regions of stability, in an otherwise unstable FlexMM which supports only rotations, i.e., only one of the two DOFs, and vice versa.

4 | Bright and Dark solitons in nonlinear flexible mechanical metamaterials

By: Antoine Demiquel, Vassos Achilleos, Georgios Theocharis, Vincent Tournat. Published in Wave Motion, on August 2024. DOI:10.1016/j.wavemoti.2024.103394.

Contents

In this chapter, we employ a combination of analytical and numerical techniques to investigate the dynamics of lattice envelope vector soliton solutions propagating within a one-dimensional chain of flexible mechanical metamaterial. To model the system, we formulate discrete equations that describe the longitudinal and rotational displacements of each individual rigid unit mass using a lump element approach. By applying the multiple-scales method in the context of a semi-discrete approximation, we derive an effective nonlinear Schrödinger equation that characterizes the evolution of rotational and slowly varying envelope waves from the aforementioned discrete equations of motion. We thus show that this flexible mechanical metamaterial chain supports envelope vector solitons where the rotational component has the form of either a bright or a dark soliton. In addition, due to nonlinear coupling, the longitudinal displacement displays kink-like profiles thus forming the 2-components vector soliton. These findings, which include specific vector envelope solutions, enrich our knowledge on the nonlinear wave solutions supported by flexible mechanical metamaterials and open new possibilities for the control of nonlinear waves and vibrations.

4.1. Introduction

Nonlinear flexible mechanical metamaterials (FlexMMs) are an emerging class of engineered materials often consisting of highly deformable soft elements connected to stiffer ones [31]. They encompass a variety of designs such as origami [111, 37] and kirigami structures [6, 112], assembled mechanical parts, 3D-printed multimaterials [113, 114], and have been shown to exhibit "exotic functionalities, such as pattern and shape transformations in response to mechanical forces, or reprogrammability" [31]. Their capacity to undergo large local deformations, including local rotations, stems from the high elasticity contrasts together with their structure and naturally implies geometric non-linearity. As with other types of metamaterials, their linear properties depend on the geometry of the structure in addition to the constituent materials, so that both non-linear and linear mechanical behaviors can be tuned by modifying their structural or material parameters. Interestingly, in the context of wave control, harnessing the nonlinear properties of a metamaterial is particularly novel, since the majority of reported results have focused on controlling linear waves by managing dispersive effects.

Despite linear wave metamaterials constitute the vast majority of studied wave control strategies, a number of nonlinear wave effects have been studied and revealed in such flexible mechanical metamaterials [48], including pulse vector solitons [39, 7, 115], rarefaction solitary waves [116, 69], transition waves and topological solitons through bistable

structures for example [34, 35, 49], and more recently the manifestation of modulation instability (MI) [117].

However, to our knowledge, envelope solitons (bright and dark solitons) or breathers, have not been reported in FlexMM. Bright and dark solitons are solutions of the universal nonlinear Schrödinger equation (NLSE), and result from the complex interplay between the dispersion and nonlinearity properties of a medium [73, 71]. On the one hand bright solitons [118], are characterized by their ability to maintain a focused intensity peak during propagation. As such, these wave objects have practical applications in optical communication systems via nonlinear optical fibers, contributing to the stability and robustness of information transmission [119, 120]. On the other hand, dark solitons, which manifest themselves as stable and localized intensity drops in a wave train, have been studied in various physical contexts, including Bose-Einstein condensates in ultracold atomic gases [121], water tank experiments [52] and optics [122, 123, 124].

In terms of applications, both bright and dark solitons find utility in fields such as signal processing, optical communications, and ultrafast optics. Thus, we believe that the study of bright and dark solitons in FlexMMs will be useful in controlling large amplitude vibrations. We also expect to observe nonlinear wave phenomena in FlexMMs not yet reported in mechanics or for other wave fields. Indeed, while bright and dark solitons are mostly associated with optical systems and cold atoms, recent research has expanded their relevance to mechanical devices. For example, researchers have explored soliton-like phenomena in structures such as granular chains or phononic crystals [125, 126]. These granular solitons show potential applications in shock absorption and energy transfer mechanisms [127]. In addition, dark solitons have been studied in the context of acoustic waves with acoustic transmission lines [68], leading to the development of novel devices for sound manipulation and waveguiding [128]. The interdisciplinary study of solitons in mechanical systems reflects a growing interest and understanding of their universal properties. The applications of bright and dark solitons in mechanical devices continue to expand, paving the way for innovations in fields such as acoustics, wave engineering, and materials science.

The main objective of this chapter is to study the bright and dark soliton solutions of the NLS equation as lattice envelope vector solitons in the nonlinear FlexMM context. The chapter is structured as follows. In Sec. 4.2 we present the nonlinear discrete lump model which was found to be relevant for describing the dynamical equations of FlexMMs. In section 4.3 we derive an effective NLS equation (eNLSE) for the slowly varying envelope of waves of the rotational degree of freedom in the semi-discrete approximation using

asymptotic expansion and multiple-scale methods, from the discrete equations of motion of the system. Finally in sections 4.4 and 4.5, the existence and dynamics of bright and dark envelope vector solitons are investigated respectively.

4.2. Lumped element approach

4.2.1. Problem position and modeling of the structure

The family of FlexMM that we consider in this work consists of rigid particles (in the shape of crosses) connected to their nearest neighbors by elastic connectors and periodically arranged in a chain of two rows and N columns, see Fig. 4.1(a). This type of structure is inspired by the FlexMM studied experimentally in Ref. [7]. There, the particles are constructed with Lego® bricks and the elastic connectors are made with highly flexible plastic films.

To model this structure in the low-frequency regime, we adopt the lumped-element approach. We consider the particles as rigid, characterized by their mass m and their moment of inertia J, while the elastic connectors are modeled as three massless springs; a longitudinal spring with stiffness k_l, a shear spring with shear stiffness k_s, and a bending spring with bending stiffness k_θ. We focus on in-plane motion, so in general, each particle has three DOFs, one rotation (around the z-axis), and two displacements (one in the longitudinal direction along x and one in the transverse direction along y). We also consider only symmetric motion relative to the symmetry axis, see Fig. 4.1(b).

Similarly to Ref. [7], we consider two DOFs, a longitudinal displacement u and a rotational motion θ. This means that we constrain the particles not to move along the y-axis. Ignoring the transverse motion may also be valid even without this forced constraint. In fact, for the structure of Ref. [7] it was shown numerically and experimentally that during the soliton propagation [7, 39], ignoring the transversal displacement is a reasonable assumption since the transversal displacement amplitude was experimentally found to be an order of magnitude smaller than the longitudinal one.

The sign of the rotation angles is considered positive in the trigonometric direction. In previous works [7, 117], the angle is defined as a positive-negative alternation from one cell to the next, which is a different point of view but does not change the physics. The choice made here makes the analysis easier since we are studying modulated waves.

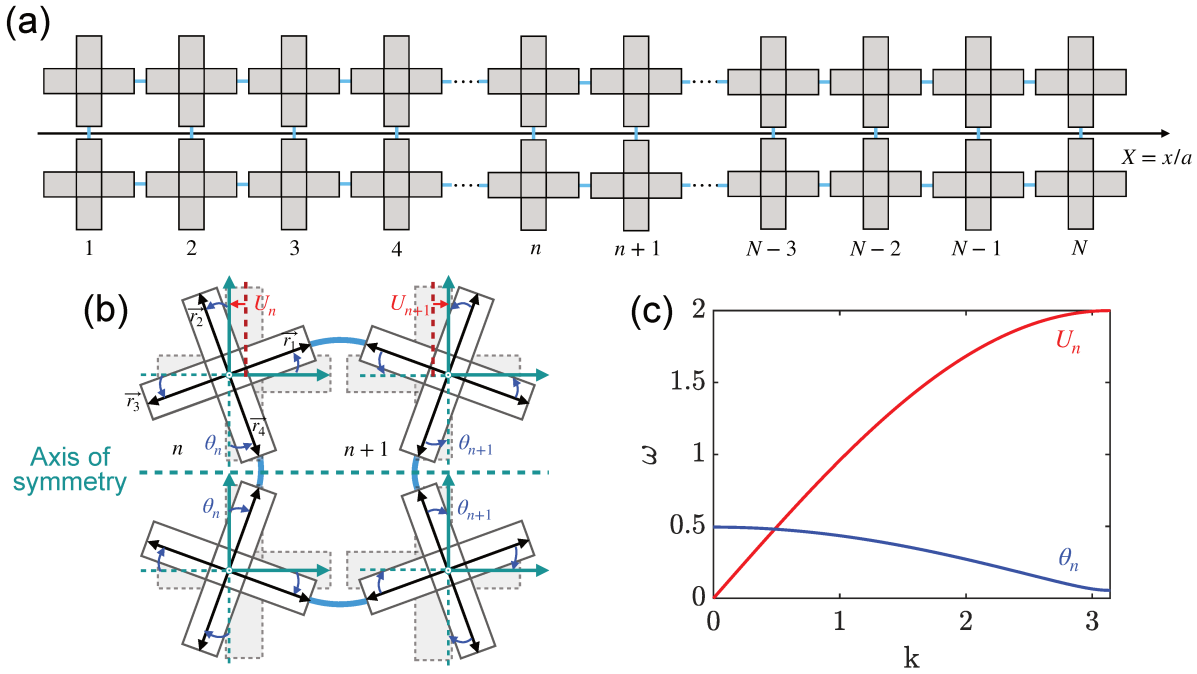

Figure 4.1: (a) Sketch of the FlexMM under consideration. The structure consists of two rows of rigid mass units (gray crosses) connected by elastic links (thick, blue lines) extending along the normalized X-direction ($X = x/a$) with a periodic arrangement. The rigid units are characterized by a mass m and a moment of inertia J using a normalization (cf. Eq. (4.8b)). The inertia of the particle can be defined by a single coefficient α. The elastic connectors are characterized by effective stiffnesses (normalized to the longitudinal spring k_l): K_s and K_θ. We consider symmetric movements relative to the horizontal axis of symmetry between the two lines. (b) Displacements of the n and $n+1$ particles from the equilibrium position, the mass units can rotate θ and longitudinally translate U. (c) Dispersion relation, cf. Eq. (4.9), of the corresponding structure using coefficients found in the literature [7, 8]: $\alpha = 1.815$, $K_s = 0.01851$ and $K_\theta = 1.534.10^{-4}$.

4.2.2. Equations of motion of the system

Based on the previous assumptions, we can establish the governing equations of a one-dimensional chain starting with perfect initial alignment, resulting in a static angle of zero. Considering a single element (a cross), the position of its extremities is,

$$\begin{aligned} \mathbf{r_1} &= \begin{pmatrix} l\cos\theta_n \\ l\sin\theta_n \end{pmatrix} \qquad \mathbf{r_2} = \begin{pmatrix} -l\sin\theta_n \\ l\cos\theta_n \end{pmatrix} \\ \mathbf{r_3} &= \begin{pmatrix} -l\cos\theta_n \\ -l\sin\theta_n \end{pmatrix} \qquad \mathbf{r_4} = \begin{pmatrix} l\sin\theta_n \\ -l\cos\theta_n \end{pmatrix} \end{aligned} . \tag{4.1}$$

Thanks to the position of the vertices, the elongations of horizontally oriented springs are given by,

$$\begin{aligned} \mathbf{\Delta l_{n,1}} &= \mathbf{y_n} + [\{\mathbf{r_3}(\theta_{n+1}) - \mathbf{r_3}(0)\} - \{\mathbf{r_1}(\theta_n) - \mathbf{r_1}(0)\}] \\ &= \begin{bmatrix} u_{n+1} - u_n - l\cos\theta_{n+1} - l\cos\theta_n + 2l \\ -l\sin\theta_{n+1} - l\sin\theta_n \end{bmatrix} , \end{aligned} \tag{4.2}$$

while the elongation of the vertically oriented springs is neglected, due to symmetry as mentioned above,

$$\mathbf{\Delta l_{n,2}} = \mathbf{0} . \tag{4.3}$$

Rotational elongation can also be expressed by,

$$\Delta\theta_{n,1} = \theta_{n+1} - \theta_n , \tag{4.4a}$$

$$\Delta\theta_{n-1,1} = \theta_n - \theta_{n-1} , \tag{4.4b}$$

$$\Delta\theta_{n,2} = 2\theta_n . \tag{4.4c}$$

Combining the expression of each hinge elongation, the expression for the potential energy of the system can be written,

$$\mathcal{U}_{n,p}(\mathbf{\Delta l_{n,p}}, \Delta\theta_{n,p}) = \frac{1}{2}\|\mathbf{k}.\mathbf{\Delta l_{n,p}}\|^2 + \frac{1}{2}k_\theta {\Delta\theta_{n,p}}^2 , \tag{4.5}$$

with, $p = \{1, 2\}$ and $\mathbf{k} = (\sqrt{k_l},\ \sqrt{k_s})$. Note that this model for the elastic potential energy assumes that the elastic bonds between vertices behave physically in the following way: the bending/rotational restoring moment just depends on the relative angles between the neighboring units, the shear restoring force is proportional to the elongation of the connector projected on the axis orthogonal to the connector axis at rest (e.g. a vertical displacement difference of the vertices for a horizontal connector), and the longitudinal restoring force is proportional to the elongation of the connector projected on the axis of the connector axis at rest. A more general model could be implemented, accounting

for global rotation effects and geometrical nonlinearity associated with large rotations, but would not necessarily lead to tractable equations of motion. These assumptions have been previously experimentally validated for soliton propagation in similar metamaterial chains [7, 115, 48].

The Hamiltonian of the total system can then be written as,

$$\mathcal{H} = 2\sum_{n=1}^{N}\left\{\frac{1}{2}m\dot{u_n}^2 + \frac{1}{2}J\dot{\theta_n}^2\right\} + 2\sum_{n=1}^{N-1}\mathcal{U}_{n,1}\left(\mathbf{\Delta l_{n,1}}, \Delta\theta_{n,1}\right) + \sum_{n=1}^{N}\mathcal{U}_{n,2}\left(\mathbf{\Delta l_{n,2}}, \Delta\theta_{n,2}\right) , \quad (4.6)$$

from which the equations of motion can be derived, assuming symmetry of the motions relative to the horizontal symmetry axis of the chain,

$$m\ddot{u}_n = -\frac{1}{2}\frac{\partial\mathcal{H}}{\partial u_n} = -\frac{\partial\mathcal{U}_{n-1,1}}{\partial u_n} - \frac{\partial\mathcal{U}_{n,1}}{\partial u_n} , \quad (4.7a)$$

$$J\ddot{\theta}_n = -\frac{1}{2}\frac{\partial\mathcal{H}}{\partial\theta_n} = -\frac{\partial\mathcal{U}_{n-1,1}}{\partial\theta_n} - \frac{\partial\mathcal{U}_{n,1}}{\partial\theta_n} - \frac{1}{2}\frac{\partial\mathcal{U}_{n,2}}{\partial\theta_n} . \quad (4.7b)$$

The corresponding normalized equations of motion for the n-th column are then written,

$$\frac{d^2U_n}{dT^2} = U_{n+1} - 2U_n + U_{n-1} - \frac{\cos\theta_{n+1} - \cos\theta_{n-1}}{2} , \quad (4.8a)$$

$$\begin{aligned}\frac{1}{\alpha^2}\frac{d^2\theta_n}{dT^2} &= K_\theta\left(\theta_{n-1} - 4\theta_n + \theta_{n+1}\right) - K_s\cos\theta_n\left[\sin\theta_{n-1} + 2\sin\theta_n + \sin\theta_{n+1}\right] \\ &\quad - \sin\theta_n\left[2(U_{n+1} - U_{n-1}) + 4 - \cos\theta_{n-1} - 2\cos\theta_n - \cos\theta_{n+1}\right] ,\end{aligned} \quad (4.8b)$$

where we have introduced the following normalized variables and parameters: the longitudinal displacement of unit n, $U_n = u_n/a$, the normalized time $T = t\sqrt{k_l/m}$, an inertial parameter $\alpha = a\sqrt{m/(4J)}$, and stiffness parameters $K_\theta = 4k_\theta/\left(k_l a^2\right)$ and $K_s = k_s/k_l$. Above, m and J are the mass and the moment of inertia of the rigid units, while a is the unit cell length (distance between the centers of the masses). If we compare this set of equations, cf. Eq. (4.8), in the one used in our previous work about modulation instability [117], the connection can be made by changing the signs of angles $\theta_{n\pm1}$.

In the linear limit, the two motions (displacements and rotations) are decoupled, i.e. each DOF follows its own dynamics, independent of the other. The corresponding dispersion

relations are given by,

$$\omega^{(1)} = 2\sin\left(\frac{k}{2}\right), \tag{4.9a}$$

$$\omega^{(2)} = \pm\sqrt{4\alpha^2(K_s - K_\theta)\cos^2\left(\frac{k}{2}\right) + 6\alpha^2 K_\theta}\,. \tag{4.9b}$$

Displayed in the figure 4.1(c), the red branch corresponds to propagating longitudinal wave: $\omega^{(1)}$, exhibiting a typical monoatomic dispersion relation, see Eq. (4.9a). The second branch, described by Eq. (4.9b), represents propagating rotational waves with an inverse Klein-Gordon type dispersion relation: $\omega^{(2)}$. Notably, this branch has an upper cutoff frequency at $\omega_c^{(2)} = \alpha\sqrt{4K_s + 2K_\theta}$.

4.3. Modulated waves in FlexMM: effective NLS equation from the semi-discrete approximation

Below we focus on weakly nonlinear solutions and consequently substitute the following expansions,

$$\cos\theta_n = 1 - \frac{\theta_n^2}{2} + \dots, \qquad \sin\theta_n = \theta_n - \frac{\theta_n^3}{6} + \dots, \tag{4.10}$$

to Eq. (4.8). By keeping terms up to cubic order we end up with the following set of equations of motion,

$$\frac{d^2U_n}{dT^2} = U_{n+1} - 2U_n + U_{n-1} - \frac{\theta_{n-1}^2 - \theta_{n+1}^2}{4}, \tag{4.11a}$$

$$\begin{aligned}\frac{d^2\theta_n}{dT^2} &= -\alpha^2\left(K_s - K_\theta\right)\left(\theta_{n-1} + 2\theta_n + \theta_{n+1}\right) - 6K_\theta\alpha^2\theta_n + \alpha^2(K_s - 1)\theta_n^3 \\ &- \alpha^2\frac{\theta_n}{2}\left(\theta_{n-1}^2 + \theta_{n+1}^2\right) + \frac{\alpha^2 K_s}{6}\left(\theta_{n-1}^3 + 2\theta_n^3 + \theta_{n+1}^3\right) + K_s\alpha^2\frac{\theta_n^2}{2}\left(\theta_{n-1} + \theta_{n+1}\right) \\ &- 2\alpha^2\theta_n(U_{n+1} - U_{n-1})\,.\end{aligned} \tag{4.11b}$$

In order to study modulated traveling waves we make use of the semi-discrete approximation [129, 130, 131], where a carrier wave, obeying the discrete dispersion relation, is modulated by a slowly varying envelope function treated in the continuum limit. In

particular, we look for solutions of the following form,

$$\begin{aligned} U_n &= \epsilon U_0 + \epsilon^2 U_2\,, \\ &= \epsilon G_{0,n}(T) + \epsilon^2 (G_{2,n}(T) e^{2i\sigma_n} + G^*_{2,n}(T) e^{-2i\sigma_n})\,, \end{aligned} \tag{4.12a}$$

$$\begin{aligned} \theta_n &= \epsilon\theta_1 \\ &= \epsilon (F_{1,n}(T) e^{i\sigma_n} + F^*_{1,n}(T) e^{-i\sigma_n})\,, \end{aligned} \tag{4.12b}$$

with $\sigma_n = kn - \omega T$. In this ansatz, $F_{1,n}$ is the modulation of the plane wave θ_n with phase σ_n. Also, due to the quadratic terms $\sim \theta^2$ in Eq. (4.11), in the ansatz for U_n we include both a dc-term $G_{0,n}$ and a term $G_{2,n}$ oscillating with a phase $2\sigma_n$. Substituting Eq. (4.12) into Eq. (4.11)(a) we arrive at the following equations collecting the dc in Eq. (4.13a) and $e^{2i\sigma n}$ terms in Eq. (4.13b) respectively,

$$\epsilon \ddot{G}_{0,n} = \epsilon \left(G_{0,n-1} - 2G_{0,n} + G_{0,n+1}\right) - \frac{\epsilon^2}{2}\left(|F_{1,n-1}|^2 - |F_{1,n+1}|^2\right)\,, \tag{4.13a}$$

$$\begin{aligned} \epsilon^2 \left(\ddot{G}_{2,n} - 4i\omega\dot{G}_{2,n} - 4\omega^2 G_{2,n}\right) &= \epsilon^2 \left(G_{2,n-1}e^{-2ik} - 2G_{2,n} + G_{2,n+1}e^{2ik}\right) \\ - \epsilon^2 \frac{F^2_{1,n-1}e^{-2ik} - F^2_{1,n+1}e^{2ik}}{4}\,. \end{aligned} \tag{4.13b}$$

Similarly, substituting Eq. (4.12) into Eq. (4.11)(b) we get the following equation collecting the $e^{i\sigma n}$ terms,

$$\begin{aligned} &\epsilon \left[\ddot{F}_{1,n} - 2i\omega\dot{F}_{1,n} - \omega^2 F_{1,n}\right] = \epsilon\alpha^2(K_\theta - K_s)\left[F_{1,n-1}e^{-ik} + 2F_{1,n} + F_{1,n+1}e^{ik}\right] \\ &- \epsilon 6\alpha^2 K_\theta F_{1,n} + \epsilon^3 3\alpha^2(K_s - 1)|F_{1,n}|^2 F_{1,n} \\ &- \epsilon^3 \frac{\alpha^2}{2}\left[2F_{1,n}\left(|F_{1,n-1}|^2 + |F_{1,n+1}|^2\right) + F^*_{1,n}(F^2_{1,n-1}e^{-2ik} + F^2_{1,n+1}e^{2ik})\right] \\ &+ \epsilon^3 \frac{K_s\alpha^2}{6}\left[3|F_{1,n-1}|^2 F_{1,n-1}e^{-ik} + 6|F_{1,n}|^2 F_{1,n} + 3|F_{1,n+1}|^2 F_{1,n+1}e^{ik}\right] \\ &+ \epsilon^3 \frac{K_s\alpha^2}{2}\left[F^2_{1,n}\left(F^*_{1,n-1}e^{ik} + F^*_{1,n+1}e^{-ik}\right) + 2|F_{1,n}|^2\left(F_{1,n-1}e^{-ik} + F_{1,n+1}e^{ik}\right)\right] \\ &- \epsilon^3 2\alpha^2 F^*_{1,n}\left(G_{2,n+1}e^{2ik} - G_{2,n-1}e^{-2ik}\right) - \epsilon^2 2\alpha^2 F_{1,n}\left(G_{0,n+1} - G_{0,n-1}\right)\,. \end{aligned} \tag{4.14}$$

We now proceed considering that the discrete functions $W_n(T) = \{F_{1,n}(T), G_{0,n}(T), G_{2,n}(T)\}$ are varying slowly in space and time. Therefore the continuum limit approximation is applied and the above discrete functions $W_n(T)$ are replaced by $W(X_1, X_2, \ldots, T_1, T_2, \ldots)$, where $X_i = \epsilon^i X$ and $T_i = \epsilon^i T$ are slow variables with $i = 1, 2, \ldots$. Note that under this

approximation the slowly varying functions are independent of the fast variables n and T. In addition $W_{n\pm1}$, is computed up to order ϵ^2 using Taylor expansion,

$$W_{n\pm1} = W \pm \epsilon\frac{\partial W}{\partial X_1} \pm \epsilon^2\frac{\partial W}{\partial X_2} + \frac{\epsilon^2}{2}\frac{\partial^2 W}{\partial X_1^2} + \mathcal{O}(\epsilon^3)\,, \tag{4.15}$$

and the time derivation as,

$$\dot{W}_n = \frac{\partial W}{\partial T} = \epsilon\frac{\partial W}{\partial T_1} + \epsilon^2\frac{\partial W}{\partial T_2} + \mathcal{O}(\epsilon^3)\,. \tag{4.16}$$

Substituting Eqs. (4.15-4.16) into the set of Eqs. (4.13-4.14) we arrive at a system of equations at successive orders in ϵ. The lowest order in Eq. (4.13a) (analogous to ϵ^3) gives us a relation between the dc-term G_0 and the envelope of the modulated plane wave F_1,

$$\left(\frac{\partial^2}{\partial T_1^2} - \frac{\partial^2}{\partial X_1^2}\right) G_0 = \frac{\partial |F_1|^2}{\partial X_1}. \tag{4.17}$$

In Eq. (4.13b) the lowest order is analogous to ϵ^2 and relates G_2 to F_1 as follows,

$$G_2 = \frac{i\sin(2k)}{8\left(\sin^2(k) - \omega^2\right)} F_1^2. \tag{4.18}$$

We now move to Eq. (4.14) where at order ϵ^1, we recover the dispersion relation,

$$\omega^2 = 4\alpha^2(K_s - K_\theta)\cos^2\left(\frac{k}{2}\right) + 6\alpha^2 K_\theta\,, \tag{4.19}$$

which corresponds to the branch of the rotational waves of the discrete model, cf. Eq. (4.9b). At order ϵ^2 we obtain the solvability condition,

$$\frac{\partial F_1}{\partial T_1} + v_g\frac{\partial F_1}{\partial X_1} = 0\,, \tag{4.20}$$

where

$$v_g = -\frac{\alpha^2(K_s - K_\theta)\sin(k)}{\omega}\,, \tag{4.21}$$

is the group velocity corresponding to Eq. (4.19). Up to this order F_1 is linear and not coupled to G_0, G_2. At the order ϵ^3 we have the contribution from all fields and nonlinearity, leading to the following nonlinear Schrödinger equation,

$$i\frac{\partial F_1}{\partial \tau_2} + P\frac{\partial^2 F_1}{\partial \xi_1^2} + Q|F_1|^2 F_1 = 0\,, \tag{4.22}$$

in terms of the slow variables $\xi_1 = \epsilon(X - v_g T)$ and $\tau_2 = \epsilon^2 T$. P and Q, are the dispersion and nonlinear coefficients respectively given by the following expressions,

$$P = \frac{\alpha^2(K_\theta - K_s)\cos(k) - v_g^2}{2\omega}, \tag{4.23a}$$

$$Q = \frac{1}{2\omega}\left[8K_s\alpha^2\cos^2\left(\frac{k}{2}\right) - \alpha^2(5+\cos(2k)) + \frac{\alpha^2\sin^2(2k)}{2\left(\sin^2(k)-\omega^2\right)} - \frac{4\alpha^2}{v_g^2-1}\right]. \tag{4.23b}$$

We note that the last two terms in Eq. (4.23b) arise due to the presence of G_0 and G_2 at order ϵ^3 (in the case that we consider only rotation DOF these terms are absent), and have an important effect on the resulting eNLSE properties.

The NLS equation exhibits two distinct behaviors depending on the sign of the product PQ. When $PQ > 0$, it is known as focusing featuring modulational instability and bright soliton solutions among others, while for $PQ < 0$, it is referred to as defocusing with stable plane waves and dark solitons [73]. For our system, the sign of PQ is determined by the choice of the carrier wavenumber k and the design characteristics of the flexible metamaterial (FlexMM) through the parameters α, K_s, K_θ [117].

In figure 4.2, we show the sign of PQ as a function of the wavenumber k for the fixed inertial parameter $\alpha = 1.815$ which corresponds to the experimental setup Ref.[48]. In addition, we choose two different cases of bending stiffness, with very small values $K_\theta = 1.534e^{-2}$ for panels (a-c) and $K_\theta = 1.534e^{-4}$, typically found in flexible elastic metamaterials. To highlight the effect of coupling between the 2DOFs (rotation and longitudinal displacement) on the nature of the NLSE, in panels (a-b) we plot the sign of the PQ product when only rotational DOF are considered, while in panels (c-d) when both DOFs are considered. Interestingly, by comparing panels (a-b) to (c-d), we observe that the coupling between the two DOFs dramatically changes the nature of the NLSE. We also observe that the variation of K_s stiffness has a stronger impact in the case of 2DOFs, panels (c-d). In conclusion, the nature of the eNLSE crucially depends on the design characteristics of the FlexMM and the presence of 2DOFs (U_n and θ_n). See appendix C for more details.

For the rest of the chapter, we will focus on two particular designs of FlexMM corresponding to the green and red lines, cf. Fig. 4.2, respectively called FlexMM 1 and FlexMM 2. In Fig. 4.3, we show the sign of PQ (as given by Eq. (4.23)) together with the dispersion relation Eq. (4.9) corresponding to the two FlexMM configurations mentioned above.

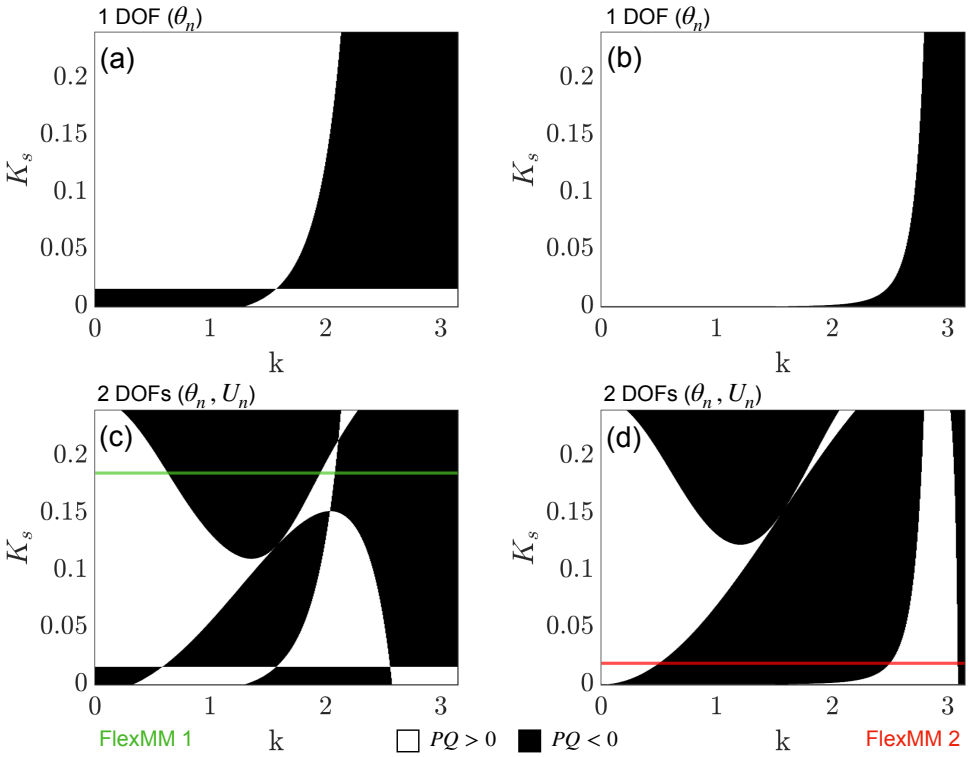

Figure 4.2: Sign of PQ as a function of k and K_s for two different $K_\theta = [1.534e{-}2, 1.534e{-}4]$ respectively used in panels (a-c) and (b-d), with $\alpha = 1.815$ fixed. Panels (a-b) correspond to a configuration where particles can only rotate, while in panels (c-d) the particles can rotate and translate. The horizontal colored lines represent the parameters chosen in Secs. 4.4-4.5 to study bright and dark solitons propagation along FlexMMs.

4.4. Bright envelope vector solitons

4.4.1. Theoretical prediction

The focusing nonlinear Schrödinger equation, Eq. (4.22) with $PQ > 0$, admits the following bright soliton solution [53],

$$F_1(\xi_1, \tau_2) = A_0 \text{sech}\left[\frac{1}{L_e}(\xi_1 - c\tau_2)\right] e^{ic\xi_1 + iQ\left(\frac{A_0^2 - c^2}{2}\right)\tau_2}, \tag{4.24}$$

where

$$Le = \frac{1}{A_0}\sqrt{\frac{2P}{Q}}, \tag{4.25}$$

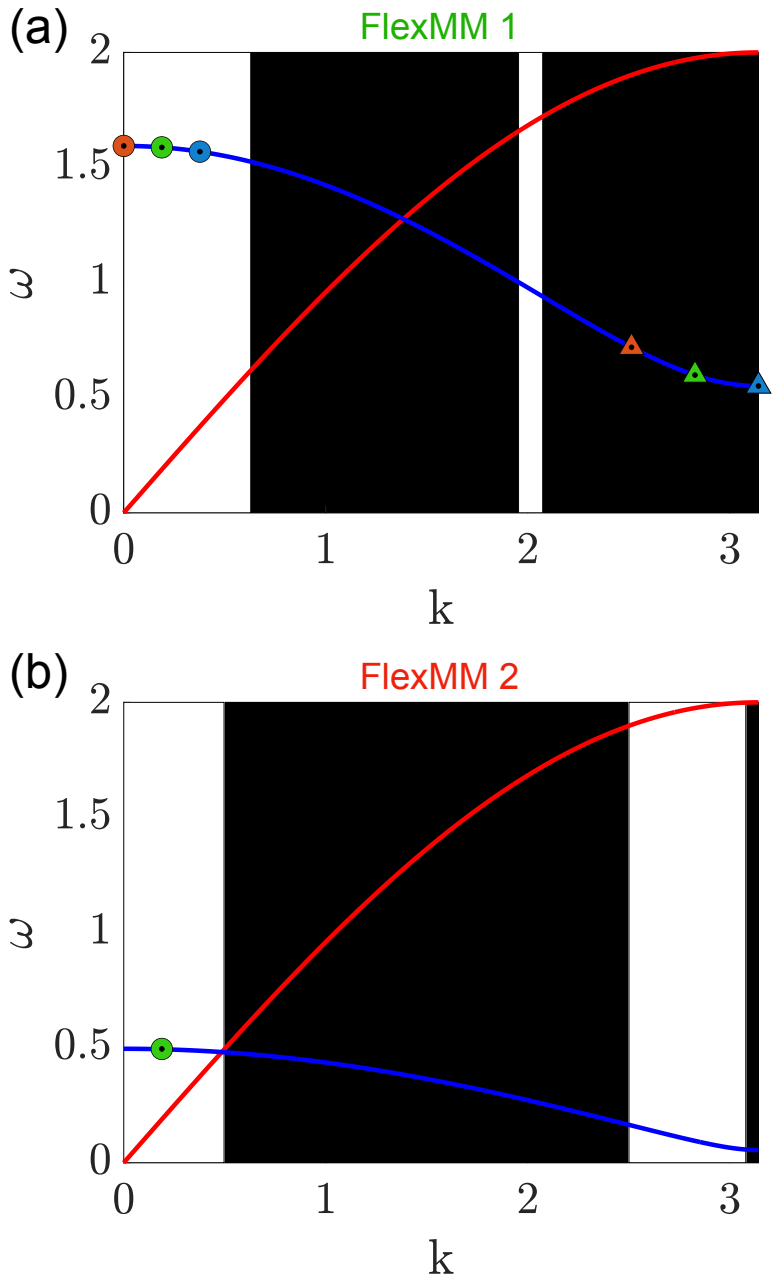

Figure 4.3: Dispersion relations of Eq. (4.8), derived in Eq. (4.9). The effective NLS focusing and defocusing regions are represented by white and black areas, respectively. The colored dots correspond to the pair of Ω and k used in Sec. 4.4 to generate lattice envelope solitons. On the panel (a), the dispersion relation corresponds to FlexMM 1 defined by the following set of parameters: $\alpha = 1.815$, $K_s = 0.1851$, $K_\theta = 1.534\text{e}^{-2}$. For panel (b), the FlexMM 2 parameters are: $\alpha = 1.815$, $K_s = 0.01851$, $K_\theta = 1.534\text{e}^{-4}$.

is the width, A_0 the amplitude, and c the velocity of the soliton at the co-moving frame coordinate system $\xi = X - v_g T$.

Using Eq. (4.12), the rotation θ_1 for $c = 0$ is found to be

$$\theta_1(X,T) = 2A_0 \text{sech}\left[\frac{\epsilon}{Le}(X - X_0 - v_g T)\right] \cos[kx - \Omega T]\,. \tag{4.26}$$

The angular frequency of the carrier wave,

$$\Omega = \omega^{(2)} - \epsilon^2 \frac{QA_0^2}{2}, \tag{4.27}$$

has been shifted at order ϵ^2, in comparison to the linear dispersion relation $\omega^{(2)}$ due to nonlinearity. Depending on the sign of Q, the shift can occur above or below the linear branch.

The combination of Eqs. (4.24) and (4.17) gives the following expression for the dc-term,

$$U_0(X,T) = \frac{A_0^2 L_e}{v_g^2 - 1} \tanh\left[\frac{\epsilon(X - X_0) - \epsilon v_g T}{L_e}\right]. \tag{4.28}$$

Equations (4.26) and (4.28) constitute a polarized envelope nonlinear wave solution of Eq. (4.8) which is propagating with a common velocity determined by the spatial frequency of the carrier wave, defined as $v_g = \frac{d\omega^{(2)}}{dk} = -\frac{\alpha^2(K_s - K_\theta)\sin k}{\omega^{(2)}}$. From now on, we refer to it as bright envelope vector soliton (BEVS). We can note that the shape of the U field physically corresponds to a longitudinal contraction of the chain around the maximum of rotating sites during the propagation of the BEVS.

4.4.2. Bright Envelope vector soliton propagation in FlexMM

Direct numerical simulations of the discrete set of equations (4.8) are employed to validate our analytical predictions. The system (4.8) is solved using a fourth-order Runge-Kutta iterative integration scheme for a total of $N = 1000$ sites, with free boundary conditions at both ends. The results presented in section 4.4 were obtained by performing the integration for a duration of eight nonlinear times: $t_f = 8T_{NL}$ [55]. T_{NL} is based on the initial condition (IC) amplitude A_0, the system nonlinearity Q and the carrier wave number k, cf. Eq. (4.23). The relationship between T_{NL}, A_0 and Q is given by,

$$T_{NL} = \frac{1}{\epsilon^2 |Q| A_0^2}\,. \tag{4.29}$$

The initial conditions are taken to be,

$$\theta(X,0) = \epsilon\theta_1(X,0)\,, \quad \dot{\theta}(X,0) = \epsilon\dot{\theta}_1(X,0)\,, \tag{4.30}$$

$$U(X,0) = \epsilon U_0(X,0)\,, \quad \dot{U}(X,0) = \epsilon\dot{U}_0(X,0)\,, \tag{4.31}$$

using Eqs. (4.26-4.28) with $X_0 = N/2 = 500$. The initial amplitude A_0 chosen for the next simulations is defined as $A_0 = A\sqrt{\frac{2P}{Q}}$ with $A = 15$. When $P = 1/2$ and $Q = 1$, $A_0 = A$ is the amplitude of the bright soliton of the normalized NLS equation. Defining the amplitude A_0 as a function of P and Q implies, from the perspective of the NLS model, that the bright soliton initial conditions for FlexMM1 and FlexMM2, represented in Figs. (4.4-4.5-4.7), are the same.

Nonlinear dynamics of FlexMM 1

We start by studying the first FlexMM structure characterized by the dispersion relation shown in Fig. 4.3(a), that as one can see, the upper cut-off frequencies of the two branches are close $\omega_c^{(2)} \approx \omega_c^{(1)} = 2$. We will focus on the small k region where the effective NLSE is focused and thus BEVS is predicted. In Fig. 4.4, we show the nonlinear dynamics of an initial condition with a BEVS with $k = 0.1885$, corresponding to the green circle point of Fig. 4.3(a). The dynamics confirm that indeed the IC evolves as a BEVS and propagates with a constant velocity keeping its shape undistorted in the form of an envelope for rotations θ (Fig. 4.4(a),(c)) and a kink for displacement U (Fig. 4.4(b)).

For a more systematic study, we have performed numerical simulations of BEVS with different wavenumbers, within the focusing NLS region. In figure 4.5 (a-b), we show the solution profile at the final time $t_f = 8T_{NL}$ for three cases corresponding to the three circles (orange, green, and blue) in Fig. 4.3(a). Superimposed are the theoretical solutions (black lines) given by Eqs. (4.26-4.28).

As expected, the orange one ($k = 0$) remains centered at X_0 due to $v_g = 0$, see dispersion relation curves Fig. 4.3(a). The other two ($k = \{0.1885, 0.3770\}$) move in the left direction due to negative group velocities, with different velocities. Overall, analytical predictions and simulation results are in good agreement. The BEVS predicted by the NLS bright soliton show a robust behavior after eight nonlinear times, confirming the validity of the effective NLSE. This is the first signature that BEVs exist and propagate through the lattice. For the three cases, final times of integration are close, $t_f(k = 0) \approx 1013$, $t_f(k = 0.1885) \approx 1020$, $t_f(k = 0.3770) \approx 1031$.

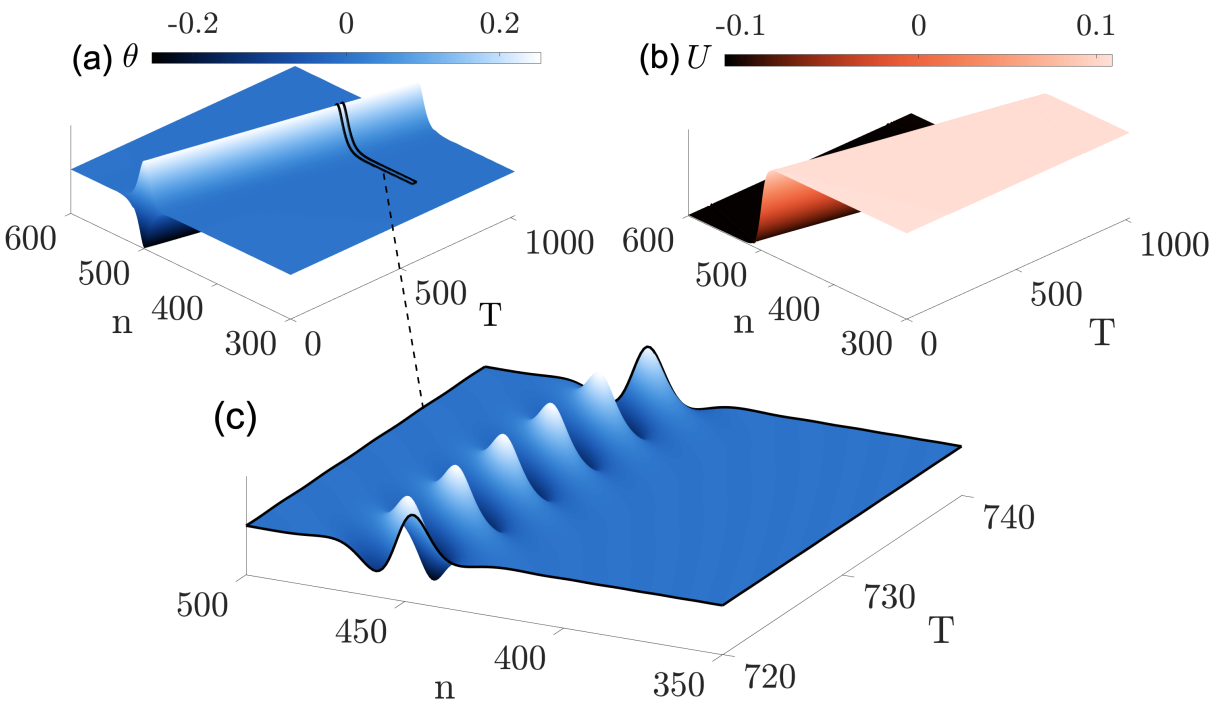

Figure 4.4: Evolution in time (T) of the amplitudes of the rotational (a-c) and longitudinal (b) displacements along the chain (n). The results correspond to a FlexMM (FlexMM 1) defined by the following set of parameters: $\alpha = 1.815$, $K_s = 0.1851$, $K_\theta = 1.534\text{e}^{-2}$. The initial condition corresponds to a BEVS with $k = 0.1885$ and $A = 15$, and a perturbation of $\epsilon = 0.01$.

For a more complete analysis, in appendix D we show the nonlinear dynamic response of the structure initially excited by Eqs. 4.30-4.31 in the case of a defocusing eNLS equation.

Another signature of the BEVS propagating through the lattice can be extracted from the nonlinear dispersion relation (NDR). As shown in [132, 133], bright solitons correspond to straight lines in the NDR. To see this, let us use the space-time double Fourier transformation,

$$\tilde{\theta}_1(\omega, k) = \int_{-\infty}^{+\infty} \int_{-\infty}^{+\infty} \theta_1(X, T) e^{-ikX} e^{+i\omega T} \mathrm{d}X \mathrm{d}T, \tag{4.32}$$

using as $\theta_1(X, T)$ the BEVS solution, namely Eq. (4.26), at a chosen k_s and $\omega^{(2)}(k_s)$. We

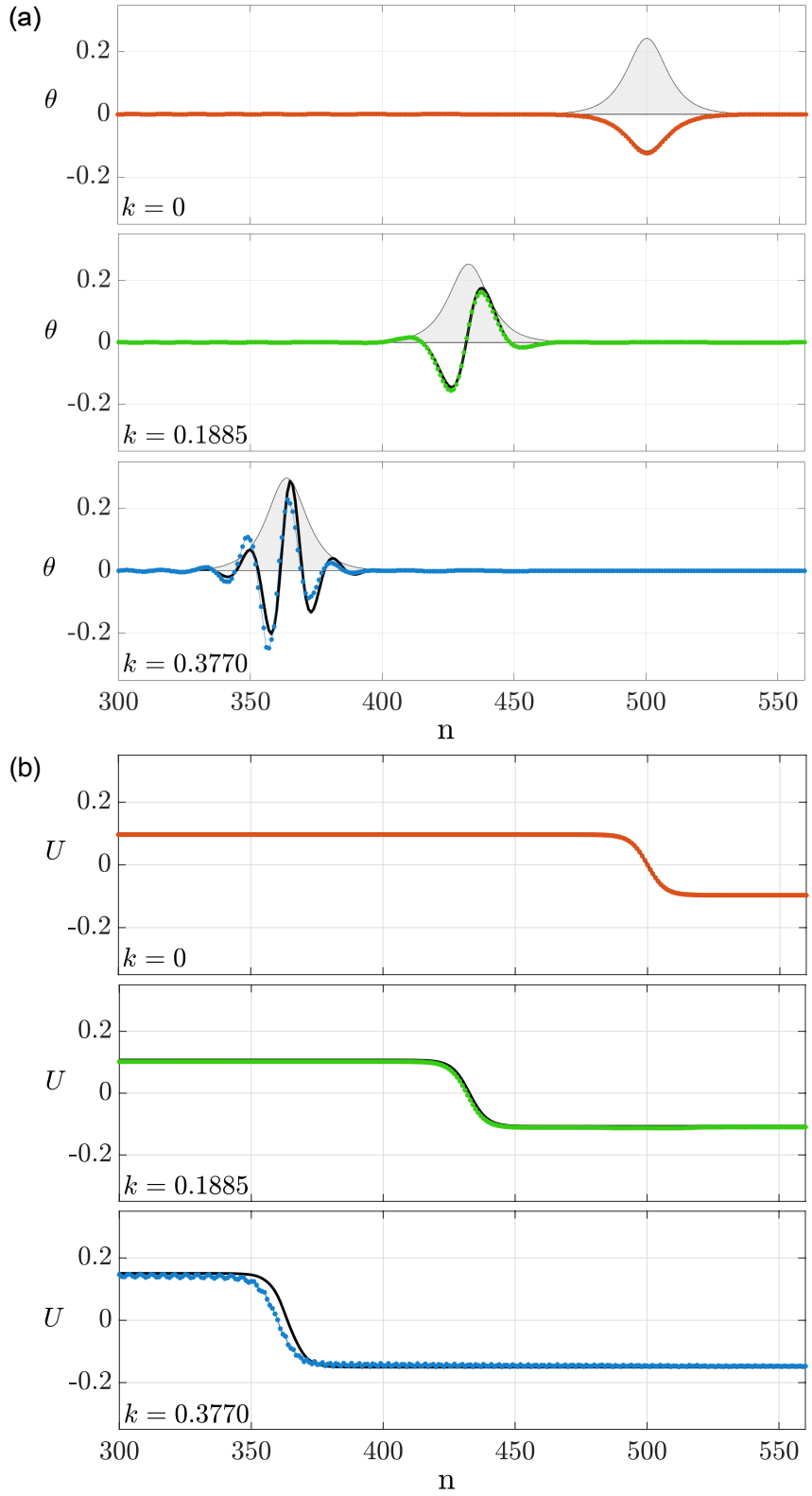

Figure 4.5: Rotational and longitudinal displacement amplitudes along the chain (n) at final time $t_f = 8T_{NL}$. The initial conditions correspond to BEVS with $k = 0$ in orange, $k = 0.1885$ in green and $k = 0.3770$ in blue, and an amplitude of $A = 15$, and a perturbation of $\epsilon = 0.01$.

obtain that,

$$\epsilon\tilde{\theta}_1(\omega,k) = 2\pi^2 A_0 L_e \text{sech}\left(\frac{\pi L_e(k-k_s)}{2\epsilon}\right) \mathrm{e}^{-iX_0(k-k_s)}\delta\left(\omega_s - \frac{Q\epsilon^2 A_0^2}{2} + v_g(k-k_s) - \omega\right) + 2\pi^2 A_0 L_e \text{sech}\left(\frac{\pi L_e(k+k_s)}{2\epsilon}\right) \mathrm{e}^{-iX_0(k+k_s)}\delta\left(-\omega_s + \frac{Q\epsilon^2 A_0^2}{2} + v_g(k+k_s) - \omega\right). \tag{4.33}$$

Using the Dirac function property, the value of $\delta(\omega_s - \frac{Q\epsilon^2 A_0^2}{2} + v_g(k-k_s) - \omega)$ and therefore $\tilde{\theta}_1$ is 0 except for points on the line,

$$\omega = v_g k + \left(\omega_s - v_g k_s - \epsilon^2 \frac{Q A_0^2}{2}\right). \tag{4.34}$$

Eq. (4.34) is the NDR of the BEVS which indeed is a straight line in the $\omega - k$ diagram.

Now, using the spatio-temporal dynamics, Fig. 4.4, we calculate the double FFT (in space and time). Since the lattice has two fields, $\theta_n(T)$ and $U_n(T)$, we apply the space-time double Fourier transform in both fields to obtain $\tilde{\theta}(\omega,k)$ and $\tilde{U}(\omega,k)$. In Fig. 4.6, we represented the normalized sum of the double FFT in space and time, in *log* scale,

$$\tilde{\psi}(\omega,k) = \left|\frac{\tilde{\theta}(\omega,k)}{\tilde{\theta}_{max}}\right| + \left|\frac{\tilde{U}(\omega,k)}{\tilde{U}_{max}}\right|. \tag{4.35}$$

As it is seen, a large amount of the 2D FFT (blue color gradient) closely matches the estimate line provided by Eq. 4.34, that is tangent to $\omega^{(2)}$ (yellow line) at point (Ω_s, k_s). This corresponds to the NDR of a bright soliton. An upper shift, of the order ϵ^2, cf. Eq. (4.27), compared to the linear dispersion relation $\omega^{(2)}$ is visible. In addition, low frequency components around $k = 0$ are observable, on the $\omega^{(1)}$curve . This corresponds to the dc-component of U of the BEVS solution.

Nonlinear dynamics of FlexMM 2

We now consider the FlexMM 2 configuration. Namely, the one that follows the dispersion relation shown in Fig. 4.3 (b) and which corresponds to the set of parameters used in experiments of [7, 8]. As one can see in Fig. 4.3 (b), this FlexMM supports rotational modes (blue curve) with frequencies that are much lower than those of the translational modes (red curve). In particular, the upper cutoff frequencies of the two branches are such that $\omega_c^{(2)} \ll \omega_c^{(1)} = 2$. Following the same analysis as before, we now use as an

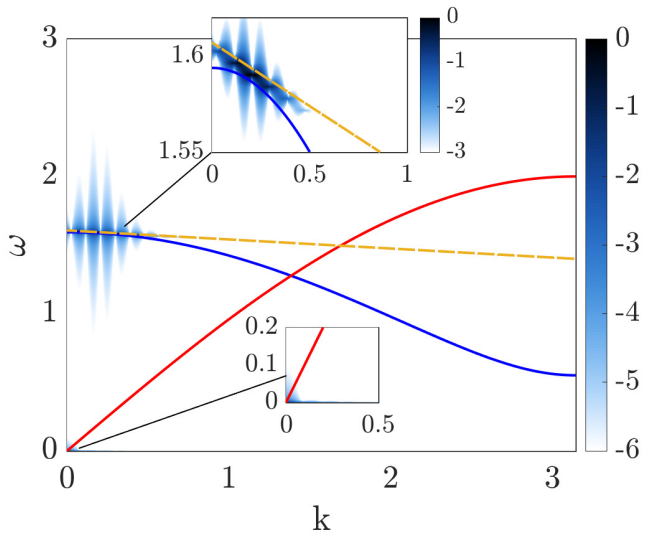

Figure 4.6: Numerical representation of the nonlinear dispersion relation of FlexMM 1 from its dynamics, represented in Fig. 4.4 using a normalized sum of the 2D-FFTs of the θ and U components. The red and blue curves denote the linear dispersion relation (see Fig. 4.3(a)), while the yellow line denotes NDR of the soliton described in Eq. (4.34). The color bar represents the $\tilde{\psi}(\omega, k)$, in *log* scale.

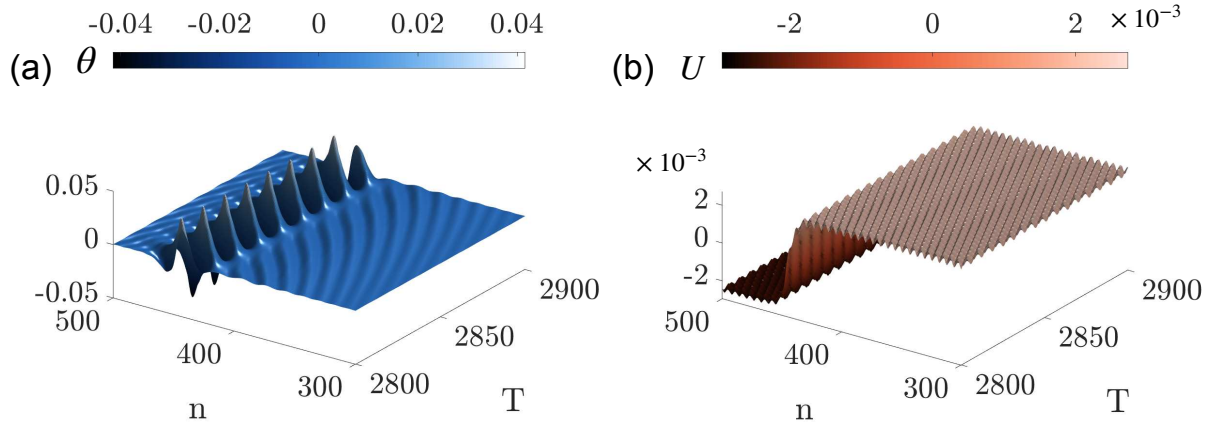

Figure 4.7: Evolution in time (T), for a duration between T=[2800; 2900], of the amplitudes of rotational (a) and longitudinal (b) displacements along the chain (n), zoomed between $n = [300; 500]$. The results correspond to a FlexMM (FlexMM 2) defined by the following set of parameters: $\alpha = 1.815$, $K_s = 0.01851$, $K_\theta = 1.534\text{e}^{-4}$. The bright soliton is generated by the initial conditions expressed in Eqs. (4.30-4.31) for a spatial frequency of $k = 0.1885$, an amplitude of $A = 15$, and a perturbation of $\epsilon = 0.01$.

initial condition Eqs. (4.30-4.31), that corresponds to a BEVS with $k = 0.1885$. The dynamics is shown in Fig. 4.7 The rotational dynamics is observed in panel (a), where it becomes evident that an envelope wave, in the form of a bright soliton, is propagating,

accompanied by the generation of additional small waves, with frequencies around Ω_s, that are radiated by the envelope wave. Note that we have confirmed that the strength of this radiation field is of the same order as that of FlexMM 1. The latter is not visible for the scales used in Fig. 4.4. From the dynamics of the longitudinal displacement, see panel (b), we observe a kink profile followed by small waves, at a frequency calculated to be around $2\Omega_s$, that move away at a relatively higher speed than the radiation observed in the rotation field. For a better understanding of these dynamics, we examine the temporal and spatial frequency spectra in Fig. 4.8.

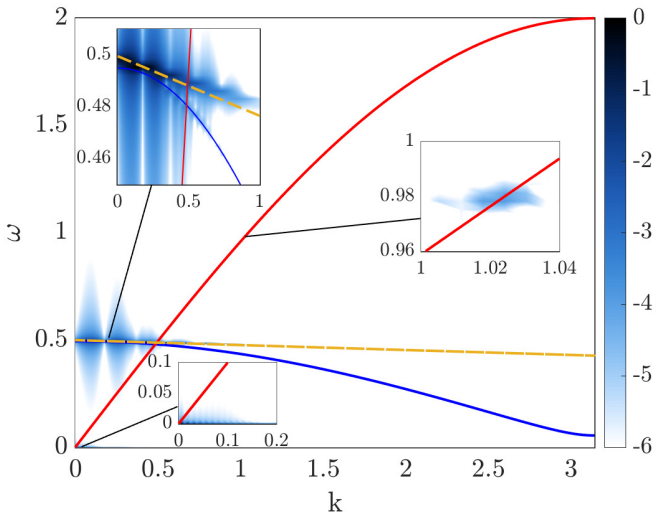

Figure 4.8: Numerical representation of the nonlinear dispersion relation of FlexMM 2 from its dynamics, represented in Fig. 4.7 using a normalized sum of the 2D-FFTs of the θ and U components. The red and blue curves denote the linear dispersion relation (see Fig. 4.3(b)), while the yellow line denotes NDR of the soliton described in Eq. (4.34). The color bar represents the $\tilde{\psi}(\omega, k)$, in *log* scale.

Here, we first note that a large amount of the 2D FFT is centered around the line that is tangent to $\omega^{(2)}$ at point (Ω_s, k_s). This corresponds to the NDR of a bright soliton. We also note that again we have spectral contribution around $k = 0$, coming from the dc-term, cf. Eq. (4.34). These two observations are a signature of the BEVS propagation through the lattice. However, in this case, we also observe significant components of the 2D FFT in other regimes of the $\omega - k$ space. In particular, we observe frequencies around $2\Omega_s$ belonging to the dispersion of the U DOF i.e., $\omega^{(1)}$ (see rightmost inset of Fig. 4.8) as expected by the quadratic terms in Eq. (4.11a). These frequency components correspond to the radiation field of U. Note that this was not the case for FlexMM 1, since this frequency was in the gap of the corresponding dispersion relation.

4.5. Dark envelope vector solitons

4.5.1. Theoretical prediction

In the previous section, we studied the existence and propagation of BEVS solutions in the dispersion relation region corresponding to the focusing eNLS equation, $PQ > 0$. Let us now turn our attention to the regions associated with a defocusing eNLSE, where $PQ < 0$. It is established that the defocusing eNLSE admits the following dark soliton solution [53],

$$F_1(\xi_1, \tau_2) = A_0 \tanh\left[\frac{1}{L_e}(\xi_1 - \xi_0)\right] e^{-iQA_0^2\tau_2}\,, \tag{4.36}$$

where A_0 is its amplitude and L_e is its width (see Eq. (4.25)). Following the steps presented in section 4.4, we derive the subsequent analytical solution for the rotation,

$$\theta_1(X, T) = 2A_0 \tanh\left[\frac{\epsilon}{L_e}(X - X_0 - v_g T)\right] \cos[kX - \Omega T]\,, \tag{4.37}$$

where Ω is the angular frequency. Its expression is given by,

$$\Omega = \omega^{(2)} + \epsilon^2 A_0^2 Q\,. \tag{4.38}$$

As for the bright soliton solution, cf. Eqs. (4.26-4.27), the angular frequency has undergone a shift at order ϵ^2, relative to the linear $\omega^{(2)}$. This shift can manifest itself either above or below the linear branch, depending on the sign of Q. The combination of Eq. (4.17) with the envelope part of Eq. (4.37) gives an expression for G_0 yielding,

$$U_0(X, T) = \frac{A_0^2}{v_g^2 - 1}\left(\epsilon(X - X_0 - v_g T) - L_e \tanh\left[\frac{\epsilon}{L_e}(X - X_0 - v_g T)\right]\right)\,. \tag{4.39}$$

Equations (4.37-4.39) form a polarized nonlinear wave solution which from now on will be called dark envelope vector soliton (DEVS).

4.5.2. Dark envelope vector soliton propagation in FlexMM

To validate our predictions regarding the existence of DEVS, we solve the discrete set of equations (4.8) using the process described in Sec. 4.4.2. We apply free boundary conditions at both ends of the structure and perform the integration over a duration of five nonlinear times: $t_f = 5T_{NL}$, cf. Eq. (4.29).

In the case of DEVS, the presence of a jump in the phase field, see Fig. 4.9, leads to a mismatch with the free boundary conditions, causing boundary effects that propagate through the lattice. To avoid these effects, similarly to [134, 135], we multiply the θ field

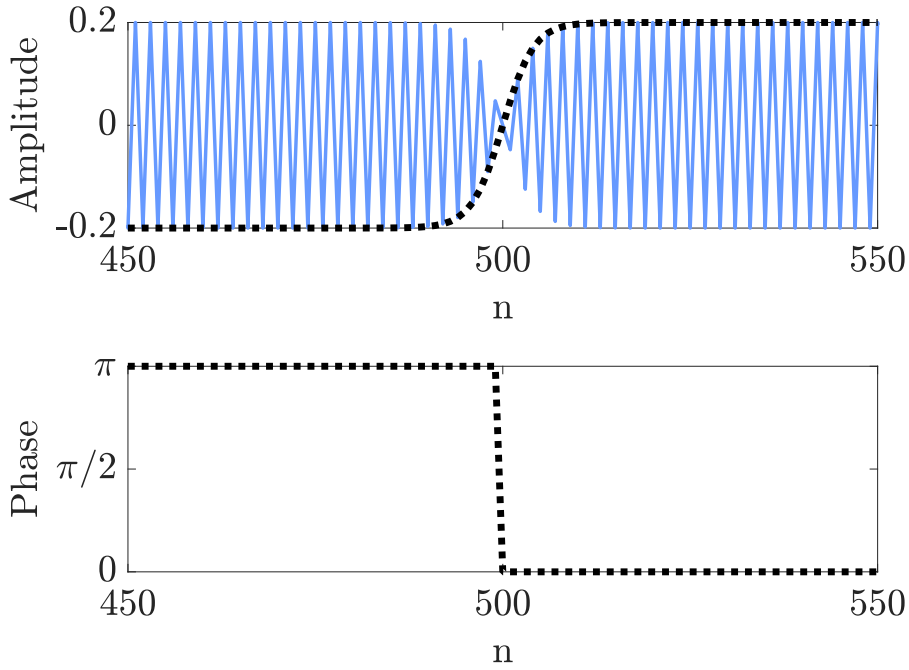

Figure 4.9: Analytical solution of the rotational component $\epsilon\theta_1$ (cf. Eq. (4.37)), and its corresponding phase at $T = 0$, for the DEVS of wave number $k = \pi$.

of Eq. (4.37) by a super-gaussian window $\mathcal{W}$ of the following form,

$$\mathcal{W} = e^{-\left(\frac{\xi_1-\xi_0}{S}\right)^p} = e^{-\left(\frac{(X-X_0-v_gT)}{s}\right)^p}, \tag{4.40}$$

centered on the initial position X_0, of the dark soliton. The width of the window is governed by $s = S/\epsilon$ where the p parameter controls the edges' sharpness. For the numerical simulations, we use $s = N/10 = 100$ and $p = 8$. The application of the spatial window $\mathcal{W}$ modulates to zero the initial rotation displacement and velocity near the boundaries. The dependence of G_0 on F_1 established by the combination of Eqs. 4.24 and 4.17 written,

$$G_0(\xi_1) = \frac{1}{v_g^2 - 1} \int |F_1|^2 d\xi_1, \tag{4.41}$$

involves that in the presence of the window $\mathcal{W}$, G_0 is now dependent on the product $F_1\mathcal{W}$. Substituting F_1 by $F_1\mathcal{W}$ by putting Eqs. (4.36-4.40) in Eq. (4.41) leads to,

$$G_0(\xi_1) = \frac{A_0^2}{v_g^2 - 1} \int \tanh^2\left(\frac{\xi_1 - \xi_0}{L_e}\right) e^{-2\left(\frac{\xi_1-\xi_0}{S}\right)^p} d\xi_1 \,. \tag{4.42}$$

The resulting integral has no analytical solution. Thus, the integration is numerically solved by computing the approximate cumulative integral of Eq. (4.42) via the trapezoidal method for each time step of the integration. At $T = 0$ the result gives the initial condition Eq. (4.43c). Performing the derivative in real-time (T), noted $\dot{(\,)}$, before the numerical integration allows to obtain the initial condition for the velocity Eq. (4.43d). Finally, the initial conditions employed to excite the lattice are,

$$\theta(X,0) = \epsilon\theta_1(X,0)\mathcal{W}(X,0)\,, \tag{4.43a}$$
$$\dot{\theta}(X,0) = \epsilon\dot{\theta}_1(X,0)\mathcal{W}(X,0) + \dots\,, \tag{4.43b}$$

$$U(\xi_1,0) = \frac{\epsilon}{v_g^2-1}\int |F_1|^2\mathcal{W}^2 d\xi_1\,, \tag{4.43c}$$
$$\dot{U}(\xi_1,0) = \frac{\epsilon}{v_g^2-1}\int |\dot{F_1}|^2\mathcal{W}^2 d\xi_1 + \dots\,. \tag{4.43d}$$

The $\dot{\mathcal{W}}$ terms in Eqs. (4.43b - 4.43d) can be neglected because they are proportional to ϵ^p. Moreover in the numerical simulations $\dot{\mathcal{W}}$ is proportional to ϵ^8.

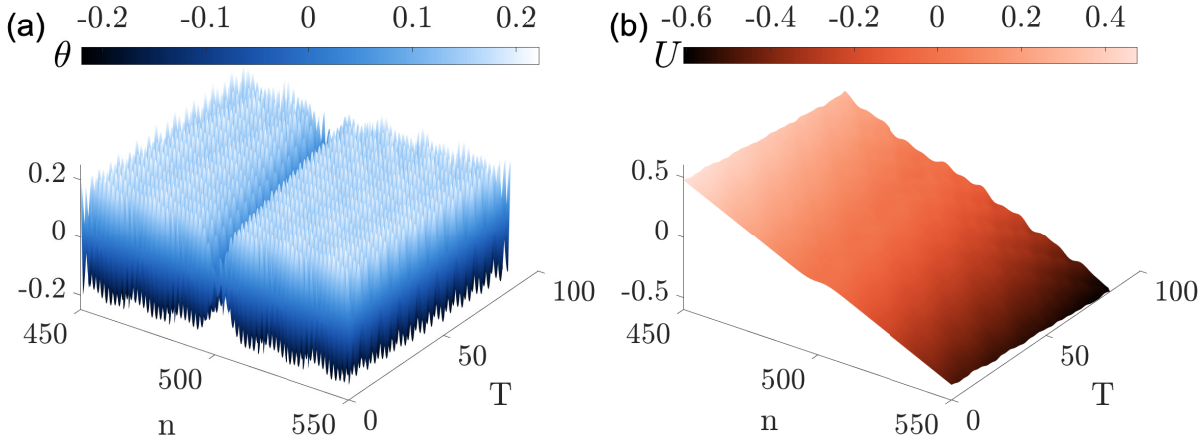

Figure 4.10: Panels (a-b) represent the evolution in time (T) of the rotational (a) and longitudinal (b) displacements along the chain (n). The results correspond to a FlexMM (FlexMM 1) defined by the following set of parameters: $\alpha = 1.815$, $K_s = 0.1851$, $K_\theta = 1.534\text{e}^{-2}$. A DEVS is generated by the initial conditions expressed in Eqs. (4.30-4.31), for a spatial frequency of $k = 2.9531$, and an amplitude of $\epsilon A_0 = 0.1$.

In Fig. 4.10, we show the nonlinear dynamics of the FlexMM 1, cf. Fig. 4.3(a), using as an initial condition a DEVS (Eq. 4.43) with $k = 2.9531$ (see green triangle in Fig. 4.3(a)). As one can see in Fig. 4.10(a), the envelope of the rotational DOF is a continuous dip that propagates at a constant velocity and maintains its shape. Moreover, the profile of U, displayed in Fig. 4.10(b), also remains approximately constant in time, a characteristic

of vector solitary waves according to our theoretical predictions. To complete the analysis, Fig. 4.11 represents DEVS at the final time of integration in FlexMM 1 for initial conditions with different wave numbers indicated by colored triangles in Fig. 4.3(a). We can see that the numerical results (color dotted lines) remain close to the theoretical ones, in terms of the carrier wave (black line) and of the absolute value of the envelope (gray area).

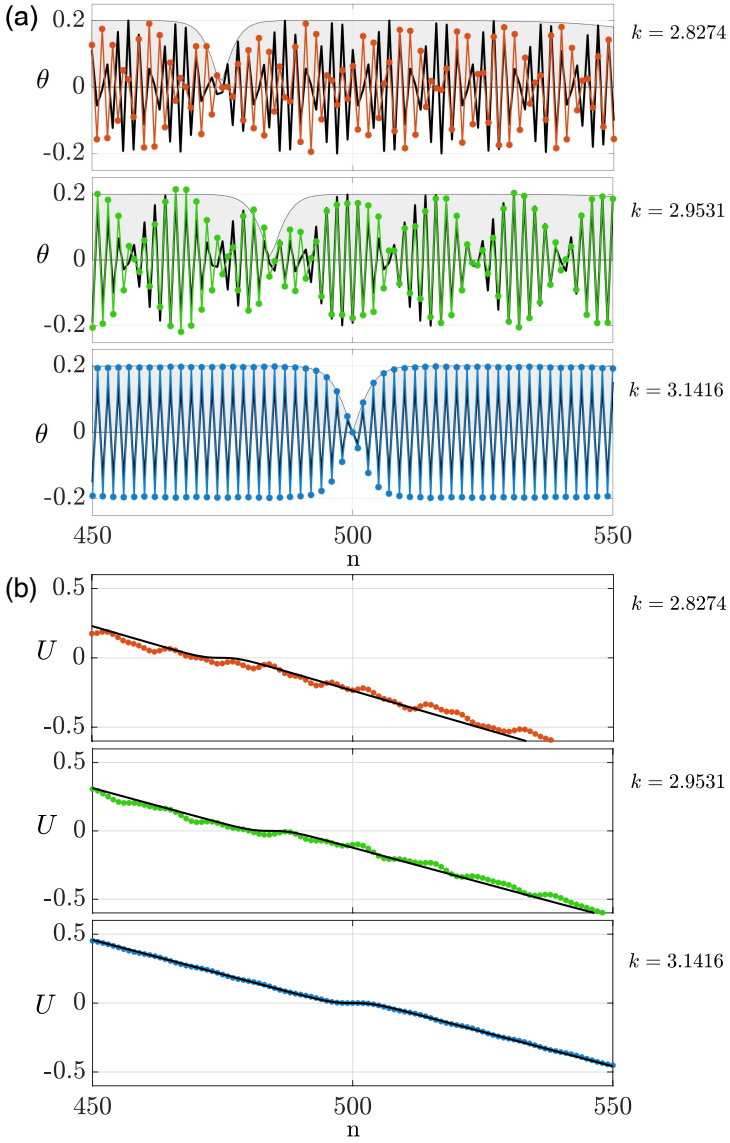

Figure 4.11: Rotational and longitudinal displacement amplitudes along the chain (n) at final time $t_f = 5T_{NL}$. The DEVS are generated by initial conditions: a spatial frequency of $k = 2.8274$ in orange, $k = 2.9531$ in green, and $k = \pi$ in blue. For the three cases, an amplitude of $A_0 = 10$ and a perturbation of $\epsilon = 0.01$ are used.

4.6. Conclusions

In this chapter, we demonstrated the generation and propagation of nonlinear envelope waves under the form of bright and dark envelope vector solitons. In particular, we found that the rotational DOF can be described by an eNLS equation and that longitudinal displacements follow the dynamics induced by the nonlinear coupling through a dc-term at the leading order. This dc-term was not observed in our studies on modulation instability phenomena [117]. Both analytical and numerical results show that with an appropriate choice of physical parameters for the FlexMM, in particular, specific combinations of inertia α and stiffness parameters (K_s and K_θ), the propagation of these solutions in FlexMMs becomes feasible and robust. This demonstrates the significant versatility offered by the proposed system in the manipulation of weakly nonlinear modulated waves.

5 | Gradient catastrophe and Peregrine soliton in nonlinear flexible mechanical metamaterials

Contents

In this final chapter, we investigate the generation of extreme wave events using the regularization of the gradient catastrophe theory developed by A. Tovbis and M. Bertola for the nonlinear Schrödinger equation (NLS). According to this theory, Peregrine solitons can locally emerge in the semiclassical limit of the NLS equation. Our objective is to investigate whether the phenomenon of gradient catastrophe can occur in FlexMM structures, in the regime where the effective focusing NLS model, described in chapter 4, is valid.

5.1. Introduction

Rogue or freak waves are fascinating oceanic extreme phenomena that are rare and unpredictable. These giant waves emerge seemingly *"from nowhere"* [136], towering over surrounding waves. Due to their rarity and the difficulty in predicting their occurrence, they are a threat to maritime safety and infrastructure [137, 138]. Before 1995, many scientists questioned the existence of these mysterious giant waves because of the lack of proof and explanation. When the first measurement of rogue waves was done on the Draupner platform in the North Sea, the scientific community increasingly started recognizing rogue waves as a real complex natural phenomenon.

Studies have revealed that rogue waves are omnipresent [139, 140] and that they can appear in different contexts, induced by various linear and nonlinear mechanisms [141, 142]. This diversity makes it challenging to establish a simplified definition of these unusual events [143]. For example, constructive interference of wave groups [144] is a linear mechanism that amplifies wave heights, described by linear theories. Wave-current interactions, as well as underwater topographical features, including shoals or deep canyons [145, 146, 139], can also contribute to wave steepening leading to rogue wave formation. In addition, external factors such as atmospheric forcing [147, 148] can promote the growth of large wave groups. Wind applies pressure variations, transferring energy to the ocean surface. However, linear wave theory is limited in its ability to explain both the spontaneous occurrence and the extreme height of larger rogue waves. Indeed, these phenomena are much more frequent than the wave height distribution predicted [149] (Rayleigh distribution). As a result, the study of nonlinear ocean dynamics has gained increasing popularity in understanding the stability and interactions of ocean waves which lead to the formation of coherent structures. It has been shown that ocean dynamics in the deep water limit are mathematically described by the nonlinear Schrödinger equation [63].
This very same equation was found to describe accurately many other physical systems [73, 53, 71]. This has led scientists to generalize the study of extreme wave events to many

other physical disciplines, such as nonlinear optics [99, 84], Bose-Einstein condensates [150], plasma physics [151], as well as discrete systems as transmission lines [55, 152]or mechanical systems [153].

The one-dimensional focusing NLS equation supports different dynamical mechanisms that lead to the emergence of coherent structures. For example, the modulation instability phenomenon, studied in Chap. 3 which originates in the exponential growth of the perturbations of an unstable plane wave background can be triggered by either random or deterministic processes. From another point of view, isolated coherent pulses and partially coherent fields [154] can demonstrate self-focusing dynamics. For instance, solitons on finite backgrounds or breathers have been identified. Amongst those, the Peregrine soliton (PS), localized both in time and space, may be appropriate to describe unique wave events [155, 107, 51, 83].

Recent mathematical proofs [156] have shown that in the semiclassical limit of the 1D focusing NLSe, a universal mechanism regularizes the gradient catastrophe, leading to the local emergence of a Peregrine soliton. This phenomenon has already been experimentally observed in fiber optics [100, 101] and water tanks [157]. We aim to apply this knowledge to FlexMM structures to control the emergence of coherent structures both temporally and spatially.

First of all, in Sec. 5.2, we present an overview of the FlexMM structure and its associated equations of motion. The effective NLS equation, derived in Sec. 5.3, is then discussed to stay in the service mi-classical limit. The Peregrine soliton and the theoretical concept of gradient catastrophe regularization are presented. We show in Sec. 5.5, via an initial condition problem that the dynamics of the NLS model are consistent with the dynamics of FlexMMs.

5.2. System and equations of motion

As the structure is presented in detail in chapters 3 and 4, we provide only a brief presentation in this section. For further information, please refer to the chapter 4. Using a lumped-element approach, the FlexMM structure can be modeled in the low-frequency regime by a one-dimensional chain made of rigid units of mass m and inertia moment J, periodically connected by three massless springs, a longitudinal spring with stiffness k_l, a shear spring with shear stiffness k_s, and a bending spring with bending stiffness k_θ. We consider only symmetric motion relative to the symmetry axis between the two lines which means each mass of the system has two DOFs, a longitudinal displacement U and a rotational motion θ where the sign of the rotation angles is considered positive in the

trigonometric direction.

From this assumption, the normalized equations of motion of the system write,

$$\frac{d^2U_n}{dT^2} = U_{n+1} - 2U_n + U_{n-1} - \frac{\cos\theta_{n+1} - \cos\theta_{n-1}}{2}\,, \tag{5.1a}$$

$$\begin{aligned}\frac{1}{\alpha^2}\frac{d^2\theta_n}{dT^2} &= K_\theta\left(\theta_{n-1} - 4\theta_n + \theta_{n+1}\right) - K_s\cos\theta_n\left[\sin\theta_{n-1} + 2\sin\theta_n + \sin\theta_{n+1}\right] \\ &\quad - \sin\theta_n\left[2(U_{n+1} - U_{n-1}) + 4 - \cos\theta_{n-1} - 2\cos\theta_n - \cos\theta_{n+1}\right]\,,\end{aligned} \tag{5.1b}$$

where the following normalized variables and parameters are introduced: the longitudinal displacement of unit n, $U_n = u_n/a$, the normalized time $T = t\sqrt{k_l/m}$, an inertial parameter $\alpha = a\sqrt{m/(4J)}$, and stiffness parameters $K_\theta = 4k_\theta/\left(k_l a^2\right)$ and $K_s = k_s/k_l$. The parameters chosen to build the virtual FlexMM are those used in chapter 4 Sec. 4.4, i.e. FlexMM1, they are the following,

$$\alpha = 1.815, \quad K_s = 0.1851, \quad K_\theta = 1.534\mathrm{e}^{-2}. \tag{5.2}$$

In the linear limit, the two motions (transversal and rotational) are decoupled, i.e. each DOF follows its own dynamics. The corresponding dispersion relations are given by,

$$\omega^{(1)} = 2\sin\left(\frac{k}{2}\right)\,, \tag{5.3a}$$

$$\omega^{(2)} = \pm\sqrt{4\alpha^2(K_s - K_\theta)\cos^2\left(\frac{k}{2}\right) + 6\alpha^2 K_\theta}\,. \tag{5.3b}$$

Displayed in figure 4.1(c), the red branch corresponds to propagating longitudinal waves ($\omega^{(1)}$). It exhibits a typical monoatomic dispersion relation, see Eq. (5.3a). The second branch, described by Eq. (5.3b), represents propagating rotational waves with an inverse Klein-Gordon type dispersion relation ($\omega^{(2)}$). Notably, this branch has an upper cutoff frequency at $\omega_c^{(2)} = \alpha\sqrt{4K_s + 2K_\theta}$.

5.3. Effective nonlinear Schrödinger equation

From Chap. 4, we build a theoretical model using the semi-discrete approximation in order to describe the propagation of slow-modulated traveling waves of the following form, in the weakly nonlinear regime,

$$\begin{aligned} U_n &= \epsilon U_0 + \epsilon^2 U_2 \,, \\ &= \epsilon G_{0,n}(T) + \epsilon^2 (G_{2,n}(T) e^{2i\sigma_n} + G^*_{2,n}(T) e^{-2i\sigma_n}) \,, \end{aligned} \tag{5.4a}$$

$$\begin{aligned} \theta_n &= \epsilon \theta_1 \\ &= \epsilon (F_{1,n}(T) e^{i\sigma_n} + F^*_{1,n}(T) e^{-i\sigma_n}) \,. \end{aligned} \tag{5.4b}$$

In this ansatz, $F_{1,n}$ is the envelope of the modulated plane wave θ_n determined in the continuum limit. The fast oscillations of the carrier wave of phase $\sigma_n = kn - \omega T$ are treated exactly obeying the discrete dispersion relation. Due to the quadratic coupling terms $\sim \theta^2_{n\pm1}$ in Eq. (4.11), the ansatz U_n must include both a dc-term $G_{0,n}$ and a term $G_{2,n}$ oscillating with a phase $2\sigma_n$ to model the first order harmonics generated.

It has been proved in Sec. 4.3 that the envelope of the modulated wave θ_n follows a nonlinear Schrödinger equation,

$$i\frac{\partial F_1}{\partial \tau_2} + P\frac{\partial^2 F_1}{\partial \xi_1^2} + Q|F_1|^2 F_1 = 0 \,, \tag{5.5}$$

with,

$$P = \frac{\alpha^2 (K_\theta - K_s)\cos(k) - v_g^2}{2\omega} \,, \tag{5.6a}$$

$$Q = \frac{1}{2\omega}\left[8K_s\alpha^2\cos^2\left(\frac{k}{2}\right) - \alpha^2(5+\cos(2k)) + \frac{\alpha^2\sin^2(2k)}{2\left(\sin^2(k)-\omega^2\right)} - \frac{4\alpha^2}{v_g^2-1}\right] , \tag{5.6b}$$

where P and Q are coefficients that depend on the structure geometry and the wave number used in the initial conditions. The analysis of the focusing respectively defocusing region has been displayed in Fig. 4.3(a) for more details. G_0 and G_2 can be directly computed from F_1,

$$G_0(\xi_1, \tau_2) = \frac{1}{v_g^2 - 1}\int |F_1(\xi_1, \tau_2)|^2 d\xi_1 \,, \tag{5.7a}$$

$$G_2(\xi_1, \tau_2) = \frac{i\sin(2k)}{8\left(\sin^2(k)-\omega^2\right)} F_1(\xi_1, \tau_2)^2 \,. \tag{5.7b}$$

$\xi_1 = \epsilon(X - v_g T)$ and $\tau_2 = \epsilon^2 T$ are the time and space scales used for the development. They are defined from the multiple scales method.

We have shown that Eq. (5.5) is an accurate model to predict and control the evolution of bright envelope vector soliton solutions, see Eq. (4.24). It is known that the evolution of solitons can be robust due to a perfect balance between nonlinearity (which tends to

focus the wave) and dispersion (which tends to spread the wave). When the nonlinearity is much stronger than the dispersion, the wave behavior is dominated by nonlinear effects.

5.3.1. Semiclassical limit

The semiclassical limit (also known as zero dispersion limit) of the NLS equation corresponds to the strongly nonlinear regime obtained when the dispersion is much weaker than the nonlinearity. For the semiclassical limit analysis, the NLS equation can be written in the following form,

$$i\frac{\partial\psi}{\partial\mathcal{T}} + \frac{1}{2N}\frac{\partial^2\psi}{\partial\mathcal{X}^2} + N|\psi|^2\psi = 0\,, \tag{5.8}$$

where N is the soliton number (see below) and ψ, $\mathcal{X}$ and $\mathcal{T}$ are given by the following normalization relations,

$$\psi = \frac{F_1}{A_0}\,, \quad \mathcal{T} = \frac{\tau_2}{\sqrt{T_{NL}T_D}}\,, \quad \mathcal{X} = \frac{\xi_1}{L_e}\,. \tag{5.9}$$

The soliton number $N > 0$, which may not be an integer, controls the dispersion-nonlinearity ratio,

$$N = \sqrt{\frac{T_D}{T_{NL}}}\,, \tag{5.10}$$

where $T_D = \frac{L_e^2}{2|P|}$ and $T_{NL} = \frac{1}{|Q|A_0^2}$ are the characteristic dispersive and nonlinear times, defined by the amplitude A_0 and width L_e of the initial pulse. When N is an integer, an N-soliton solution [158] of Eq. (5.8) at $\mathcal{T} = 0$ gives,

$$\psi(\mathcal{X}, 0) = \mathrm{sech}\,(\mathcal{X})\ . \tag{5.11}$$

These solitons exhibit more complex dynamics than the fundamental 1-soliton, including periodic oscillations called breathers or multi-peak structures produced by the interaction and the superposition of multiple fundamental solitons, explained by the Inverse Scattering Transform method [158]. In the semiclassical limit of the one-dimensional focusing NLS equation, recent studies [100, 101, 132] revealed that another fundamental mechanism, called gradient catastrophe, leads to the emergence of localized structures using the self-focusing property of the NLS equation. These localized structures have been proven to asymptotically (when $N \to \infty$) approach the Peregrine soliton [156, 100].

5.3.2. Peregrine soliton of the NLSE

The Peregrine soliton is a rational solution of the NLS equation originally proposed in 1983 by D.H. Peregrine [155]. It is a spatiotemporal localized solution of high amplitude with a stiff wavefront profile. Mathematically, the Peregrine soliton solution to the NLS equation of the form of Eq. (5.8) is expressed as,

$$\psi(\mathcal{X},\mathcal{T}) = a_0 \frac{1-4[1+2ia_0^2N(\mathcal{T}-\mathcal{T}_m)]}{1+4a_0^2N^2\mathcal{X}^2+4a_0^4N^2(\mathcal{T}-\mathcal{T}_m)^2} e^{ia_0^2N(\mathcal{T}-\mathcal{T}_m)}, \tag{5.12}$$

where a_0 is the continuous background amplitude and $\mathcal{T}_m$ is the moment of maximum compression. The analytical PS, cf. Eq. (5.12), is displayed in Fig. 5.1.

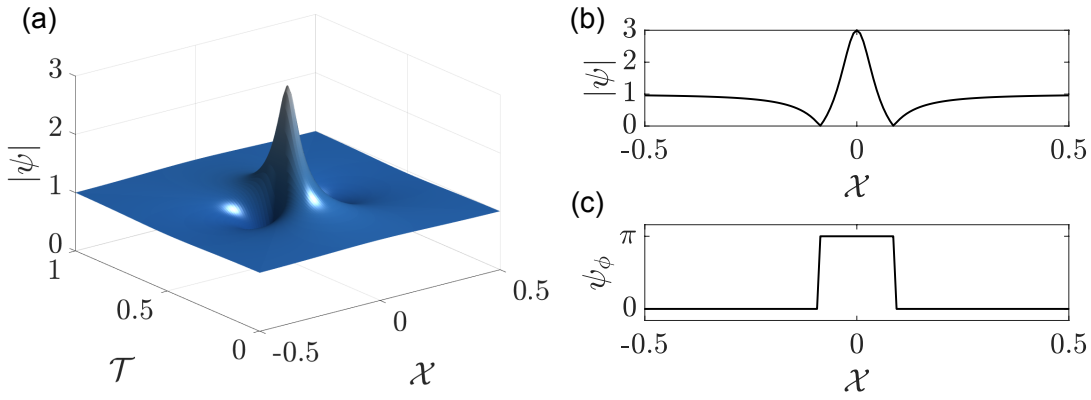

Figure 5.1: Analytical Peregrine soliton solution of the NLS equation, cf. Eq. (5.8), for $N = 10$ and $a_0 = 1$. In panel (a), a spatiotemporal representation is displayed while in panels (b-c), a cross-section at the maximum compression moment $\mathcal{T} = \mathcal{T}_m = 0.5$ of the amplitude and phase profile is visible.

At the maximum compression moment, visible in Fig. 5.1 (b), the amplitude of the PS reached three times the continuous background amplitude $\psi(0,\mathcal{T}_m) = 3a_0$ including a π-phase jump, see Fig. 5.1 (c). After this point, the amplitude of the solution decreases, expands, and finally disappears, see Fig. 5.1 (a). The shape and its localization in both space and time, resemble the sudden and transient nature of rogue waves [159]. This is why Peregrine soliton is often considered as a possible explanation of this kind of event.

5.4. Local emergence of the Peregrine soliton by the regularization of the gradient catastrophe

In the semiclassical limit of the one-dimensional focusing nonlinear Schrödinger equation, for $N \gg 1$, it has been established [100, 84] that during the initial stages of its evolution, a wide pulse undergoing propagation is primarily influenced by nonlinear effects, while dispersive effects are negligible. This dominance of nonlinearity leads to a self-steepening of both the phase and amplitude profiles of the pulse, reaching a critical point $(\mathcal{T}_c,\, \mathcal{X}_c)$ where the derivatives of phase and amplitude become infinite. At this point, the gradient catastrophe phenomenon emerges, localized at position $\mathcal{X}_c$ and moment $\mathcal{T}_c$. Following the gradient catastrophe occurrence ($\mathcal{T} > \mathcal{T}_c$), dispersive effects cannot be ignored, leading to the regularization of the gradient catastrophe through the emergence of localized breathers. From mathematical predictions [156], the maximum compression point occurs at time,

$$\mathcal{T}_m = \mathcal{T}_c + CN^{-4/5}\,, \tag{5.13}$$

with C a universal constant defined as,

$$C = 2.38\left(\frac{5|C_1|}{4}\right)^{1/5}(2b_0)^{-3/2}\left(1+\mathcal{O}\left(N^{-4/5}\right)\right)\,. \tag{5.14}$$

When the initial pulse is an N-soliton solution,

$$\mathcal{T}_c = 1/2\,, \qquad b_0 = \sqrt{2}\,, \qquad C_1 = \frac{32\sqrt{2i}}{15\times 2^{9/4}}\,. \tag{5.15}$$

The first localized structure that emerges can be asymptotically approximate to a Peregrine soliton of the NLSE, cf. Eq. (5.12). For $N \to \infty$, the amplitude of the Peregrine soliton reaches the asymptotic limit $\psi(\xi, \mathcal{T}_m) = 3\sqrt{2}$.

5.5. Comparison of the gradient catastrophe phenomenon in the FlexMM and in the NLSE

The theoretical concept and main results for the gradient catastrophe phenomenon regularization have been presented. Now, we would like to find out whether such a phenomenon can be observed in FlexMM structures. From the effective NLS equation of the architected structure, the initial conditions can be determined. In the next sections,

we compare the dynamics of the FlexMM with the effective NLS equation evolution. To this end, we have carried out a series of simulations on both the NLS equation and the FlexMM discrete-lattice equations of motion. As the phenomenon is known for the NLS equation, the aim here is to vary the number of N-soliton solutions to numerically prove that the first emerged localized structure in the rotational evolution of the FlexMM can also be well fit by a Peregrine soliton.

5.5.1. Numerical integration of the NLS equation and FlexMM equations of motion

To numerically solve the NLS equation Eq. (5.8), we use the exponential time difference fourth-order Runge-Kutta (ETDRK4) scheme [160, 161]. It is a powerful integration scheme that provides a robust, accurate, and efficient solution for stiff differential equations by exactly handling the stiffness arising from the linear components of the system. More information is available in appendix E. The integration is done using an exact N-soliton solution as an initial condition,

$$\psi(\mathcal{X}, \mathcal{T} = 0) = \text{sech}\,(\mathcal{X}) \ . \tag{5.16}$$

Direct numerical simulations of the discrete set of equations (5.1) are employed to validate the analytical predictions and to compare them to the NLS equation evolution. The system (5.1) is solved using a fourth-order Runge-Kutta iterative integration scheme with free boundary conditions at both ends.

As an initial condition, we use the N-soliton solution, Eq. (5.16). The latter can be expressed in (τ_2, ξ_1) variables as,

$$F_1(\xi_1, 0) = A_0 \text{sech}\left(\frac{\xi_1}{L_e}\right) \ , \tag{5.17}$$

with

$$L_e = \frac{N}{A_0}\sqrt{\frac{2|P|}{|Q|}} \ , \tag{5.18}$$

where A_0 is the amplitude of the pulse in the co-moving frame coordinate system and where $\xi_1 = \epsilon(X - v_g T)$.

To determine the initial conditions for the FlexMM dynamical equations, namely the

corresponding lattice waves for θ and U fields, using Eq. (5.4), we obtain for the rotation,

$$\theta_1(X,0) = 2A_0 \mathrm{sech}\left[\frac{\epsilon}{L_e}(X - X_0)\right]\cos(kx)\,. \tag{5.19}$$

k is the wave number of the carrier wave following the dispersion relation of the θ branch, cf. Eq. (5.3b). The combination of Eqs. (5.17) and (5.7a) gives the following expression for the dc-term initial condition,

$$U_0(X,0) = \frac{A_0^2 L_e}{v_g^2 - 1}\tanh\left[\frac{\epsilon(X - X_0)}{L_e}\right]\,. \tag{5.20}$$

The initial conditions on the velocity $\dot{\theta}_1(X,0)$ and $\dot{U}_0(X,0)$ are deduced from the anlytical expression in Chap. 4 of the BEVS expressed in Eqs. (5.19-5.20). Since the solution only is taken into account up to the first order of perturbation (ϵ), the initial conditions write,

$$\theta(X,0) = \epsilon\theta_1(X,0)\,, \quad \dot{\theta}(X,0) = \epsilon\dot{\theta}_1(X,0)\,, \tag{5.21}$$

$$U(X,0) = \epsilon U_0(X,0)\,, \quad \dot{U}(X,0) = \epsilon\dot{U}_0(X,0)\,. \tag{5.22}$$

For the simulations, the initial condition is centered at X_0, the middle of the lattice.

Here are some details on the parameters used to run the simulations.

- *FlexMM* - The integration of the equations of motion is done on $n_s = 2000$ sites for a total time of $T_f = 10^4$, with time step $dt = 0.05$. The initial amplitude is $A_0 = 5$, the wave number of the carrier wave is set to $k = 0$ and $\epsilon = 0.01$.

- *NLS* - For the ETDRK4 scheme, the integration is done for $\mathcal{T}_f = \epsilon^2 T_f\sqrt{T_{NL}T_D}$, with time step $h = 1\mathrm{e}^{-3}$. The space is a grid of size $L_x = \epsilon n_s/L_e$ divided in $N_x = 2^{10}$ points.

5.5.2. Higher-order solitons in FlexMM

In this section, we focus on the higher-order soliton solutions of FlexMMs, predicted by the effective NLS equation. In the first row of Fig. 5.2, we display the results of the numerical integration of the NLS equation (cf. Eq. (5.8)), while in the second (third) row, we show the numerical results of the lattice equations (cf. Eq. (5.1)), for the rotational (longitudinal) component, choosing $N = \{2, 3, 4\}$.

Let us first discuss the $N = 2$ soliton solution. It corresponds to the first column of

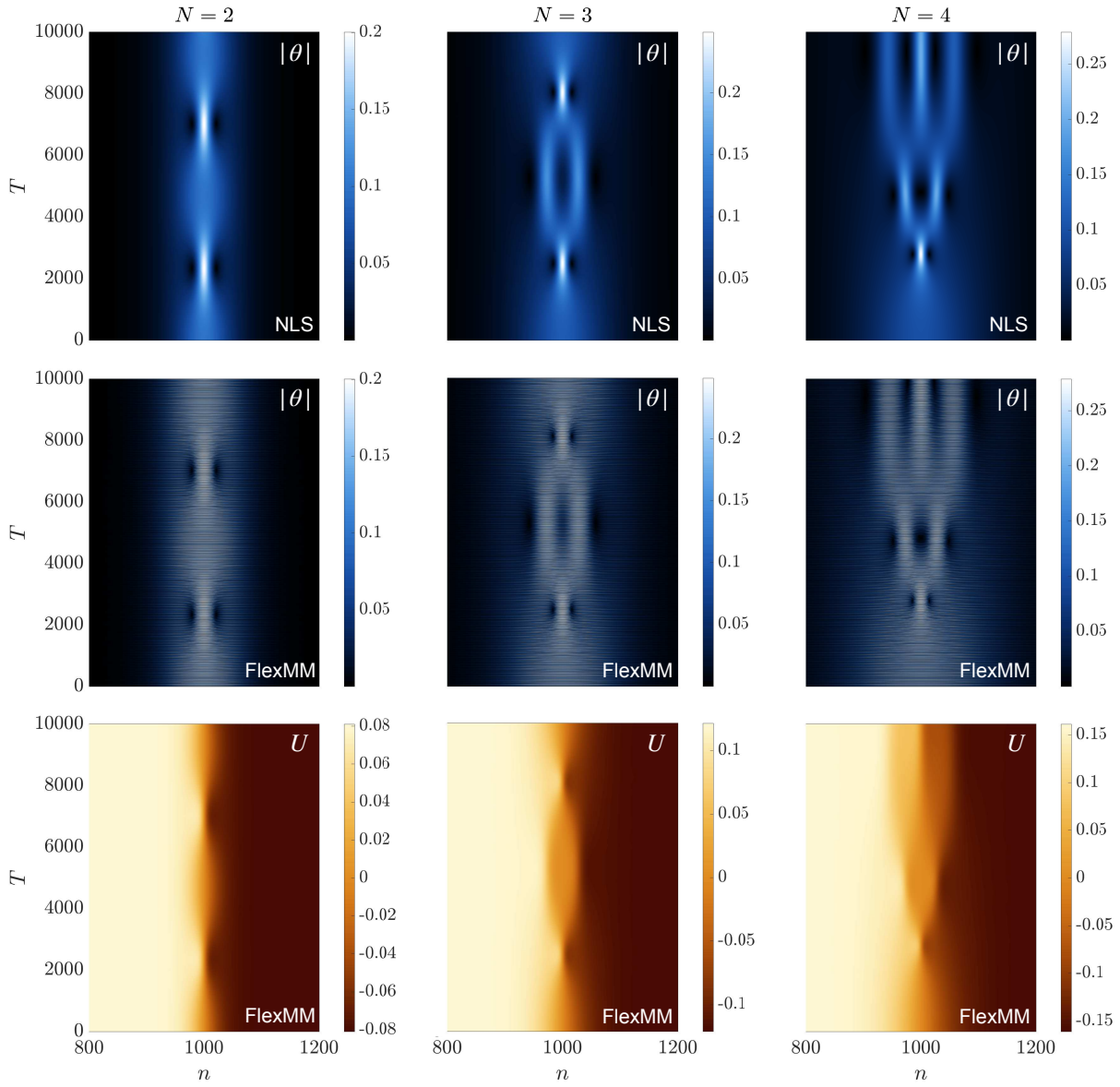

Figure 5.2: Numerical solutions of the NLS equation in the first line and of the FlexMM in the second one, for the rotational motion θ, and in the third lines for the longitudinal displacement U. Each column corresponds to simulations for a specific number of solitons $N = \{2, 3, 4\}$.

Fig. 5.2. Concerning the NLSE, this solution consists of the nonlinear superposition of two fundamental, non-traveling solitons. Together, they form a bound state that results in a breathing solution characterized by a temporally-periodic evolution. Concerning the FlexMM discrete lattice model, we observe that the envelope of the θ component follows the NLS equation evolution with great accuracy. In addition, due to the nonlinear coupling with the U component, one can observe a corresponding pattern in the evolution of the longitudinal motion that follows (is driven by) the rotational motion.

Similarly, for higher order solitons, for example, $N = 3$ and $(N = 4)$, the emergence of localized breathing structures is induced by the interaction of three (four) bright solitons as shown in the second (third) column of Fig. 5.2. Once again, the FlexMM discrete evolution is in good agreement with what the NLSE predicts.

5.5.3. Gradient catastrophe in FlexMM

As noted in Sec. 5.4, the gradient catastrophe phenomenon is regularized by the local emergence (at $T = T_m$) of a Peregrine soliton as an asymptotic solution of the focusing NLS equation. This property is verified in Fig. 5.3.

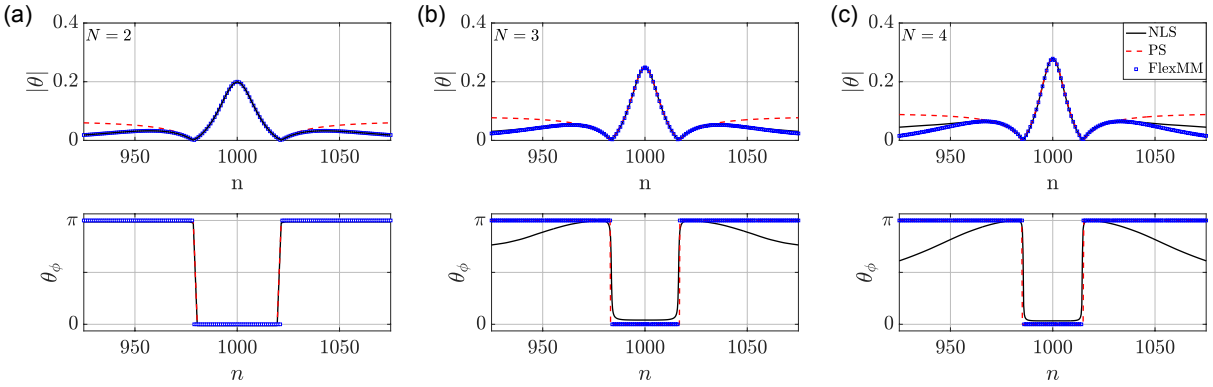

Figure 5.3: Profile and phase of the first localized structure for $N = 2$ in panel (a), for $N = 3$ in panel (b), and $N = 4$ in panel (c) at the maximum compression moment for the FlexMM (blue square) and the NLS equation (black line). For each N, the coherent structure is compared to a scaled PS (red dashed line).

In this figure, the discrete spatial profile at the maximum compression moment for the rotational motion of the FlexMM is plotted (blue squares) and compared to the NLSE prediction (black line). The analytic PS (dashed red line) agrees with the discrete simulations for both the spatial and phase profiles. We note that we determined the PS continuous background a_0, cf. Eq. (5.1), from the maximum amplitude of the rotational component (NLSE simulation). In this case $a_0 = |\theta(X_0, T_m)|/3$.

For a more detailed analysis of the theoretical prediction accuracy, we show the amplitude of the first localized structure in Fig. 5.4(a) and the maximum compression moment in Fig. 5.4(b) for a wide range of N values. For the discrete equations of the FlexMM, N takes values from 2 to 10. For all these values of N, it is clear that FlexMM and the NLS model are in excellent agreement. If for $N = 10$, the numerically calculated value of T_m is close to the theoretical estimation, we observe that the amplitude remains significantly

far from the asymptotic value,

$$\theta_{N\to\infty} = 6\sqrt{2}\epsilon A_0. \tag{5.23}$$

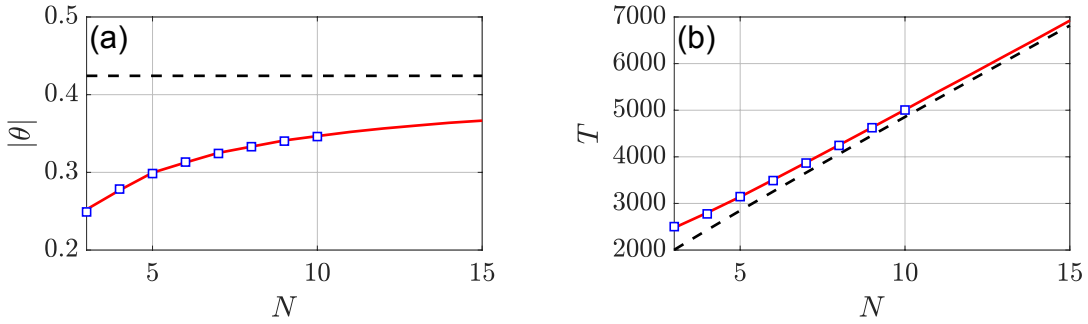

Figure 5.4: Numerical simulations displaying the maximum amplitude (a) of the rotational evolution at the compression moment (b) as a function of N. The black dashed line represents the theoretical predictions from Eqs. (5.23-5.13). The red line represents the simulation results using the NLS equation, and the blue squares represent those of the FlexMM.

Fig. 5.5 represents the dynamic evolution of the NLS equation (a) and of the discrete FlexMM equation (b-c) for $N = 10$ in more detail. The spatial profiles of $|\theta|$ (d) and U (e) are represented at the maximum compression point. From the $|\theta|$ profile of the NLS model shown in panel (d), we can predict the profile of the first-order term of the longitudinal displacement, G_0, using Eq. (5.7a). This prediction is represented by the black line in panel (e). The excellent match between the predicted and actual FlexMM profiles demonstrates the effectiveness of the NLS model in accurately describing the envelope dynamics of the FlexMM.

5.6. Conclusions

In this last chapter, we have introduced a mathematical concept developed by A. Tovbis and M. Bertola, called gradient catastrophe. It has been proven that this phenomenon can lead to the generation of the rational Peregrine Soliton as a local asymptotic solution of the NLSE. Based on the theoretical model introduced in Chap. 4, we have proven that the propagation of sufficiently large initial modulated waves in FlexMMs can lead to the emergence of the gradient catastrophe phenomenon. An interesting future direction is to study if the manifestation of the gradient catastrophe could be used as a dynamical trigger of transition waves in bistable mechanical structures like the ones already studied in the literature [32, 162]. For preliminary results following this line, see the Chap. 6.

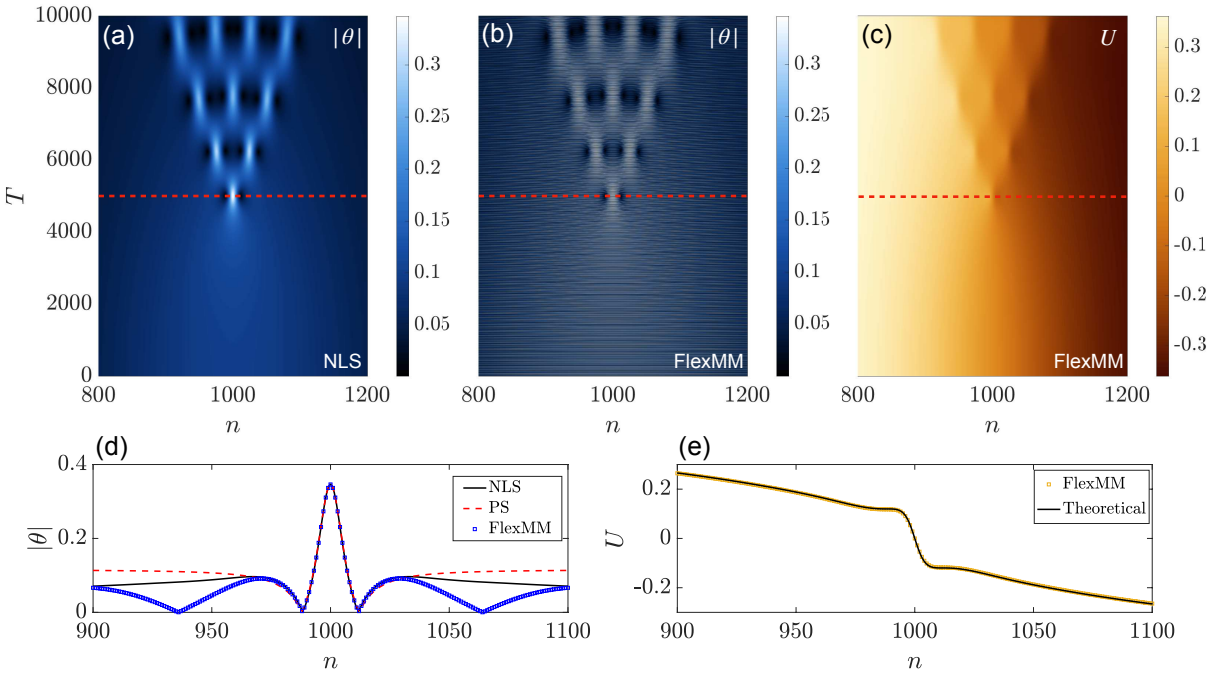

Figure 5.5: Numerical simulations of Eq. (5.8) in panel (a) and Eq. (5.1) in panels (b-c) for an initial pulse with $N = 10$. Panel (d) represents the absolute value of the rotational profile of the dynamics displayed in (a) and (b) at the maximum compression moment where the scaled PS is superimposed for comparison. In panel (e), the longitudinal displacement is compared to the theoretical profile obtained using Eq. (5.7a). This prediction is calculated by substituting the rotational field, computed with the NLS equation, into Eq. (5.7a).

6 | General conclusion and perspectives

The presented PhD work has been dedicated to the theoretical and numerical investigation of propagating modulated waves in nonlinear flexible metamaterials (FlexMMs). These structures, whose unique properties arise from the geometric nonlinearity and the multiple degrees of freedom of the structures, offer a rich platform for exploring various nonlinear wave phenomena.

Chapter 2 laid the groundwork for essential analytical and numerical tools. Those were first applied to a simpler system: the simplified rotating-square structure where the motion equation reduces to a nonlinear Klein-Gordon equation with cubic nonlinearity. Applying multiple scales perturbation, the transition to the nonlinear Schrödinger equation (NLSE) was highlighted. This methodology is of fundamental importance and sets the stage for understanding the more complex case of FlexMMs with two DOFs.

Building on this base, chapter 3 explored the modulation instability (MI) phenomenon in FlexMMs. The stability of these waves was examined by deriving an NLS equation for slowly varying envelope waves from a discrete, nonlinear lump model. The analysis revealed that the interplay between the rotational and longitudinal DOFs can stabilize regions that would otherwise be unstable. A natural extension of this work includes the initial excitation of both the rotational and longitudinal modulated waves, leading to a coupled NLS equation with much richer MI dynamics.

Chapter 4 extended the approach and the methodology to account for discrete effects and localized modulated waves. As an outcome, the existence and propagation of bright and dark envelope vector solitons were analyzed in detail. The rotational DOF was found to be described by an extended NLS equation (compared to the one in chapter 3). The longitudinal one followed the dynamics induced by a nonlinear coupling. These solutions constitute novel nonlinear wave solutions under vectorial form. Future investigations could take advantage of the multiple DOFs to seek other types of vector solitons in FlexMMs which would be described by a multiple-component NLS equation.

Finally, in chapter 5, the concept of gradient catastrophe was introduced, as developed by A. Tovbis and M. Bertola [156]. We demonstrated that the propagation of sufficiently large initial modulated plane waves in FlexMMs could lead to the generation of an assembly of localized coherent structures. The first emerging structure is locally asymptotic to a Peregrine soliton, a solution of the effective NLS equation theoretically predicted in chapter 4.

In a nutshell, this thesis has shown the significant potential of nonlinear FlexMMs for observing and controlling both typical and novel nonlinear phenomena related to modulated waves. Future research will focus on the experimental validation and the modeling of dissipative effects. These efforts will further enhance our understanding of nonlinear wave dynamics in soft mechanical metamaterials, paving the way for innovative developments and applications in this field. The two very last sections present the preliminary results following the line of setting up experiments and exploring gradient catastrophe in bistable systems to trigger transition waves.

Towards Experiments: Experimental setup

Several steps must be taken to prepare for future experimental validation of the findings in this thesis. These include exciting the system by applying driving functions to one end of the chain and adding dissipation to the system. Additionally, the third degree of freedom, namely the transverse displacement, could also be considered if needed. Some work has already been pursued in that way, particularly in Xinxin Guo's PhD thesis prepared at LAUM and defended in 2018 [8]. In this work, the system of equations of a structure consisting of N and M columns of rigid particles was determined, taking into account the third degree of freedom. The influence of the static angle (i.e. the initial orientation of the particles) on the linear propagation properties of the global structure also was considered.

Preliminary results using numerical simulations of lumped element equations similar to the ones used in the text core are shown in Fig. 6.1(a). Here, one can observe the propagation of a damped bright soliton within the FlexMM, generated by a driver at one extremity of the chain. Here, a simple linear viscous damping, proportional to the velocity of the particles, has been used. Losses in the system lead to an exponential decrease in the amplitude of the soliton. Moreover, decay causes the solution to spread out.

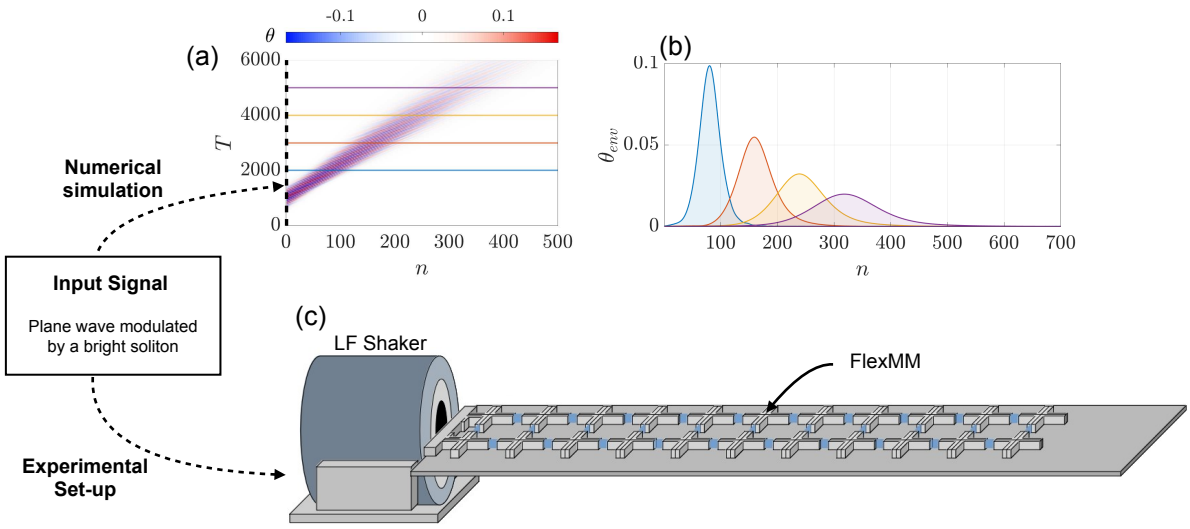

Figure 6.1: (a) Evolution of the θ component of a bright envelope vector soliton with linear viscous damping propagating in the FlexMM. (b) Profile of the BEVS envelope at different moments. The system is excited using a driving function on the left extremity of the chain. (c) The input signal could be applied experimentally with a low-frequency (LF) shaker.

Gradient-catastrophe induced transition waves: preliminary results

Bistable (multistable) systems can be observed both in natural and engineered materials. Due to the existence of two (multiple) stable states, these systems exhibit a rich phenomenology including structural phase transitions, the existence of domain walls, and more.

For mechanical structures, this property makes them valuable in various applications such as energy harvesting, mechanical switches, and adaptive materials. Due to the potential barrier, transitioning to the other stable state requires a critical amount of

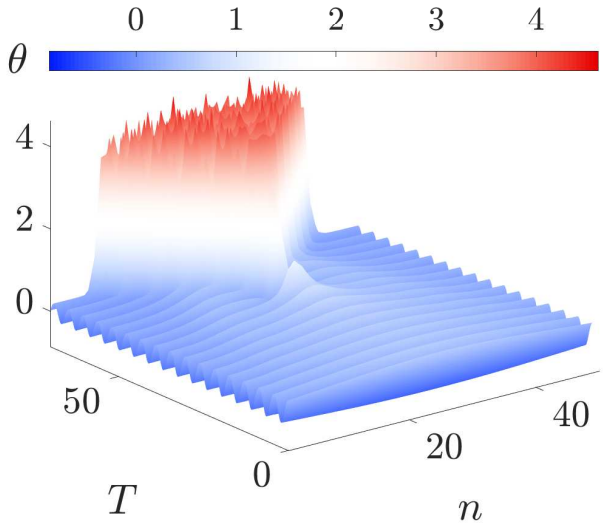

Figure 6.2: Evolution of the bistable system. At $T = 50$ the transition wave is generated by the emergence of a local coherent structure.

energy. After reaching the required energy level, a transition wave can propagate through the structure, allowing each site in the system to move from stable state 1 (blue) to stable state 2 (red), as visible in Fig. 6.2.

Transition waves are typically generated at one end of the structure by a quasi-static displacement or an impact. Our ability to control the regularization of the gradient catastrophe phenomenon would enable precise control over the timing and location of the transition wave in the structure (i.e. the localization properties of the emerging Peregrine soliton).

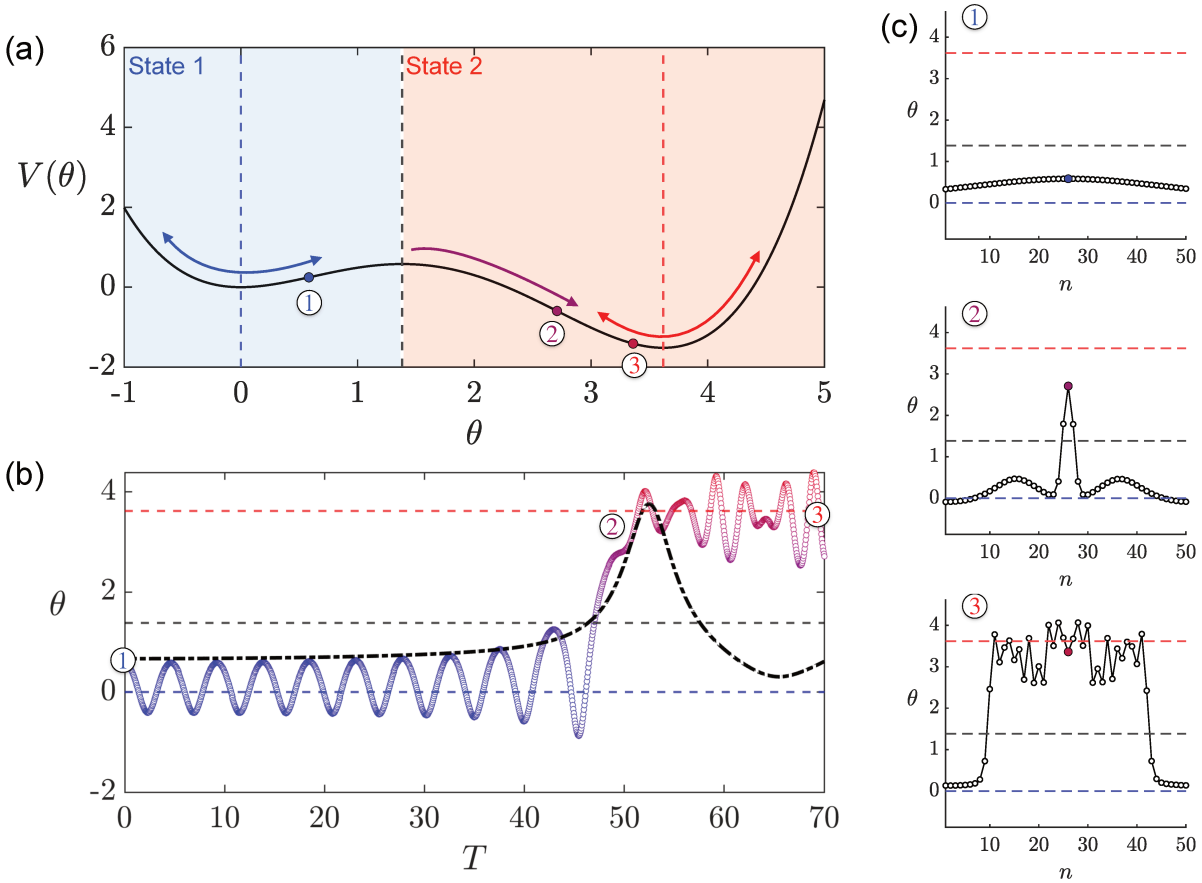

Figure 6.3: Evolution of the $n = 25$ site. At $T = 50$, the transition wave is generated. The black dotted line corresponds to the temporal profile predicted by the NLS equation which locally takes the form of the Peregrine soliton.

In this preliminary investigation, we study a mathematical model characterized by a discrete nonlinear cubic Klein-Gordon (KG) equation with an on-site asymmetric bistable potential of the form θ_n^4 [131][162] with n the site number. Following the procedure described in Chap. 5, we can determine the coefficients P and Q of the effective NLS equation of the bistable system. These coefficients allow us to establish the initial conditions nec-

essary to generate and characterize the gradient catastrophe phenomenon. In Fig. 6.3(c), the nonlinear dynamics of the bistable structure are illustrated at three different moments. The first one describes the case in which the discrete points are trapped in the potential well corresponding to stable state 1. In the second panel, the regularization of the gradient catastrophe occurs, resulting in the emergence of a localized structure in space and time. Finally, in the last panel, the transition wave successively moves the points into stable state 2. In Fig. 6.3(b), the NLS model (black dotted line) shows consistency with the dynamics of the discrete model until the transition.

Many questions remain unanswered and need to be explored in greater depth, particularly regarding the energy required for the transition. Up to now, observations have been made on this matter. It appears that a single point crossing the potential barrier is insufficient for a transition, due to interactions with its neighbors. Additionally, the initial phase of the carrier wave seems to influence the amount of required energy.

A | Dispersion relation

The dispersion relation of the metastructure is obtained by linearizing the equations of motion ($\sin\theta \approx \theta$) and assuming that the chain is excited by a harmonic source of pulsation ω, propagating along increasing x. The harmonic solutions of the linear system are represented by the following three vectors when one poses $x_i = ia$, $x_{i\pm1} = (i \pm 1)a$:

$$\begin{aligned}
\vec{\phi}_i &= \begin{bmatrix} U_i \\ \theta_i \end{bmatrix} = \begin{bmatrix} U_0 \\ \theta_0 \end{bmatrix} e^{j(\omega t - q x_i)} = \begin{bmatrix} U_i \\ \theta_i \end{bmatrix}, \\
\vec{\phi}_{i+1} &= \begin{bmatrix} U_{i+1} \\ \theta_{i+1} \end{bmatrix} = \begin{bmatrix} U_0 \\ \theta_0 \end{bmatrix} e^{j(\omega t - q x_{i+1})} = \begin{bmatrix} U_i \\ \theta_i \end{bmatrix} e^{-jqa}, \\
\vec{\phi}_{i-1} &= \begin{bmatrix} U_{i-1} \\ \theta_{i-1} \end{bmatrix} = \begin{bmatrix} U_0 \\ \theta_0 \end{bmatrix} e^{j(\omega t - q x_{i-1})} = \begin{bmatrix} U_i \\ \theta_i \end{bmatrix} e^{+jqa}.
\end{aligned} \tag{A.1}$$

By substituting these harmonic solutions in the linearized equations, we obtain an eigenvalue problem,

$$[M]^{-1}[K]\vec{\phi} = \lambda\vec{\phi}\,, \tag{A.2}$$

with $\lambda = \omega^2$ the eigenvalue and $\vec{\phi} = \begin{bmatrix} U_0 \\ \theta_0 \end{bmatrix}$ the eigenvector, and

$$\begin{aligned}
[M] &= \begin{bmatrix} 1 & 0 \\ 0 & \alpha^{-2} \end{bmatrix}, \\
[K] &= \begin{bmatrix} 2\,(1 - \cos(qa)) & 0 \\ 0 & -2\delta\cos(qa) + 2\,(K_s + 2K_\theta) \end{bmatrix}.
\end{aligned} \tag{A.3}$$

The coupling between modes comes from the anti-diagonal terms of the K matrix. Since every mass unit is aligned at the initial time, these anti-diagonal coefficients are equal to zero. The modes are decoupled.

B | Multiple scales method

The different scales imply that the differentials of X and T must be redefined according to the different scales used X_i and T_i. By defining the notation $D_i = \frac{\partial}{\partial T_i}$ and in an analogous way $D_{iX} = \frac{\partial}{\partial X_i}$, we can write,

$$\begin{aligned}
\frac{\partial^2}{\partial T^2} &= (D_0 + \epsilon D_1 + \epsilon^2 D_2 + ...)^2 \,, \\
&= D_0^2 + 2\epsilon D_0 D_1 + \epsilon^2 (D_1^2 + 2D_0 D_2) + ... \,, \\
\frac{\partial^2}{\partial X^2} &= (D_{0X} + \epsilon D_{1X} + \epsilon^2 D_{2X} + ...)^2 \,, \\
&= D_{0X}^2 + 2\epsilon D_{0X} D_{1X} + \epsilon^2 (D_{1X}^2 + 2D_{0X} D_{2X}) + ... \,.
\end{aligned} \tag{B.1}$$

The operators $\hat{\mathcal{L}}_j^{(i)}$ and $\hat{\mathcal{M}}_j^{(i)}$ are given by the following expressions:

$$\begin{aligned}
\hat{\mathcal{L}}_0^{(1)} &= D_0^2 - D_{0X}^2 \\
\hat{\mathcal{L}}_0^{(2)} &= D_0^2 - C_1 D_{0X}^2 + C_2 \,, \\
\hat{\mathcal{L}}_1^{(1)} &= 2(D_0 D_1 - D_{0X} D_{1X}) \,, \\
\hat{\mathcal{L}}_1^{(2)} &= 2(D_0 D_1 - C_1 D_{0X} D_{1X}) \,, \\
\hat{\mathcal{L}}_2^{(1)} &= D_1^2 - D_{1X}^2 + 2D_0 D_2 - 2D_{0X} D_{2X} \,, \\
\hat{\mathcal{L}}_2^{(2)} &= D_1^2 - C_1 D_{1X}^2 + 2D_0 D_2 - 2C_1 D_{0X} D_{2X} \,,
\end{aligned} \tag{B.2}$$

$$\begin{aligned}
\hat{\mathcal{M}}_0^{(1)} &= \frac{1}{2} D_{0X} \,, \\
\hat{\mathcal{M}}_0^{(2)} &= -C_4 D_{0X} \,, \\
\hat{\mathcal{M}}_1^{(1)} &= \frac{1}{2} D_{1X} \,, \\
\hat{\mathcal{M}}_1^{(2)} &= -C_4 D_{1X} \,, \\
\hat{\mathcal{M}}^{(3)} &= -C_3 \,.
\end{aligned}$$

C | Parametric study of the PQ product

As mentioned in Sec. 4.3 of the main text, the NLS equation exhibits two different behaviors depending on the sign of the product PQ. In figure C.1, parametric studies are displayed to illustrate the influence of each parameter and the coupling effect between the rotational and longitudinal displacements on the NLS equation. To do this, all parameters are initially set to those used in the Lego® structure for the experiments [7], $\alpha = \alpha_l = 1.815$, $K_s = K_{sl} = 0.01851$, $K_\theta = K_{\theta l} = 1.534\text{e}^{-4}$. The range of examined parameters goes from zero to ten times the initial values.

Figure C.1 shows that the coupling between the two DOFs plays a major role, making the evolution of the sign of PQ as a function of k even more complex (cf. panels (b-d-f)) than when there is only rotation in the system (a-c-e). For example, if the system can only rotate, α (cf. panel (a)) does not affect the sign of PQ. Moreover in the case of panels (c) and (e), K_s and K_θ dependent respectively, the variation of the parameters slightly changes the transition value of k to obtain a focusing or defocusing NLS equation. If we compare each of these studies with its coupled equivalent (cf. (a) to (b), (c) to (d), and (e) to (g)), more transition values (values where PQ change its sign) of k are visible. In conclusion, the behavior of the eNLSE under coupling conditions, between U_n and θ_n, is very sensitive to the design features of the FlexMM.

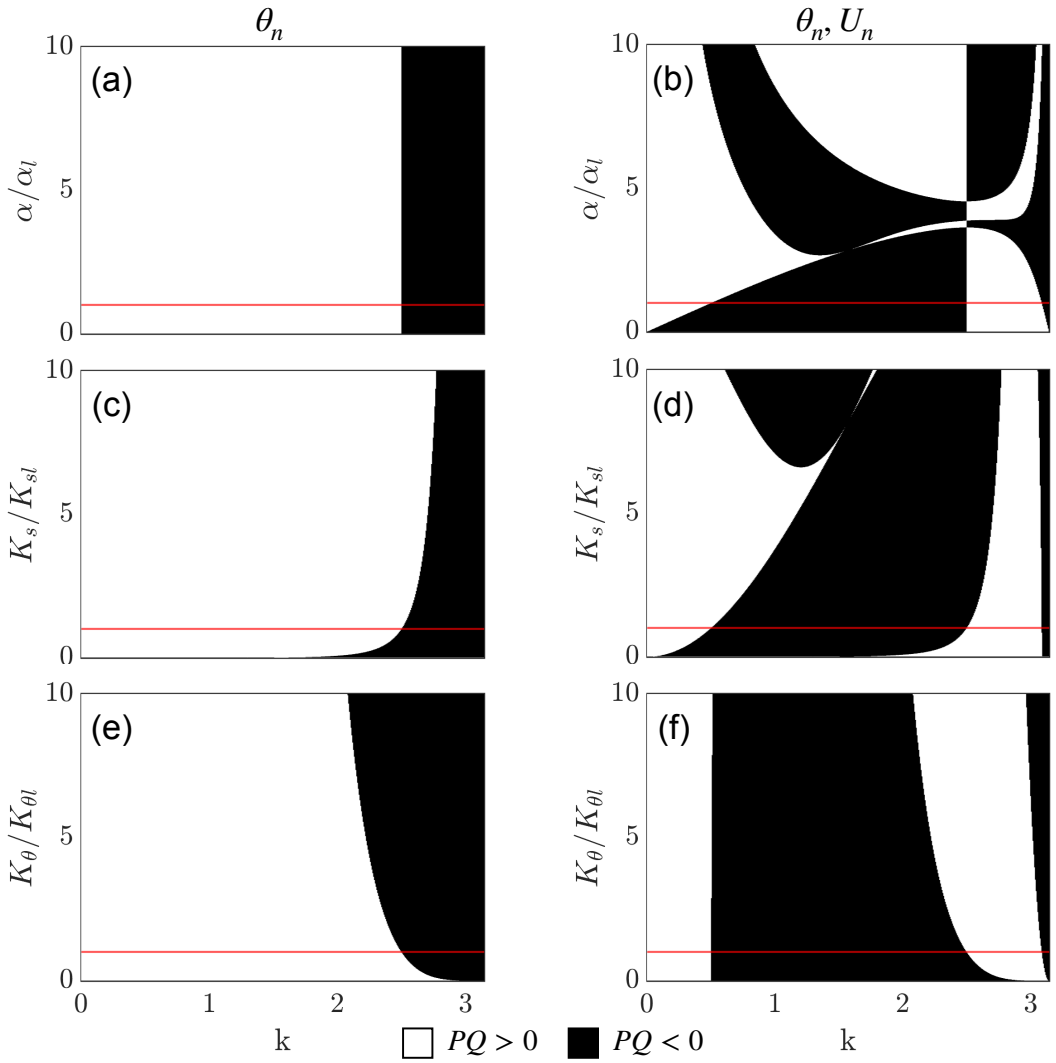

Figure C.1: Sign of PQ as a function of k and: α for panels (a-b), K_s for panels (c-d), and K_θ for panels (e-f). α, K_s, and K_θ are normalized by $\alpha_l, K_{sl}, K_{\theta l}$ respectively, the physical parameters used in the Lego® structure for experiments. The horizontal red line for each panel represents 1, that is when $\alpha = \alpha_l$, $K_s = K_{sl}$, $K_\theta = K_{\theta l}$. Finally, the first column (a, c, e) corresponds to a configuration where particles can only rotate while in the second column (b, d, f), particles both can rotate and translate.

D | Defocusing nonlinearity, propagation of a modulated wave in the lattice

In section 4.4 of the main text, the global nonlinear dynamic response of the structure (see Figs. (4.4-4.7)) and its dynamics only at the final time (see Fig. 4.5) are presented, generated by an initial excitation of the bright soliton solution in the case of a focusing eNLS equation. As a result, a lattice BEVS propagates throughout the structure.

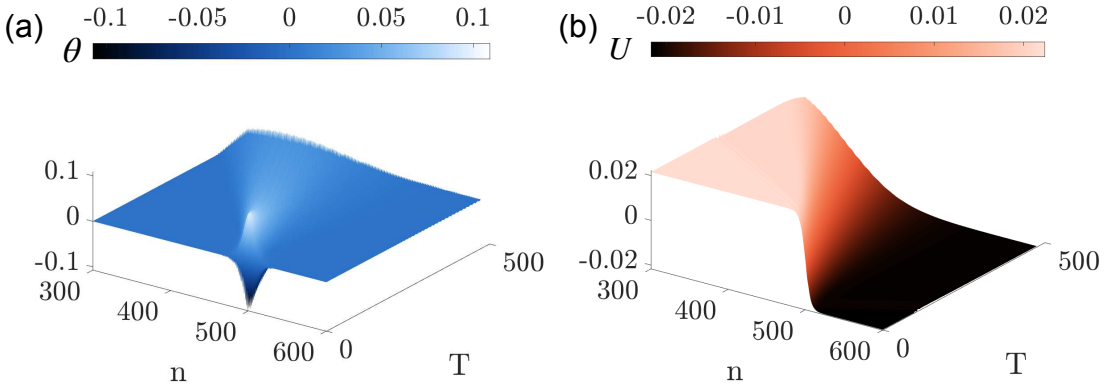

Figure D.1: Evolution in time (T) of the amplitudes of the rotational (a) and longitudinal displacements (b) along the chain (n). The results correspond to a flexMM defined by the following set of parameters: $\alpha = 1.815$, $K_s = 0.1851$, $K_\theta = 1.534\text{e}^{-2}$. The solution is generated by the initial conditions expressed in Eqs. (4.30-4.31) for the spatial frequency $k = 2.8274$, an amplitude $A = 15$, and a perturbation $\epsilon = 0.01$.

For a more general study, it is interesting to use this initial condition in a wisely chosen wave number range to obtain a defocusing NLS equation, highlighted with the black areas in Fig. 4.3 (a). A defocusing NLS equation is obtained when the product of the dispersive and nonlinear coefficients is negative $PQ < 0$. To use the ICs expressed by Eqs. (4.30-4.31), we have to put an absolute value to P and Q. As expected in Fig. D.1, the defocusing property of the eNLS equation, and thus of the propagation medium, leads to a time spreading of the wave packets.

E | Exponential time difference fourth-order Runge-Kutta scheme

In this appendix, we present the exponential time difference fourth-order Runge-Kutta (ETDRK4) scheme used in chapter 5 to solve the NLS equation.

This method was developed by Cox and Matthews in 2002 [160] and improved by Kassam and Trefethen in 2005 [161]. ETDRK-based methods are powerful integration schemes that provide a robust, accurate, and efficient solution for stiff differential equations by exactly handling the linear terms and approximating an integral involving the nonlinear terms, see Eq. (E.7). It combines the strengths of exponential integrators and Runge-Kutta methods (in our case of 4th order).

For this method, we shall split the PDE into its linear and nonlinear parts,

$$u_t = \mathcal{L}u + \mathcal{N}(u,t)\,, \tag{E.1}$$

where $\mathcal{L}$ is linear and $\mathcal{N}(u,t)$ nonlinear. Once the spatial part of the PDE is discretized, Eq. (E.1) resulting in a system of ODEs,

$$u_t = \mathbf{L}u + \mathbf{N}(u,t)\,. \tag{E.2}$$

The concept of the ETD methods is similar to the method of the integrating factor [163]. The idea is to multiply both sides of Eq. (E.2) by an integrating factor,

$$e^{-\mathbf{L}t}u_t = e^{-\mathbf{L}t}\mathbf{L}u + e^{-\mathbf{L}t}\mathbf{N}(u,t)\,. \tag{E.3}$$

By a relevant change of variable,

$$v = ue^{-\mathbf{L}t}\,, \tag{E.4}$$

Eq. (E.3) becomes,

$$v_t = e^{-\mathbf{L}t}\mathbf{N}(ve^{\mathbf{L}t})dt\,. \tag{E.5}$$

This clever change of variable allows us to exactly solve the linear part on the left side of Eq. (E.5). Integrating the equation over a single time step h from $t = t_n$ to $t_{n+1} = t_n + h$, we get,

$$\begin{aligned} \int_{t_n}^{t_n+h} \frac{d}{dt}\left(e^{-\mathbf{L}t}u\right)dt &= \int_{t_n}^{t_n+h} e^{-\mathbf{L}t}\mathbf{N}(u)dt\,, \\ e^{-\mathbf{L}(t_n+h)}u_{n+1} - e^{-\mathbf{L}t_n}u_n &= \int_{t_n}^{t_n+h} e^{-\mathbf{L}t}\mathbf{N}(u)dt\,. \end{aligned} \tag{E.6}$$

Finally, the solution of Eq. (E.1) at $t = t_{n+1}$ can be computed exactly using the following equation,

$$u_{n+1} = e^{\mathbf{L}h}u_n + e^{\mathbf{L}h}\int_0^h e^{-\mathbf{L}\tau}\mathbf{N}(u(t_n+\tau), t_n+\tau)d\tau\,, \tag{E.7}$$

where $\tau = t - t_n$. As mentioned, up to now, Eq. (E.7) is exact. However, the integral must be approximated using an ETD numerical scheme of the chosen order. To approximate the integral, Cox and Matthews developed a recurrence relation that provides an algorithm based on the Runge-Kutta time-stepping scheme for various orders of approximations.

Here are the formulae for the 4th-order Runge-Kutta scheme,

$$a_n = e^{\mathbf{L}h/2}u_n + \mathbf{L}^{-1}\left(e^{\mathbf{L}h/2} - \mathbf{I}\right)\mathbf{N}(u_n, t_n)\,, \tag{E.8a}$$

$$b_n = e^{\mathbf{L}h/2}u_n + \mathbf{L}^{-1}\left(e^{\mathbf{L}h/2} - \mathbf{I}\right)\mathbf{N}(a_n, t_n + h/2)\,, \tag{E.8b}$$

$$c_n = e^{\mathbf{L}h/2}a_n + \mathbf{L}^{-1}\left(e^{\mathbf{L}h/2} - \mathbf{I}\right)\left(2\mathbf{N}(b_n, t_n + h/2) - \mathbf{N}(u_n, t_n)\right)\,, \tag{E.8c}$$

$$\begin{aligned} u_{n+1} = {} & e^{\mathbf{L}h/2}u_n + \alpha\mathbf{N}(u_n, t_n) + 2\beta\left[\mathbf{N}(a_n, t_n + h/2) + \mathbf{N}(b_n, t_n + h/2)\right] \\ & + \gamma\mathbf{N}(c_n, t_n + h)\,, \end{aligned} \tag{E.8d}$$

with $\mathbf{I}$ the identity matrix and α, β, and γ defined as,

$$\alpha = h^{-2}\mathbf{L}^{-3}\left[-4 - \mathbf{L}h + e^{\mathbf{L}h}(4 - 3\mathbf{L}h + (\mathbf{L}h)^2)\right]\,, \tag{E.9a}$$

$$\beta = h^{-2}\mathbf{L}^{-3}\left[2 + \mathbf{L}h + e^{\mathbf{L}h}(-2 + \mathbf{L}h)\right]\,, \tag{E.9b}$$

$$\gamma = h^{-2}\mathbf{L}^{-3}\left[-4 - 3\mathbf{L}h - (\mathbf{L}h)^2 + e^{\mathbf{L}h}(4 - \mathbf{L}h)\right]\,. \tag{E.9c}$$

These constants depend on the linear operator L and the time step h and can be computed before the time-stepping of the Runge-Kutta scheme.

For the following NLS equation,

$$i\frac{\partial u}{\partial t} + \frac{1}{2}\frac{\partial^2 u}{\partial x^2} + |u|^2 u = 0, \tag{E.10}$$

we discretize the spatial domain using a Fourier spectral method. Translating Eq. (E.10) to the Fourier space gives,

$$\hat{u}_t = -0.5ik^2\hat{u} - i\widehat{|u|^2 u}\,. \tag{E.11}$$

In form of Eq. (E.2), we obtain the following operators,

$$\mathbf{L}\hat{u}(k) = \mathbf{L}\mathcal{F}(u) = -0.5ik^2\mathcal{F}(u)\,, \tag{E.12a}$$

$$\mathbf{N}(\hat{u}(k), t) = \mathbf{N}(\mathcal{F}(u), t) = -i\mathcal{F}\left(|\mathcal{F}^{-1}(\mathcal{F}(u))|^2\mathcal{F}^{-1}(\mathcal{F}(u))\right)\,, \tag{E.12b}$$

where $\mathcal{F}$ is the discrete Fourier transform.

F | List of scientific publications, communications and activities during the PhD thesis work

F.1. Scientific publications

- **A. Demiquel**, V. Achilleos, G. Theocharis, V. Tournat, Modulation instability in nonlinear flexible mechanical metamaterials, Physical Review E **107**, 054212 (2023),
- **A. Demiquel**, V. Achilleos, G. Theocharis, V. Tournat, Envelope vector solitons in nonlinear flexible mechanical metamaterials, Wave Motion **131**, 103394 (2024).
- **A. Demiquel**, V. Achilleos, G. Theocharis, V. Tournat, Gradient catastrophe and Peregrine soliton in nonlinear flexible mechanical metamaterials, in preparation.

F.2. Conferences and training schools

(O) Oral presentation, **(P)** Poster session, **(T)** Training School, **(A)** Attendee

- **(O) A. Demiquel**, V. Achilleos, G. Theocharis, V. Tournat, "Génération d'instabilités modulationnelles dans des Métamatériaux Elastiques Flexibles Architecturés", 16ème Congrès Français d'Acoustique (CFA), Marseille, France, April 11th - 15th 2022,
- **(O) A. Demiquel**, V. Achilleos, G. Theocharis, V. Tournat, "Instabilités modulationnelles dans des Métamatériaux Elastiques Flexibles", Seminar ED SPI for the second year PhD student, Vannes, France, June 30th - July 1st 2022,
- **(O) A. Demiquel**, V. Achilleos, G. Theocharis, V. Tournat, "Generation of Modulational Instabilities in an Architectural Flexible Elastic Metamaterial", SIAM Conference on Nonlinear Waves and Coherent Structures (NWCS22), Bremen, Germany, August 30th - September 2nd 2022,

- **(O) A. Demiquel**, V. Achilleos, G. Theocharis, V. Tournat, " Generation of modulational instabilities in a flexible elastic metamaterial", 3rd edition of SAM Symposium on Acoustic Metamaterials, Nîmes, France, October 19th-21th 2022,
- **(P) A. Demiquel**, F. Allein, A. Anastasiadis, R. Chaunsali, I. Frankel, N. Boechler, F. Diakonos, V. Tournat, V. Achilleos, **G. Theocharis**, "Mechanical Metamaterials: from topological edge states to rogue waves", La 26ème rencontre du non linéaire (RNL), Paris, France, March 28th - 30th 2023,
- **(T)** Training School on Acoustic & Elastic (Meta)-Materials, UPV Valencia, Spain, November 13th-17th 2024,
- **(P) A. Demiquel**, V. Achilleos, G. Theocharis, V. Tournat, "Envelope vector solitons in nonlinear flexible mechanical metamaterials", La 27ème rencontre du non linéaire (RNL), Paris, France, March 18th - 20th 2024,
- **(A)** 4th edition of SAM Symposium on Acoustic Metamaterials, Aegina, Greece, May 15th-18th 2024,
- **(O) A. Demiquel**, V. Achilleos, G. Theocharis, V. Tournat, "Gradient catastrophe and Peregrine soliton in nonlinear flexible mechanical metamaterials", Workshop DynaMetaFlex Kick-off meeting of the IRP CNRS – Harvard, Le Mans, France, July 3rd-4th 2024.

F.3. Activities

F.3.1. Lectures (160h)

- Mathematics, Mechanics bachelor degree, 3rd year (40 hours)
- Vibrations practicals, Acoustics bachelor degree, 2nd year (30 hours).
- Acoustics practicals, Acoustics bachelor degree, 2nd year (60 hours),
- Mathematics and Vibrations, Mechanics master degree, 1st year (30 hours).

F.3.2. Student project: "La biennale du son, Le Mans Sonore 2022 "

Analytical, numerical, and experimental characterization of a spring-coupled pendulum chain: linear waves and solitons, by Hubert Coste and Tristan Nerson (3rd year bachelor's degree in acoustics and vibrations), co-supervised with Nicolas Pajusco.

In the context of the biennial event Le Mans Sonore 2022, the Laboratoire d'Acoustique de l'Université du Mans (LAUM) and the RAmDAM association decided to create a mainstream event to showcase acoustic phenomena studied in the laboratory. To achieve this goal of scientific mediation, a spring-coupled pendulum chain was built. By comparing the analytical model that describes the dynamics of the system with numerical simulations and experimental results, the accuracy of the theoretical model is discussed, particularly about whether the pendulums should be considered as point masses.

In this project, the linear and nonlinear regimes of the system were studied experimentally. To estimate the chain parameters, the dispersion relation of the system was determined. In addition, different solutions of the sine-Gordon equation in the nonlinear regime, including kink, anti-kink, and breather solutions, were observed. For more information, a video on the project (in French) is available on YouTube [62].

F.3.3. PhD break for 4 months in the University of Ioannina (Epirus, Greece)

Thanks to a mobility grant from the IAGS (Institut d'Acoustique Graduate School, Le Mans Université), I had the opportunity to stay at the Department of Mathematics of the University of Ioannina from April to August 2023. During this period, I collaborated with Prof. Theodoros Horikis on the properties of nonlinear evolution equations applied to various physical settings, including nonlinear optics and water waves. Specifically, we worked on the Exponential Time Differencing methods (ETDRK4), which we applied to the KdV equation to study the undular bore effect in shallow water.

This research experience was enriching from a human and scientific point of view. It gave me valuable insights into advanced numerical methods and their applications. Additionally, the break allowed me to take a step back from my PhD topic, offering a fresh perspective and new ideas for my ongoing research. Finally, the time spent at the University of Ioannina not only advanced my understanding of nonlinear dynamics but also extended my professional network, and my cultural experiences and gave me the chance to meet great people. Many thanks for these memories!

G | Extended abstract (in french)

Dans cette thèse, nous nous intéressons à la propagation d'ondes modulées non linéaires dans des métamatériaux mécaniques flexibles à éléments rotatifs (FlexMM). Avant cela, il a été démontré et observé que des solitons vecteurs pulsés pouvaient être générés dans ces structures, et présentent un lien étroit avec l'équation non linéaire de Klein-Gordon. Le champ de déplacement rotationnel θ est modélisé par cette équation dans la limite continue. Ces études sur les solitons vecteurs pulsés constituent la base de notre investigation, car elles démontrent une connexion entre l'équation non linéaire de Klein-Gordon et les équations du mouvement de nos FlexMM où chaque élément peuvent, en plus de pivoter localement, se déplacer suivant un mode de traction-compression longitudinal U. De plus, puisqu'il est établi que l'équation de Schrödinger non linéaire (NLS) peut décrire l'enveloppe d'une onde se propageant dans l'équation non linéaire de Klein-Gordon, nous pouvons anticiper l'observation de phénomènes spécifiques à l'équation NLS dans les FlexMM, tels que les instabilités modulationelles, les solitons "brights/ darks/breathers", etc., dans le régime faiblement non linéaire et dispersif.

Cette thèse est motivée par l'amélioration des connaissances sur les propriétés dynamiques mécaniques non linéaires des FlexMMs, ce qui augmenterait leur potentiel d'application, notamment dans les dispositifs discrets soumis à des vibrations continues. De plus, les FlexMM offrent une plateforme prometteuse pour étudier de nouveaux phénomènes et explorer des événements extrêmes (abordés dans le chapitre 5 et dans les perspectives) à l'aide d'ondes non linéaires modulées continues.

Dans le premier chapitre de cette thèse sont introduites les notions de métamateriau et de soliton. Au cours des deux dernières décennies, les structures mécaniques architecturées, également connues sous le nom de métamatériaux, ont joué un rôle prédominant dans les avancées scientifiques effectuées dans le domaine de la physique des ondes. Dans ce contexte, les métamatériaux désignent des structures composites synthétiques offrant un contrôle sur la dispersion de différents types d'ondes (optiques, thermiques, acoustiques, vibrations mécanique, etc.). Certains comportements insoupçonnés ont ainsi pu être observés pour toujours mieux contrôler les ondes. Le fait que ces matériaux puissent

manipuler les ondes d'une manière que les matériaux naturels ne le peuvent, a conduit à des innovations dans divers domaines. Par exemple, en optique, des métamatériaux appelés cristaux photoniques sont utilisés pour créer des dispositifs tels que des superlentilles ou des capes d'invisibilité. Dans le domaine de l'acoustique et des vibrations, il existe une très grande variété de métamatériaux qui visent généralement à isoler des vibrations, pour de la réduction de bruit ou du guidage d'onde, etc..., avec différentes astuces de fabrication et de conception.

Pour ces travaux de thèse nous nous intéressons à une classe de métamateriaux mécaniques, à savoir les métamateriaux mecaniques flexibles (FlexMM). Ce sont des structures composées d'éléments rigides et souples, qui une fois reliés forment un réseau périodique de cellules unitaires qui peuvent se déplacer de manière continue les unes par rapport aux autres. Leurs propriétés dynamiques innovantes proviennent de la géométrie de la structure et non de ses propriétés intrinsèques (composition chimique, structure atomique...). Chaque cellule peut se déformer, tourner, fléchir, se plier et se rompre sous l'effet de contraintes mécaniques, et est conçue pour que les cellules adjacentes du réseau puissent interagir, produisant ainsi un comportement collectif souhaité. L'architecture microstructurale confère à la structure globale des propriétés uniques et souvent avancées, telles que la morphing de forme, la protection topologique et des réponses non linéaires.

Le chapitre 2 présente les méthodes analytiques et numériques utilisées dans les chapitres suivants pour étudier la propagation d'ondes modulées dans les FlexMMs. Nous introduisons une version simplifiée de notre chaîne FlexMM, inspirée de plusieurs travaux, où l'équation du mouvement se réduit à une équation de Klein-Gordon non linéaire continue dans la limite continue. Enfin, nous démontrons comment cette équation mène à une équation de Schrödinger non linéaire, qui décrit l'enveloppe du train d'ondes. La solution du soliton "bright" de l'équation NLS est particulièrement étudiée comme exemple.

Dans le chapitre 3, l'objectif principal est d'étudier le phénomène non linéaire d'instabilité modulationnelle (MI) dans les FlexMM. L'étude des MI vise à examiner l'évolution non linéaire des ondes planes modulées. Cette connaissance fondamentale est cruciale pour faire progresser les applications pratiques telles que l'amortissement des vibrations et la récolte d'énergie, où les signaux périodiques sont couramment rencontrés. En partant d'un modèle non linéaire par éléments discrets qui décrit avec précision la dynamique des FlexMM, nous dérivons une équation NLS pour l'enveloppe lentement variable des ondes dans le degré de liberté en rotation. Nous analysons ensuite les conditions sous lesquelles l'instabilité modulationnelle des ondes planes se manifeste suite à une perturbation aléatoire de l'amplitude de l'onde. Enfin, les prédictions théoriques sont comparées à des simulations numériques du modèle discret non linéaire complet, démontrant com-

ment le couplage entre les degrés de liberté des particules et les paramètres mécaniques du métamatériau peuvent induire des instabilités modulationnelles.

Le chapitre 4 est consacré aux solutions solitons de l'équation NLS : les solitons "bright" et "dark". Dans le contexte des FlexMM, il s'agit de solitons-vecteurs enveloppe. Nous présentons le modèle non linéaire par éléments discrets, qui s'est révélé pertinent pour décrire les équations dynamiques des FlexMM. Par la suite, nous dérivons une équation NLS effective dans l'approximation semi-discrète pour l'enveloppe lentement variable des ondes du degré de liberté en rotation. L'utilisation de l'approximation semi-discrète fournit un modèle valide pour toute longueur d'onde des ondes porteuses, contrairement au développement du chapitre 3. Les sections Sec. 4.4 et Sec. 4.5 étudient l'existence et la dynamique des solitons-vecteurs enveloppe "bright" et "dark".

Dans le chapitre 5, nous explorons la génération d'événements extrêmes dans les FlexMM en nous inspirant du phénomène des vagues scélérates, présent dans les océans. Les vagues scélérates sont des vagues géantes et imprévisibles, bien plus hautes que les vagues environnantes. Elles peuvent apparaître soudainement, atteignant des hauteurs de 20 à 30 mètres. De part leur imprévisibilité, elles sont une menace pour la sécurité des marins ainsi que pour les infrastructures maritimes. Longtemps contestée, leur existence n'a été confirmée qu'à partir de 1995. Ces vagues peuvent se former par divers mécanismes linéaires et non linéaires mais la théorie linéaire ne suffit pas à expliquer leur occurrence. La dynamique des vagues en eau profonde, modélisée par l'équation non linéaire de Schrödinger, offre une meilleure compréhension. De part l'universalité de cette équation en optique ou en mécanique quantique par exemple, de tels phénomènes ont été observés dans d'autres systèmes comme les fibres optiques, les condensats de Bose-Einstein ou encore dans le cadre de cette thèse sur les FlexMMs. Mathématiquement, l'objet utilisé pour décrire une vague scélérate est le soliton de Peregrine, une structure cohérente localisée, qui émerge dans certaines conditions. Il a été récemment démontré, grâce au théorème dévelopé par A. Tovbis et M. Bertola, qu'un phénomène appelé "gradient catastrophe" pouvait engendrer l'apparition de structures cohérentes localisées en espace et en temps. Selon cette théorie, des solitons de Peregrine peuvent émerger localement dans la limite semi-classique de l'équation NLS, c'est-à-dire lorsque la non linéarité est bien plus importante que la dispersion dans le système. En utilisant l'équation NLS effective (eNLS) obtenue au Chapitre 4, nous comparons l'évolution des dynamiques des FlexMM avec celle de l'équation NLS en fonction des conditions initiales utilisées. Dans ce chapitre, nous prouvons que la propagation d'ondes modulées suffisamment larges, nous rapprochant de la limite semi-classique de l'équation non linéaire de Schrödinger dans les FlexMM, conduit à l'émergence de structures localisées à la fois en espace et en temps, très similaires au

soliton de Peregrine.

Enfin, dans le Chapitre 6, les conclusions générales et les principales perspectives du travail présenté sont exposées.

L'une de ces perspectives consiste à discuter des élements à mettre en place pour la validation expérimentale des résultats de cette thèse. Pour préparer la validation expérimentale, plusieurs étapes clés doivent être franchies. Il s'agit notamment d'exciter le système en appliquant des fonctions excitatrices à une extrémité de la chaîne (via l'utilisation d'un pot vibrant par exemple), d'introduire de la dissipation dans le système, et de considérer, éventuellement, le déplacement transversal comme un degré de liberté supplémentaire. Les simulations numériques préliminaires montrent déjà des résultats prometteurs, comme la propagation d'un soliton "bright" amorti au sein du FlexMM, bien que la perte dans le système entraîne une diminution de l'amplitude et un étalement de la solution. Cela ouvre la voie à de nouvelles avancées passionnantes dans ce domaine, en s'appuyant sur les travaux antérieurs et en explorant de nouvelles pistes.

Une autre perspective à ce travail consiste à utiliser les résultats obtenus dans le Chapitre 5 sur un FlexMM bistable. Dans cette étude préliminaire, nous explorons un modèle mathématique basé sur une équation non linéaire discrète de Klein-Gordon avec un potentiel bistable asymétrique de la forme θ_n^4. En suivant la méthode décrite dans le Chapitre 5, nous determinons l'équation non linéaire de Schrödinger effective du système bistable, ce qui nous permet de définir les conditions initiales pour générer et caractériser le phénomène du gradient catastrophe. Les dynamiques non linéaires du système bistable sont illustrées à travers trois étapes distinctes : l'état stable initial dans l'état 1, l'émergence d'une structure localisée suite à la régularisation du gradient catastrophe, puis la transition finale vers un nouvel état stable 2. En utilisant ce procédé, il serait possible à la fois de choisir la position ainsi que le moment auquel se produirait la transition d'un état stable à un autre, au sein de la structure.

References

[1] M. Maldovan. Sound and heat revolutions in phononics. *Nature*, 503(7475):209–217, 2013.

[2] J. Shim, S. Shan, A. Košmrlj, S. H. Kang, E. R. Chen, J. C. Weaver, and K. Bertoldi. Harnessing instabilities for design of soft reconfigurable auxetic/chiral materials. *Soft Matter*, 9(34):8198, 2013.

[3] T. Tachi. Freeform Rigid-Foldable Structure using Bidirectionally Flat-Foldable Planar Quadrilateral Mesh. In C. Ceccato, L. Hesselgren, M. Pauly, H. Pottmann, and J. Wallner, editors, *Advances in Architectural Geometry 2010*, pages 87–102. Springer Vienna, Vienna, 2010.

[4] G. V. Rodrigues, L. M. Fonseca, M. A. Savi, and A. Paiva. Nonlinear dynamics of an adaptive origami-stent system. *International Journal of Mechanical Sciences*, 133:303–318, 2017.

[5] K. Kuribayashi, K. Tsuchiya, Z. You, D. Tomus, M. Umemoto, T. Ito, and M. Sasaki. Self-deployable origami stent grafts as a biomedical application of Ni-rich TiNi shape memory alloy foil. *Materials Science and Engineering: A*, 419(1-2):131–137, 2006.

[6] T. Shyu, F. Damasceno, M. Dodd, A. Lamoureux, L. Xu, M. Shlian, M. Shtein, S. C. Glotzer, and N. A. Kotov. A kirigami approach to engineering elasticity in nanocomposites through patterned defects. *Nature Mater*, 14(8):785–789, 2015.

[7] B. Deng, P. Wang, Q. He, V. Tournat, and K. Bertoldi. Metamaterials with amplitude gaps for elastic solitons. *Nat. Commun.*, 9(1):3410, 2018.

[8] X. Guo. *Nonlinear architected metasurfaces for acoustic wave scattering manipulation.* Acoustics, Université du Maine, 2018. NNT : 2018LEMA1030.

[9] G. Theocharis, O. Richoux, V Romero-García, A. Merkel, and V. Tournat. Limits of slow sound propagation and transparency in lossy, locally resonant periodic structures. *New J. Phys.*, 16(9):093017, 2014.

[10] F. Allein, V. Tournat, V. Gusev, and G. Theocharis. Linear and Nonlinear Elastic Waves in Magnetogranular Chains. *Phys. Rev. Applied*, 13(2):024023, 2020.

[11] V. G. Veselago. The electrodynamics of substances with simultaneously negative values of and. *Usp. fiz. nauk.*, 92(3):517–526, 1967.

[12] J. B. Pendry. Negative Refraction Makes a Perfect Lens. *Phys. Rev. Lett.*, 85(18):3966–3969, 2000.

[13] Z. Liu, H. Lee, Y. Xiong, C. Sun, and X. Zhang. Far-Field Optical Hyperlens Magnifying Sub-Diffraction-Limited Objects. *Science*, 315(5819):1686–1686, 2007.

[14] D. Schurig, J. J. Mock, B. J. Justice, S. A. Cummer, J. B. Pendry, A. F. Starr, and D. R. Smith. Metamaterial Electromagnetic Cloak at Microwave Frequencies. *Science*, 314(5801):977–980, 2006.

[15] W. Cai, U.K. Chettiar, A.V. Kildishev, and V.M. Shalaev. Optical cloaking with metamaterials. *Nature Photon*, 1(4):224–227, 2007.

[16] T. Cui, D. R. Smith, and R. Liu. *Metamaterials, Theory, Design, and applications.* Springer, springer edition, 2010.

[17] P. A. Deymier. *Acoustic metamaterials and phononic crystals*, volume 173. Springer Science \& Business Media, 2013.

[18] B. Liang, X. S. Guo, J. Tu, D. Zhang, and J. C. Cheng. An acoustic rectifier. *Nature Mater*, 9(12):989–992, 2010.

[19] A. Santillán and S.I. Bozhevolnyi. Acoustic transparency and slow sound using detuned acoustic resonators. *Phys. Rev. B*, 84(6):064304, 2011.

[20] V. Romero-García, G. Theocharis, O. Richoux, A. Merkel, V. Tournat, and V. Pagneux. Perfect and broadband acoustic absorption by critically coupled sub-wavelength resonators. *Sci. Rep.*, 6(1):19519, 2016.

[21] R. Martínez-Sala, J. Sancho, J. V. Sánchez, V. Gómez, J. Llinares, and F. Meseguer. Sound attenuation by sculpture. *Nature*, 378(6554):241–241, 1995.

[22] A. Leonard, C. Chong, P. G. Kevrekidis, and C. Daraio. Traveling waves in 2D hexagonal granular crystal lattices. *Granular Matter*, 16(4):531–542, 2014.

[23] L.-Y. Zheng, F. Allein, V. Tournat, V. Gusev, and G. Theocharis. Granular graphene: Direct observation of edge states on zigzag and armchair boundaries. *Phys. Rev. B*, 99(18):184113, 2019.

[24] Z. Liu, X. Zhang, Y. Mao, Y. Y. Zhu, Z. Yang, C. T. Chan, and P. Sheng. Locally Resonant Sonic Materials. *Science*, 289(5485):1734–1736, 2000.

[25] G. Ma and P. Sheng. Acoustic metamaterials: From local resonances to broad horizons. *Sci. Adv.*, 2(2):e1501595, 2016.

[26] S. Chen, Y. Fan, Q. Fu, H. Wu, Y. Jin, J. Zheng, and F. Zhang. A Review of Tunable Acoustic Metamaterials. *Applied Sciences*, 8(9):1480, 2018.

[27] P. K. Tang and W. A. Sirignano. Theory of a generalized Helmholtz resonator. *Journal of Sound and Vibration*, 26(2):247–262, 1973.

[28] V. Romero-García, N. Jiménez, G. Theocharis, V. Achilleos, A. Merkel, O. Richoux, V. Tournat, J.-P. Groby, and V. Pagneux. Design of acoustic metamaterials made of Helmholtz resonators for perfect absorption by using the complex frequency plane. *Comptes Rendus. Physique*, 21(7-8):713–749, 2021.

[29] G. Hu, L. Tang, and X. Cui. On the modelling of membrane-coupled Helmholtz resonator and its application in acoustic metamaterial system. *Mechanical Systems and Signal Processing*, 132:595–608, 2019.

[30] Y. Zhu and B. Assouar. Multifunctional acoustic metasurface based on an array of Helmholtz resonators. *Phys. Rev. B*, 99(17):174109, 2019.

[31] K. Bertoldi, V. Vitelli, J. Christensen, and M. van Hecke. Flexible mechanical metamaterials. *Nat. Rev. Mater.*, 2(11):17066, 2017.

[32] J. R. Raney, N. Nadkarni, C. Daraio, D. M. Kochmann, J. A. Lewis, and K. Bertoldi. Stable propagation of mechanical signals in soft media using stored elastic energy. *Proc. Natl. Acad. Sci. U.S.A.*, 113(35):9722–9727, 2016.

[33] O. R. Bilal, A. Foehr, and C. Daraio. Bistable metamaterial for switching and cascading elastic vibrations. *Proc. Natl. Acad. Sci. U.S.A.*, 114(18):4603–4606, 2017.

[34] L. Jin, R. Khajehtourian, J. Mueller, A. Rafsanjani, V. Tournat, K. Bertoldi, and D. M. Kochmann. Guided transition waves in multistable mechanical metamaterials. *Proc. Natl. Acad. Sci. U.S.A.*, 117(5):2319–2325, 2020.

[35] A. Zareei, B. Deng, and K. Bertoldi. Harnessing transition waves to realize deployable structures. *Proc. Natl. Acad. Sci. U.S.A.*, 117(8):4015–4020, 2020.

[36] J. Köpfler, T. Frenzel, M. Kadic, J. Schmalian, and M. Wegener. Topologically Protected Twist Edge States for a Resonant Mechanical Laser-Beam Scanner. *Phys. Rev. Applied*, 11(3):034059, 2019.

[37] Y. Miyazawa, C. Chen, R. Chaunsali, T. S. Gormley, G. Yin, G. Theocharis, and J. Yang. Topological state transfer in Kresling origami. *Commun. Mater*, 3(1):62, 2022.

[38] F. Allein, A. Anastasiadis, R. Chaunsali, I. Frankel, N. Boechler, F. K. Diakonos, and G. Theocharis. Strain topological metamaterials and revealing hidden topology in higher-order coordinates. *Nat. Commun.*, 14(1):6633, 2023.

[39] B. Deng, J. R. Raney, V. Tournat, and K. Bertoldi. Elastic Vector Solitons in Soft Architected Materials. *Phys. Rev. Lett.*, 118(20):204102, 2017.

[40] Z. Song, X. Wang, C. Lv, Y. An, M. Liang, T. Ma, D. He, Y.-J. Zheng, S.-Q. Huang, H. Yu, and H. Jiang. Kirigami-based stretchable lithium-ion batteries. *Sci. Rep.*, 5(1):10988, 2015.

[41] M. Johnson, Y. Chen, S. Hovet, S. Xu, B. Wood, G. Ren, J. Tokuda, and Z. Tse. Fabricating biomedical origami: a state-of-the-art review. *Int. J. C.A.R.S*, 12(11):2023–2032, 2017.

[42] C. Park, Y. Lee, J. Jang, and M. Han. Origami and Kirigami Structure for Impact Energy Absorption: Its Application to Drone Guards. *Sensors*, 23(4):2150, 2023.

[43] S. Tomita, K. Shimanuki, S. Oyama, H. Nishigaki, Toshiaki Nakagawa, M. Tsutsui, Y. Emura, M. Chino, H. Tanaka, Y. Itou, and K. Umemoto. Transition of deformation modes from bending to auxetic compression in origami-based metamaterials for head protection from impact. *Sci. Rep.*, 13(1):12221, 2023.

[44] J. Ma, H. Dai, M. Shi, L. Yuan, Y. Chen, and Z. You. Quasi-static axial crushing of hexagonal origami crash boxes as energy absorption devices. *Mech. Sci.*, 10(1):133–143, 2019.

[45] S. Babaee, S. Pajovic, A. Rafsanjani, Y. Shi, K. Bertoldi, and G. Traverso. Bioinspired kirigami metasurfaces as assistive shoe grips. *Nat. Biomed. Eng.*, 4(8):778–786, 2020.

[46] A. Rafsanjani, K. Bertoldi, and A. R. Studart. Programming soft robots with flexible mechanical metamaterials. *Sci. Robot.*, 4(29):eaav7874, 2019.

[47] F. Ahmed, M. Waqas, B. Jawed, A. M. Soomro, S. Kumar, A. Hina, U. Khan, K. H. Kim, and K. H. Choi. Decade of bio-inspired soft robots: a review. *Smart Mater. Struct.*, 31(7):073002, 2022.

[48] B. Deng, J. R. Raney, K. Bertoldi, and V. Tournat. Nonlinear waves in flexible mechanical metamaterials. *J. Appl. Phys.*, 130(4):040901, 2021.

[49] H. Yasuda, L. M. Korpas, and J. R. Raney. Transition Waves and Formation of Domain Walls in Multistable Mechanical Metamaterials. *Phys. Rev. Applied*, 13(5):054067, 2020.

[50] C. Mo, J. Singh, J. R. Raney, and P. K. Purohit. Cnoidal wave propagation in an elastic metamaterial. *Phys. Rev. E*, 100(1):013001, 2019.

[51] A. Chabchoub and M. Fink. Time-Reversal Generation of Rogue Waves. *Phys. Rev. Lett.*, 112(12):124101, 2014.

[52] A. Chabchoub, O. Kimmoun, H. Branger, N. Hoffmann, D. Proment, M. Onorato, and N. Akhmediev. Experimental Observation of Dark Solitons on the Surface of Water. *Phys. Rev. Lett.*, 110(12):124101, 2013.

[53] Y. Kivshar and G. Agrawal. *Optical Solitons: From Fibers to Photonic Crystals*. Academic Press, 1 edition, 2003.

[54] Y. Nakamura. Experiments on Ion-Acoustic Solitons in Plasmas Invited Review Article. *IEEE Transactions on Plasma Science*, 10(3):180–195, 1982.

[55] M. Remoissenet. *Waves Called Solitons*. Advanced Texts in Physics. Springer Berlin Heidelberg, Berlin, Heidelberg, 1999.

[56] J. S. Russell. Report on Waves. *Mtg. of the British Assoc. for the Advance. of Science*, 14, 1844.

[57] D. J. Korteweg and G. De Vries. XLI. On the change of form of long waves advancing in a rectangular canal, and on a new type of long stationary waves. *Philosophical magazine*, 91(4-6):1007–1028, 1895.

[58] E. Fermi, P. Pasta, S. Ulam, and M. Tsingou. STUDIES OF THE NONLINEAR PROBLEMS. 1955.

[59] N. J. Zabusky and M. D. Kruskal. Interaction of "Solitons" in a Collisionless Plasma and the Recurrence of Initial States. *Phys. Rev. Lett.*, 15(6):240–243, 1965.

[60] J. K. Perring and T. H. R. Skyrme. A model unified field equation. *Nuclear Physics*, 31:550–555, 1962.

[61] P. J. Caudrey, J. C. Eilbeck, and J. D. Gibbon. The sine-Gordon equation as a model classical field theory. *Nuov. Cim. B.*, 25(2):497–512, 1975.

[62] H. Coste, T. Nerson, N. Pajusco, and A. Demiquel. Présentation de solitons dans une chaîne de pendules (Biennale du son 2022), 2022. `https://www.youtube.com/watch?v=lXLFGMEnyTc`.

[63] V. E. Zakharov. Stability of periodic waves of finite amplitude on the surface of a deep fluid. *J. Appl. Mech. Tec. Phys.*, 9(2):190–194, 1968.

[64] T. Brooke Benjamin and J. E. Feir. The disintegration of wave trains on deep water Part 1. Theory. *J. Fluid Mech.*, 27(3):417–430, 1967.

[65] A. Chabchoub, N. P. Hoffmann, and N. Akhmediev. Rogue Wave Observation in a Water Wave Tank. *Phys. Rev. Lett.*, 106(20):204502, 2011.

[66] E. Kengne, S. T. Chui, and W. M. Liu. Modulational instability criteria for coupled nonlinear transmission lines with dispersive elements. *Phys. Rev. E*, 74(3):036614, 2006.

[67] B. Ghosh and K. P. Das. Modulational instability of electron plasma waves in a cylindrical wave guide. *Plasma Phys. Control. Fusion*, 27(9):969–982, 1985.

[68] J. Zhang, V. Romero-García, G. Theocharis, O. Richoux, V. Achilleos, and D. Frantzeskakis. Dark Solitons in Acoustic Transmission Line Metamaterials. *Applied Sciences*, 8(7):1186, 2018.

[69] B. Deng, Y. Zhang, Q. He, V. Tournat, P. Wang, and K. Bertoldi. Propagation of elastic solitons in chains of pre-deformed beams. *New J. Phys.*, 21(7):073008, 2019.

[70] M. H. Holmes. Introduction to Perturbation Methods. In J. E. Marsden, L. Sirovich, M. Golubitsky, W. Jäger, and F. John, editors, *Introduction to Perturbation Methods*, volume 20 of *Texts in Applied Mathematics*, pages 105–159. Springer New York, New York, NY, 1995.

[71] M. Peyrard and T. Dauxois. Physics of solitons. In *Physics of solitons*, pages 71–109. Cambridge university press edition, 2010.

[72] M. Brandenbourger, O. Gamayun, J. Veenstra, F. van Gorp, H. Terwisscha-Dekker, J.-S. Caux, and C. Coulais. Non-reciprocal breathing solitons, 2024. arXiv:2405.10562 [cond-mat, physics:nlin].

[73] M. J. Ablowitz, B. Prinari, and A. D. Trubatch. *Discrete and Continuous Nonlinear Schrodinger Systems*. Cambridge university press edition, 2004.

[74] J. Cuevas-Maraver, P. G. Kevrekidis, and F. Williams, editors. *The sine-Gordon Model and its Applications: From Pendula and Josephson Junctions to Gravity and*

High-Energy Physics, volume 10 of *Nonlinear Systems and Complexity*. Springer International Publishing, Cham, 2014.

[75] B. Haghpanah, L. Salari-Sharif, P. Pourrajab, J. Hopkins, and L. Valdevit. Multistable Shape-Reconfigurable Architected Materials. *Adv. Mater.*, 28(36):7915–7920, 2016.

[76] Y. Jiang, L. M. Korpas, and J. R. Raney. Bifurcation-based embodied logic and autonomous actuation. *Nat. Commun.*, 10(1):128, 2019.

[77] N. Y. Yao, C. Nayak, L. Balents, and M. P. Zaletel. Classical Discrete Time Crystals. *Nat. Phys.*, 16(4):438–447, 2020. arXiv:1801.02628 [cond-mat, physics:quant-ph].

[78] Z. G. Nicolaou and A. E. Motter. Anharmonic classical time crystals: A coresonance pattern formation mechanism. *Phys. Rev. Research*, 3(2):023106, 2021.

[79] Y. Chen, X. Li, C. Scheibner, V. Vitelli, and G. Huang. Realization of active metamaterials with odd micropolar elasticity. *Nat. Commun.*, 12(1):5935, 2021.

[80] C. Scheibner, W. T. M. Irvine, and V. Vitelli. Non-Hermitian Band Topology and Skin Modes in Active Elastic Media. *Phys. Rev. Lett.*, 125(11):118001, 2020.

[81] Y. Chen, T. Frenzel, S. Guenneau, M. Kadic, and M. Wegener. Mapping acoustical activity in 3D chiral mechanical metamaterials onto micropolar continuum elasticity. *Journal of the Mechanics and Physics of Solids*, 137:103877, 2020.

[82] V. E. Zakharov and L. A. Ostrovsky. Modulation instability: The beginning. *Physica D: Nonlinear Phenomena*, 238(5):540–548, 2009.

[83] J. M. Dudley, G. Genty, A. Mussot, A. Chabchoub, and F. Dias. Rogue waves and analogies in optics and oceanography. *Nat. Rev. Phys.*, 1(11):675–689, 2019.

[84] F. Copie, S. Randoux, and P. Suret. The Physics of the one-dimensional nonlinear Schrödinger equation in fiber optics: Rogue waves, modulation instability and self-focusing phenomena. *Reviews in Physics*, 5:100037, 2020.

[85] K. Tai, A. Hasegawa, and A. Tomita. Observation of modulational instability in optical fibers. *Phys. Rev. Lett.*, 56(2):135–138, 1986.

[86] P. K. Shukla and J. J. Rasmussen. Modulational instability of short pulses in long optical fibers. *Opt. Lett.*, 11(3):171, 1986.

[87] K. E. Strecker, G. B. Partridge, A. G. Truscott, and R. G. Hulet. Formation and propagation of matter-wave soliton trains. *Nature*, 417(6885):150–153, 2002.

[88] L. Liu, G. James, P. Kevrekidis, and A. Vainchtein. Breathers in a locally resonant granular chain with precompression. *Physica D: Nonlinear Phenomena*, 331:27–47, 2016.

[89] D. R. Solli, C. Ropers, P. Koonath, and B. Jalali. Optical rogue waves. *Nature*, 450(7172):1054–1057, 2007.

[90] M. J. Potasek. Modulation instability in an extended nonlinear Schrödinger equation. *Opt. Lett.*, 12(11):921, 1987.

[91] X. Cheng, J. Wang, and J. Li. Controllable rogue waves in coupled nonlinear Schrödinger equations with varying potentials and nonlinearities. *Nonlinear Dyn.*, 77(3):545–552, 2014.

[92] F. K. Diakonos, G. C. Katsimiga, X. N. Maintas, and C. E. Tsagkarakis. Symmetric solitonic excitations of the Abelian-Higgs "classical vacuum". *Phys. Rev. E*, 91(2):023202, 2014.

[93] A. E. Kraych, D. Agafontsev, S. Randoux, and P. Suret. Statistical Properties of the Nonlinear Stage of Modulation Instability in Fiber Optics. *Phys. Rev. Lett.*, 123(9):093902, 2019.

[94] A. K. Sarma. Modulational instability of few-cycle pulses in optical fibers. *EPL*, 92(2):24004, 2010.

[95] A. K. Sarma and M. Saha. Modulational instability of coupled nonlinear field equations for pulse propagation in a negative index material embedded into a Kerr medium. *J. Opt. Soc. Am. B*, 28(4):944, 2011.

[96] Y. Xiang, X. Dai, S. Wen, and D. Fan. Modulation instability in metamaterials with saturable nonlinearity. *J. Opt. Soc. Am. B*, 28(4):908, 2011.

[97] F. Bonnefoy, A. Tikan, F. Copie, P. Suret, G. Ducrozet, G. Prabhudesai, G. Michel, A. Cazaubiel, E. Falcon, G. El, and S. Randoux. From modulational instability to focusing dam breaks in water waves. *Phys. Rev. Fluids*, 5(3):034802, 2020.

[98] G. Xu, A. Chabchoub, D. E. Pelinovsky, and B. Kibler. Observation of modulation instability and rogue breathers on stationary periodic waves. *Phys. Rev. Research*, 2(3):033528, 2020.

[99] B. Kibler, J. Fatome, C. Finot, G. Millot, F. Dias, G. Genty, N. Akhmediev, and J. M. Dudley. The Peregrine soliton in nonlinear fibre optics. *Nature Phys*, 6(10):790–795, 2010.

[100] A. Tikan, C. Billet, G. El, A. Tovbis, M. Bertola, T. Sylvestre, F. Gustave, S. Randoux, G. Genty, P. Suret, and J. M. Dudley. Universality of the Peregrine Soliton in the Focusing Dynamics of the Cubic Nonlinear Schrödinger Equation. *Phys. Rev. Lett.*, 119(3):033901, 2017.

[101] A. Tikan, S. Randoux, G. El, A. Tovbis, F. Copie, and P. Suret. Local Emergence of Peregrine Solitons: Experiments and Theory. *Front. Phys.*, 8:599435, 2021.

[102] D. Pierangeli, M. Flammini, L. Zhang, G. Marcucci, A. J. Agranat, P. G. Grinevich, P. M. Santini, C. Conti, and E. DelRe. Observation of Fermi-Pasta-Ulam-Tsingou Recurrence and Its Exact Dynamics. *Phys. Rev. X*, 8(4):041017, 2018.

[103] S. Zhao, H. Yang, N. Chen, and C. Zhao. Controlled generation of high-intensity optical rogue waves by induced modulation instability. *Sci. Rep.*, 7(1):39926, 2017.

[104] H. Pichard, A. Duclos, J.-P. Groby, V. Tournat, and V. E. Gusev. Localized transversal-rotational modes in linear chains of equal masses. *Phys. Rev. E*, 89(1):013201, 2014.

[105] E. Prodan, K. Dobiszewski, A. Kanwal, J. Palmieri, and C. Prodan. Dynamical Majorana edge modes in a broad class of topological mechanical systems. *Nat. Commun.*, 8(1):14587, 2017.

[106] H. Duran, J. Cuevas-Maraver, P. G. Kevrekidis, and A. Vainchtein. Discrete breathers in a mechanical metamaterial. *Phys. Rev. E*, 107(1), 2023.

[107] N. Akhmediev, A. Ankiewicz, and J. M. Soto-Crespo. Rogue waves and rational solutions of the nonlinear Schrödinger equation. *Phys. Rev. E*, 80(2):026601, 2009.

[108] N. N. Akhmediev and V. I. Korneev. Modulation instability and periodic solutions of the nonlinear Schrödinger equation. *Theoretical and Mathematical Physics*, 69(2):1089–1093, 1986.

[109] N. N. Akhmediev, V. M. Eleonskii, and N. E. Kulagin. Exact first-order solutions of the nonlinear Schödinger equation. *Theoretical and Mathematical Physics*, 72(2):809–818, 1987.

[110] M. Joseph, M. Justin, V. David, S. Azakine Sindanne, and G. Betchewe. Modulational instability and rogue waves in one-dimensional nonlinear acoustic metamaterials: case of diatomic model. *Phys. Scr.*, 96(12):125274, 2021.

[111] E. T. Filipov, T. Tachi, and G. H. Paulino. Origami tubes assembled into stiff, yet reconfigurable structures and metamaterials. *Proc. Natl. Acad. Sci. U.S.A.*, 112(40):12321–12326, 2015.

[112] M. Isobe and K. Okumura. Initial rigid response and softening transition of highly stretchable kirigami sheet materials. *Sci. Rep.*, 6(1):24758, 2016.

[113] J. R. Raney and J. A. Lewis. Printing mesoscale architectures. *MRS Bull.*, 40(11):943–950, 2015.

[114] S. Sundaram, M. Skouras, D. S. Kim, L. Van Den Heuvel, and W. Matusik. Topology optimization and 3D printing of multimaterial magnetic actuators and displays. *Sci. Adv.*, 5(7):eaaw1160, 2019.

[115] B. Deng, V. Tournat, P. Wang, and K. Bertoldi. Anomalous Collisions of Elastic Vector Solitons in Mechanical Metamaterials. *Phys. Rev. Lett.*, 122(4):044101, 2019.

[116] E. B. Herbold and V. F. Nesterenko. Propagation of Rarefaction Pulses in Discrete Materials with Strain-Softening Behavior. *Phys. Rev. Lett.*, 110(14):144101, 2013.

[117] A. Demiquel, V. Achilleos, G. Theocharis, and V. Tournat. Modulation instability in nonlinear flexible mechanical metamaterials. *Phys. Rev. E*, 107(5):054212, 2023.

[118] Y. Silberberg. Collapse of otical pulses. *Opt. Lett.*, 15(22):1282–1284, 1990.

[119] A. Hasegawa and F. Tappert. Transmission of stationary nonlinear optical pulses in dispersive dielectric fibers. I. Anomalous dispersion. *Appl. Phys. Lett.*, 23(3):142–144, 1973.

[120] L. F. Mollenauer, R. H. Stolen, and J. P. Gordon. Experimental Observation of Picosecond Pulse Narrowing and Solitons in Optical Fibers. *Phys. Rev. Lett.*, 45(13):1095–1098, 1980.

[121] L. Pitaevskii and S. Stringari. *Bose-Einstein condensation and superfluidity*, volume 164. Oxford University Press., 2016.

[122] P. Emplit, J.P. Hamaide, F. Reynaud, C. Froehly, and A. Barthelemy. Picosecond steps and dark pulses through nonlinear single mode fibers. *Optics Communications*, 62(6):374–379, 1987.

[123] D. Krökel, N. J. Halas, G. Giuliani, and D. Grischkowsky. Dark-Pulse Propagation in Optical Fibers. *Phys. Rev. Lett.*, 60(1):29–32, 1988.

[124] A. M. Weiner, J. P. Heritage, R. J. Hawkins, R. N. Thurston, E. M. Kirschner, D. E. Leaird, and W. J. Tomlinson. Experimental Observation of the Fundamental Dark Soliton in Optical Fibers. *Phys. Rev. Lett.*, 61(21):2445–2448, 1988.

[125] C. Chong, P. G. Kevrekidis, G. Theocharis, and C. Daraio. Dark breathers in granular crystals. *Phys. Rev. E*, 87(4):042202, 2013.

[126] C. Chong, F. Li, J. Yang, M. O. Williams, I. G. Kevrekidis, P. G. Kevrekidis, and C. Daraio. Damped-driven granular chains: An ideal playground for dark breathers and multibreathers. *Phys. Rev. E*, 89(3):032924, 2014.

[127] V. F. Nesterenko. Waves in strongly nonlinear discrete systems. *Phil. Trans. R. Soc. A.*, 376(2127):20170130, 2018.

[128] G. Theocharis, N. Boechler, and C. Daraio. Nonlinear Periodic Phononic Structures and Granular Crystals. In P. A. Deymier, editor, *Acoustic Metamaterials and Phononic Crystals*, volume 173, pages 217–251. Springer Berlin Heidelberg, Berlin, Heidelberg, 2013. Series Title: Springer Series in Solid-State Sciences.

[129] Y. S. Kivshar and M. Peyrard. Modulational instabilities in discrete lattices. *Phys. Rev. A*, 46(6):3198–3205, 1992.

[130] I. Daumont, T. Dauxois, and M. Peyrard. Modulational instability: first step towards energy localization in nonlinear lattices. *Nonlinearity*, 10(3):617–630, 1997.

[131] M. Remoissenet. Low-amplitude breather and envelope solitons in quasi-one-dimensional physical models. *Phys. Rev. B*, 33(4):2386–2392, 1986.

[132] A. Tikan, F. Bonnefoy, G. Ducrozet, G. Prabhudesai, G. Michel, A. Cazaubiel, E. Falcon, F. Copie, S. Randoux, and P. Suret. Nonlinear dispersion relation in integrable turbulence. *Sci. Rep.*, 12(1):10386, 2022.

[133] K. P. Leisman, D. Zhou, J. W. Banks, G. Kovačič, and D. Cai. Effective dispersion in the focusing nonlinear Schrödinger equation. *Phys. Rev. E*, 100(2):022215, 2019.

[134] D. J. Frantzeskakis. Dark solitons in atomic Bose–Einstein condensates: from theory to experiments. *J. Phys. A: Math. Theor.*, 43(21):213001, 2010.

[135] R. Zaera, J. Vila, J. Fernandez-Saez, and M. Ruzzene. Propagation of solitons in a two-dimensional nonlinear square lattice. *International Journal of Non-Linear Mechanics*, 106:188–204, 2018.

[136] N. Akhmediev, A. Ankiewicz, and M. Taki. Waves that appear from nowhere and disappear without a trace. *Phys. Lett. A*, 373(6):675–678, 2009.

[137] P. Müller, C. Garrett, and A. Osborne. Meeting report: Rogue waves—The Fourteenth 'Aha Huliko'a Hawaiian Winter Workshop. *Oceanography*, 18(3):66–75, 2015.

[138] E. M. Bitner-Gregersen and O. Gramstad. Rogue Waves: Impact on Ships and Offshore Structures. *DNV GL*, 2015.

[139] K. Dysthe, H. E. Krogstad, and P. Müller. Oceanic Rogue Waves. *Annu. Rev. Fluid Mech.*, 40(1):287–310, 2008.

[140] E. Didenkulova. Catalogue of rogue waves occurred in the World Ocean from 2011 to 2018 reported by mass media sources. *Ocean & Coastal Management*, 188:105076, 2020.

[141] C. Kharif and E. Pelinovsky. Physical mechanisms of the rogue wave phenomenon. *European Journal of Mechanics - B/Fluids*, 22(6):603–634, 2003.

[142] M. Onorato, S. Residori, U. Bortolozzo, A. Montina, and F.T. Arecchi. Rogue waves and their generating mechanisms in different physical contexts. *Physics Reports*, 528(2):47–89, 2013.

[143] N. Akhmediev and E. Pelinovsky. Editorial – Introductory remarks on "Discussion & Debate: Rogue Waves – Towards a Unifying Concept?". *Eur. Phys. J. Spec. Top.*, 185(1):1–4, 2010.

[144] J. Gemmrich and L. Cicon. Generation mechanism and prediction of an observed extreme rogue wave. *Sci. Rep.*, 12(1):1718, 2022.

[145] J. K. Mallory. Abnormal waves on the south east coast of South Africa. *The International hydrographic review*, 1974.

[146] K. B. Dysthe. Refraction of gravity waves by weak current gradients. *J. Fluid Mech.*, 442:157–159, 2001.

[147] P. Janssen. *The Interaction of Ocean Waves and Wind*. Cambridge University Press, 1 edition, 2004.

[148] A. Toffoli, A. Alberello, H. Clarke, F. Nelli, A. Benetazzo, F. Bergamasco, B. N. Ntamba, M. Vichi, and M. Onorato. Observations of rogue seas in the Southern Ocean. *Phys. Rev. Lett.*, 132(15), 2024.

[149] M. Longuet-Higgins. On the distribution of the heights of sea waves: Some effects of nonlinearity and finite band width. *J. Geophys. Res.*, 85(C3):1519–1523, 1980.

[150] L. Wen, L. Li, Z. D. Li, S. W. Song, X. F. Zhang, and W. M. Liu. Matter rogue wave in Bose-Einstein condensates with attractive atomic interaction. *Eur. Phys. J. D*, 64(2-3):473–478, 2011.

[151] H. Bailung, S. K. Sharma, and Y. Nakamura. Observation of Peregrine Solitons in a Multicomponent Plasma with Negative Ions. *Phys. Rev. Lett.*, 107(25):255005, 2011.

[152] D. Ahmadou, H. Alphonse, M. Justin, D. Philippe, S. Alioum, G. Betchewe, D. Y. Serge, and K. T. Crepin. Dynamics of rogue waves and modulational instability with the Manakov system in a nonlinear electric transmission line with second couplings. *Eur. Phys. J. Plus*, 138(12):1113, 2023.

[153] E. G. Charalampidis, J. Lee, P. G. Kevrekidis, and C. Chong. Phononic rogue waves. *Phys. Rev. E*, 98(3):032903, 2018.

[154] R. El Koussaifi, A. Tikan, A. Toffoli, S. Randoux, P. Suret, and M. Onorato. Spontaneous emergence of rogue waves in partially coherent waves: A quantitative experimental comparison between hydrodynamics and optics. *Phys. Rev. E*, 97(1):012208, 2018.

[155] D. H. Peregrine. Water waves, nonlinear Schrödinger equations and their solutions. *J. Aust. Math. Soc. Series B, Appl. Math*, 25(1):16–43, 1983.

[156] M. Bertola and A. Tovbis. Universality for the Focusing Nonlinear Schrödinger Equation at the Gradient Catastrophe Point: Rational Breathers and Poles of the Tritronquée Solution to Painlevé I. *Comm. Pure Appl. Math.*, 66(5):678–752, 2013.

[157] A. Tikan, F. Bonnefoy, G. Roberti, G. El, A. Tovbis, G. Ducrozet, A. Cazaubiel, G. Prabhudesai, G. Michel, F. Copie, E. Falcon, S. Randoux, and P. Suret. Prediction and manipulation of hydrodynamic rogue waves via nonlinear spectral engineering. *Phys. Rev. Fluids*, 7(5):054401, 2022.

[158] J. Yang. *Nonlinear waves in integrable and nonintegrable systems*, volume 16. 2010.

[159] V. I. Shrira and V. V. Geogjaev. What makes the Peregrine soliton so special as a prototype of freak waves? *J. Eng. Math.*, 67(1-2):11–22, 2010.

[160] S. M. Cox and P. C. Matthews. Exponential Time Differencing for Stiff Systems. *Journal of Computational Physics*, 176(2):430–455, 2002.

[161] A.-K. Kassam and L. N. Trefethen. Fourth-Order Time-Stepping for Stiff PDEs. *SIAM J. Sci. Comput.*, 26(4):1214–1233, 2005.

[162] A. Paliovaios, G. Theocharis, V. Achilleos, and V. Tournat. Transition waves in bistable systems generated by collision of moving breathers. *Extreme Mechanics Letters*, 71:102199, 2024.

[163] M. Krusemeyer. *Differential Equations*. Macmillan College Pub. Co., 1994.

COLLEGE SCIENCES
DOCTORAL DE L'INGENIERIE
PAYS DE LA LOIRE ET DES SYSTEMES

Le Mans Université

Titre : Contrôle d'ondes modulées non linéaires dans des métamateriaux mécaniques flexibles

Mots clés : Systèmes périodiques non linéaire, Métamatériaux mécaniques flexibles, Equation de Schrödinger non linéaire, Instabilité modulationnelle, Soliton-enveloppe vectoriel, Catastrophe de Gradient.

Résumé : Ce travail est consacré à l'étude des ondes modulées se propageant le long de métamatériaux mécaniques flexibles nonlinéaires (FlexMM). Ces structures sont des matériaux architecturés constitués d'éléments souples très déformables connectés à des éléments plus rigides. Leur capacité à subir de grandes déformations locales favorise l'apparition de phénomènes d'ondes non linéaires. En utilisant une approche par éléments discrets, nous formulons des équations discrètes non linéaires qui décrivent les déplacements longitudinaux et rotationnels de chaque cellule unitaire et leur couplage mutuel. Une analyse multi-échelles est employée afin d'obtenir une équation de Schrödinger non linéaire (NLS) effective décrivant les ondes modulées pour le degré de liberté rotationnel du FlexMM. En nous appuyant sur l'équation NLS, nous identifions divers types de phénomènes d'ondes non linéaires dans le FlexMM. En particulier, nous avons observé que des ondes planes faiblement non linéaires peuvent être modulationellement stables ou instables en fonction des paramètres du système et de l'excitation utilisée. De plus, nous avons trouvé que les FlexMMs supportent des solitons-enveloppe vectoriels où le degré de liberté rotationnel des unités peut prendre la forme de solitons dits "bright" ou "dark" et, en raison du couplage, le degré de liberté de déplacement longitudinal présente un comportement de type "kink". Enfin, nous abordons le phénomène de "catastrophe de gradient", qui prédit l'émergence de structures similaires aux solitons de Peregrine dans la limite semi-classique de l'équation NLS, dans la structure FlexMM. Grâce à nos prédictions analytiques et à l'utilisation de simulations numériques, nous pouvons déterminer les conditions requises et les valeurs des paramètres physiques pour observer ces phénomènes dans les FlexMMs.

Title : Control of nonlinear modulated waves in flexible mechanical metamaterials

Keywords : Nonlinear periodic systems, Flexible mechanical metamaterials, Nonlinear Schrödinger equation, Modulation instability, Envelope vector soliton, Gradient catastrophe.

Abstract: This work is dedicated to the investigation of modulated waves propagating along nonlinear flexible mechanical metamaterials (FlexMM). These structures are architected materials consisting of highly deformable soft elements connected to stiffer ones. Their capacity to undergo large local deformations promotes the occurrence of nonlinear wave phenomena. Using a lump element approach, we formulate nonlinear discrete equations that describe the longitudinal land rotational displacements of each unit cell and their mutual coupling. A multiple scales analysis is employed in order to derive an effective nonlinear Schrödinger (NLS) equation describing envelope waves for the rotational degree of freedom of FlexMM. Leveraging on the NLS equation we identify various type of nonlinear waves phenomena in FlexMM. In particular we observed that weakly nonlinear plane waves can be modulationally stable or unstable depending of the system and excitation parameters. Moreover we have found that the FlexMMs support envelope vector solitons where the units rotational degree of freedom might take the form of bright or dark soliton and due to coupling, the longitudinal displacement degree of freedom has a kink-like behavior. Finally, we address the phenomenon of "gradient catastrophe", which predicts the emergence of Peregrine soliton-like structures in the semiclassical limit of the NLS equation, in FlexMM. Through our analytical predictions and by using numerical simulations, we can determine the required conditions and the values of the physical parameters in order to observe these phenomena in FlexMMs.